A revised orbital forcing concept of West African climate and vegetation variability during the Pliocene and the Last Glacial cycle

- Molecular isotopic approach and proxy calibration -

Dissertation for the Doctoral Degree in Natural Sciences

Dr. rer. nat.

in the Faculty of Geosciences

at the University of Bremen

submitted by

Rony Rupert Küchler

March, 2015

marum Universität Bremen GLOMAR

Erklärung / Declaration

Name: Rony Rupert Küchler
Adresse: Osterfeuerbergstr. 121, 28217 Bremen

Hiermit versichere ich, dass
(1) die Arbeit ohne unerlaubte Hilfe angefertigt,
(2) keine anderen als die von mir angegebenen Quellen und Hilfsmittel verwendet und
(3) die den benutzten Werken wörtlich oder inhaltlich entnommenen Stellen als solche kenntlich gemacht wurden.

Bremen, den 31.03.2015

_____

(Unterschrift)

Tag des Promotionskolloquiums:
19. Mai 2015

Mitglieder des Prüfungsausschusses:

Gutachter der Dissertation
Prof. Dr. Gerold Wefer
Prof. Dr. Gesine Mollenhauer

Weitere Mitglieder
Prof. Dr. Heiko Pälike
Dr. Enno Schefuß
Dr. Lydie Dupont
Meral Yavuz

The world is not willing to stand still long enough to see it clear as a whole.
after Hunter S. Thompson (*18.7.1937 - †20.2.2005)

Table of Contents

Acknowledgements

During the last years, many people have contributed to the successful finish of my PhD project and mentioning all of them for everything they did would add another main chapter to this thesis.

First of all I want to thank Gerold Wefer for his confidence in my work and for providing the chance to gain experiences in an excellent institution with a diverse scientific network. His willingness to support my academic career is highly appreciated.

The project itself would not have been tackled by anyone without the efforts of Enno Schefuß, who deserves the biggest thanks for his faith in me, his patient support at any time throughout my work and for imparting his knowledge and experience in an amicable way. His “group within the working group“ offered a great place to extend my knowledge on biomarkers by providing the right atmosphere and lab facilities to get a multitude of insights into molecular environmental proxies and their applications. Small but nice social events in a comfortable ambience completed these experiences.

Special thanks go to Lydie Dupont for her patience during many discussions, giving sincere advices and having ideas, which significantly promoted the evolution of the “hybrid drive“, but also the thesis as a whole.

The ordinary work load was facilitated by the help of many people, of which I want to thank first of all Britta Beckmann for her endless care during my lab work by guiding me through waves of solvents and being available for every question. Furthermore, I want to thank Thomas (the grinder) and “Metal“ Meral (thanks also for the birthday cleaning) for doing some dirty jobs in the lab, Wolfgang, Birgit, Ralph, Ulla, Vera, Thomas and Walter for technical support, and Ralf Tiedemann for his competent efforts in my thesis committee.

I am also grateful to Gerd Fischer for the opportunity to join a research cruise with RV Poseidon, which brought me close to my study area and coincidentially, right into a dust storm (jackpot!). The time on board was very impressive and revealed, at least in part, what it takes to get some samples. Thanks to Gerd, Götz, Isabell, Kalle, Marco and Nico, who made (working) life easier and enjoyable during this time.

Thank you very much to all who have contributed to a great time for me in Bremen. This includes (in alphabetical order): Andreas, Anna, Christoph, Francesca, Ines, Jan, Jana, Katja, Maria, Nando (my fellow sufferer), Moritz (for the music, concerts and constant visits), Nicole (for the chili experience), Sebastian (the fifth office mate), Stefan “Zwiebel“ and Sven (for the music sessions and concerts), Thorsten (for the special events), Tim (for entertaining and educational discussions), Tolga (the special agent), Yansheng (no more print jobs!),....

Finally, I want to thank my parents for their sincere support, tireless patience and constant motivation. Without their absolute believe in me, I wouldn‘t be who I am.

Abbreviations

AABW	Antarctic Bottom Water
ACL	Average chain-length
AEJ	African Easterly Jet
AHP	African Humid Period
AMOC	Atlantic Meridional Overturning Circulation
BP	Before Present
C_3 plants	Plants, using C_3-type photosynthesis
C_4 plants	Plants, using C_4-type photosynthesis
CAM	Plants, capable to use both C_3- and C_4-type photosynthesis
CAS	Central American Seaway
CPI	Carbon peference index
D	Deuterium
IHIG	Interhemispheric insolation gradient
ITCZ	Intertropical Convergence Zone
ka	Thousand years (before present)
LGC	Last Glacial cycle
LGM	Last Glacial Maximum
LIG	Latitudinal insolation gradient
Ma	Million years (before present)
MAT	Mean air temperature
MIS	Marine isotope stage
NADW	North Atlantic Deep Water
NETW	Northeast trade winds
NHG	Northern Hemisphere Glaciations
ODP	Ocean Drilling Program
SST	Sea-surface temperatures (given in degree centigrade, °C)
$U^{k'}_{37}$	Alkenone unsaturation index
VP	Water vapor pressure
VPDB	Vienna Pee Dee Belemnite
VSMOW	Vienna Standard Mean Ocean Water
XRF	X-ray fluorescence
$\delta^{13}C$	Stable carbon isotopic composition (given in per mil, ‰ vs. VPDB)
$\delta^{13}C_{wax}$	$\delta^{13}C$ of plant waxes
δD	Stable hydrogen isotopic composition (given in per mil, ‰ vs. VSMOW)
δD_p	δD of precipitation
δD_{wax}	δD of plant waxes
$\delta^{18}O$	Stable oxygen isotopic composition (given in per mil, ‰ vs. VPDB)
ε	Apparent fractionation between δD_{wax} and δD_p

Abstract

The tropical monsoon system is a pivotal feature of the atmospheric circulation and is tightly linked to global climate dynamics. Understanding the future development of the current climate change towards warmer conditions relies heavily on our knowledge of analogous situations in the past. One of the most promising time intervals to study a warmer-than-today climate is the Pliocene about 3-5 Ma ago, since it constitutes the most recent period of the geological record with many boundary conditions similar to today. This PhD thesis combines two main topics, comprising paleoclimate variability and proxy calibration, and focuses on the application of stable carbon and hydrogen isotopes of plant-wax-derived long-chain *n*-alkanes ($\delta^{13}C_{wax}$, δD_{wax}), as well as other (in)organic geochemical proxies. All studies presented herein were carried out on marine sediments from the Northeast (NE) Atlantic Ocean close to West Africa, in order to characterize past environmental conditions on the adjacent continent (down-core analyses), as well as to strengthen the significance of the applied methods (surface mapping).

The hydrologic reconstruction of the Sahara-Sahel transition during the Last Glacial cycle is based on a deep-sea sediment core and reveals a consistent anti-correlation of the δD_{wax} and $\delta^{13}C_{wax}$ records throughout the last 130 ka. In line with published pollen data, this plant-wax signal is attributed to the combined effects of a high susceptibility of the Sahelian vegetation to precipitation changes and the activity of the NE trade winds (NETW). Dry (humid) conditions are indicated by enriched (depleted) δD_{wax} values, and promote a retreat (extension) of the C_4-plant-dominated vegetation in the Sahel, which reduces (increases) the amount of C_4 plant waxes exported from this region, while simultaneously, enhanced (weakened) NETW supply more (less) C_3 plant waxes from areas to the north of the Sahara, resulting in more depleted (enriched) $\delta^{13}C_{wax}$ values. δD_{wax}-inferred humidity changes are supported by concomitant shifts in weathering intensity, based on varying major element ratios. Orbital-scale climate changes in West Africa are generally caused by high-amplitude fluctuations in Northern Hemisphere summer insolation intensity. However, during Marine Isotope Stages 2 and 3, when insolation variability was minor, the hydrologic regime was more prone to variations in NE Atlantic sea-surface temperatures (SST), based on alkenones.

Extending the molecular isotopic approach from the Last Glacial cycle to the Pliocene provides further indications that a solely precession-dominated insolation forcing is insufficient to explain West African monsoon variability as a whole. Two fundamental modes of orbital forcing were identified: During eccentricity maxima, i.e., when precession was strong, the West African monsoon was indeed controlled by summer insolation intensity, but during eccentricity minima, when changes in precession and thus insolation were minimal, the obliquity-dominated latitudinal insolation gradient during summer became the primary influence on the distribution of monsoonal rainfall. This hybrid insolation forcing concept accounts for the atmospheric/oceanic linkages between low and high latitudes, which increase significantly in importance during subsequent Northern Hemisphere Glaciations.

The application of δD_{wax} as humidity proxy is still subject to ongoing research, since many factors may contribute to the final isotopic signal captured in plant waxes. For this reason, the environmental significance of δD_{wax} changes detected in marine surface sediments was investigated along a N-S-transect from Morocco to Guinea. Additional $\delta^{13}C_{wax}$ analyses formed the basis for the attribution of the deposited plant waxes to continental vegetation

sources. In line with previous studies, a maximum in C_4 plant contributions is found at the latitudes of the Sahel, while C_3 plants dominate off Morocco and Guinea corresponding to the vegetation cover. These findings thus support further implications based on δD_{wax}. Interestingly, despite of the large climate and vegetation gradient, the apparent fractionation (ε) of the *n*-C_{31} alkane, relative to precipitation δD (δD_p), is almost invariable along the transect. This is also expressed in a significant correlation between its δD and annual δD_p, in contrast to that of the *n*-C_{29} and *n*-C_{33} alkanes. Instead, these latter two compounds correlate significantly with $\delta^{13}C_{wax}$ and mean air temperatures, which indicates the influence of vegetation changes and related differences in water use efficiency on the corresponding δD_{wax} signatures. This pattern is mostly restricted to the northern part, between Morocco and the Sahel, while in the southern part, δD_{wax} and ε values yield negligible deviations among homologs, independent of mixed C_3/C_4 contributions. For the West African setting, the *n*-C_{31} alkane is thus suggested as the most reliable (i.e., unbiased) indicator of the continental hydrologic conditions and thus, suitable for paleoclimate reconstructions. Finally, the distinct pattern of latitudinal changes in δD_{wax} and $\delta^{13}C_{wax}$ may provide further evidence for latitudinal shifts in climate and vegetation, based on the isotopic offsets between homologs.

Zusammenfassung

Der tropische Monsoon ist ein entscheidendes Element der atmosphärischen Zirkulation und ist somit eng verbunden mit der globalen Klimadynamik. Ein Verständnis der zukünftigen Entwicklung des gegenwärtigen Klimawandels zu wärmeren Bedingungen beruht erheblich auf unser Wissen über entsprechende Gegebenheiten in der Vergangenheit. Eine der erfolgversprechendsten Zeitintervalle für die Untersuchung eines, relativ zur heutigen Zeit, wärmeren Klimas ist das Pliozän (vor etwa 3-5 Ma), da es die jüngste Phase in der Erdgeschichte darstellt, in der viele Rahmenbedingungen vergleichbar zu heute waren. Diese Dissertation kombiniert zwei Hauptthemen, Paläoklima-Variabilität und Proxy-Kalibrierung, und konzentriert sich auf die Anwendung von stabilen Kohlenstoff- und Wasserstoff-Isotopen von Pflanzenwachs-stammenden langkettigen *n*-Alkanen ($\delta^{13}C_{wax}$, δD_{wax}), sowie anderer (in) organisch-geochemischer Proxies. Alle nachstehend präsentierten Studien wurden an marinen Sedimenten aus dem nordöstlichen (NE) Atlantischen Ozean nahe West Afrika durchgeführt, um die vergangenen Umweltbedingungen des angrenzenden Kontinents zu beschreiben (Bohrkern-Analyse), als auch die Bedeutung der angewendeten Methoden auszubauen (Oberflächen-Kartierung).

Die hydrologische Rekonstruktion des Sahara-Sahel-Grenzverlaufs während des Letzten Glazialen Zyklus basiert auf einen Tiefsee-Sedimentkern und zeigt eine beständige Antikorrelation zwischen δD_{wax} und $\delta^{13}C_{wax}$ Daten während der letzten 130 ka. Im Einklang mit publizierten Pollendaten, kann dieses Pflanzenwachs-Signal auf die sich aufsummierenden Effekte einer hohen Empfindlichkeit der Vegetation in der Sahel gegenüber Niederschlagsänderungen und der Aktivität der NE Passatwinde (NETW) zurückgeführt werden. Trockene (feuchte) Bedingungen werden angezeigt durch angereicherte (abgereicherte) δD_{wax} Werte, und begünstigen einen Rückzug (Ausbreitung) der C_4-dominierten Vegetation in der Sahel, wodurch der Export von C_4 Pflanzenmaterial aus dieser Region reduziert (erhöht) wird, während gleichzeitig stärkere (schwächere) NETW mehr (weniger) C_3 Pflanzenwachse aus Gebieten nördlich der Sahara liefern, resultierend in abgereicherte (angereicherte) $\delta^{13}C_{wax}$ Werte. Die aus den δD_{wax} Werten abgeleiteten Feuchtigkeitsänderungen werden untermauert durch begleitende Änderungen in der Verwitterungsintensität, basierend auf Änderungen der Hauptelement-Verhältnisse. Klimawandel in West Afrika auf orbitalen Zeitskalen wird generell durch starke Intensitätsschwankungen in der Sonneneinstrahlung während der Sommerjahreszeit in der Nordhemisphäre verursacht. Während den Marinen Isotopen Stadien 2 und 3 waren die Schwankungen in der Insolation jedoch gering und das hydrologische Regime wurde anfälliger für Schwankungen der NE atlantischen Meeresoberflächentemperaturen, basierend auf Alkenonen.

Die Erweiterung des molekular-isotopischen Ansatzes vom Letzten Glazialen Zyklus zum Pliozän liefert weitere Anzeichen, dass lediglich der Einfluss der präzessions-gesteuerten Insolation die Variabilität des West Afrikanischen Monsoon in der Gesamtheit ungenügend beschreibt. Grundsätzlich konnten zwei Arten von orbitalen Änderungen bestimmt werden: Während Exzentrizitätsmaxima, d.h. wenn Schwankungen in der Präzession am stärksten waren, wurde der West Afrikanische Monsoon in der Tat von der Sonneneintrahlung während des Sommers dominiert, aber während Exzentrizitätsminima, als Änderungen in der Präzession und somit in der Sonneneinstrahlung gering waren, wurde der latitudinale Insolationsgradient, der im Sommer durch die Obliquität gesteuert wird, zum primären

Einfluss auf die Regenverteilung. Dieses Konzept einer hybriden Insolationssteuerung berücksichtigt die atmosphärischen und ozeanographischen Koppelungen zwischen den niederen und hohen Breiten, welche während der folgenden Nordhemisphären-Vereisungen entscheidend an Bedeutung zunehmen.

Die Anwendung von δD_{wax} als Feuchtigkeitsindikator ist nach wie vor Bestandteil laufender Forschung, da zahlreiche Faktoren in das endgültige Isotopensignal von Pflanzenwachsen miteinfließen können. Aus diesem Grund wurde die ökologische Aussagekraft von δD_{wax} Änderungen in marinen Oberflächensedimenten entlang eines N-S-Transekts von Marokko bis Guinea untersucht. Zusätzliche $\delta^{13}C_{wax}$ Analysen bildeten die Grundlage für die Zuordnung der abgelagerten Plfanzenwachse zu kontinentalen Vegetationsquellen. Im Einklang mit früheren Studien, wurden die höchsten C_4 Pflanzeneinträge vor der Sahel und höchste C_3 Pflanzeneinträge vor Marokko und Guinea gefunden, entsprechend der Vegetation an Land. Diese Ergebnisse unterstützen daher weitere Schlussfolgerungen, basierend auf δD_{wax}. Interessanterweise bleibt trotz des großen Klima- und Vegetationsgradienten die scheinbare Fraktionierung (ε) der *n*-C_{31} Alkane, relativ zum δD im Niederschlag (δD_p), nahezu unverändert entlang des Transekts. Dies zeigt sich auch in einer signifikanten Korrelation zwischen dessen δD und jährlichen δD_p Werten, im Gegensatz zu denen der *n*-C_{29} und *n*-C_{33} Alkane. Stattdessen korrelieren letztere Komponenten mit $\delta^{13}C_{wax}$ und Lufttemperatur, was auf einen Einfluss von Vegetationsänderungen und damit einhergehende Unterschiede in der Wassernutzung auf das dazugehörige δD_{wax} Signal hinweist. Dieses Muster beschränkt sich auf den nördlichen Teil, zwischen Marokko und der Sahel, während im südlichen Teil die δD_{wax} und ε Werte vernachlässigbare Abweichungen zwischen den Homologen zeigen, unabhängig von einer gemischten C_3/C_4 Vegetation. Für Westafrika kann somit abgeleitet werden, dass die *n*-C_{31} Alkane am verlässlichsten (d.h. unverfälschtesten) die hydrologischen Bedingungen an Land reflektieren, und von daher geeignet sind für Paläoklima-Rekonstruktionen. Letztendlich zeigt sich auch, dass das deutliche Muster in den latitudinalen Änderungen von δD_{wax} und $\delta^{13}C_{wax}$ einen zusätzlichen Ansatz bietet, um Klima- und Vegetationsänderungen zu erfassen, basierend auf den isotopischen Unterschieden zwischen den einzelnen Homologen.

I

Introduction

The hydrologic cycle is of vital importance for the global climate system, owing to its function in regulating the heat and moisture balance. This is mainly achieved through the atmospheric and ocean circulation, which tend to equalize the differences in solar heating between low and high latitudes. Without these effects, the average annual equator-to-pole temperature gradient would amount to around 100 °C compared to the actual value of around 40 °C (Lindzen, 1990, 1994). The importance of this heat redistribution is further illustrated by the fact that around 50% of the annual energy budget of high latitudes originates from lower latitudes (Peixoto and Oort, 1992), peaking in winter, when polar night conditions prevail at high latitudes (Davis and Brewer, 2011). In this way, atmospheric water vapor acts as the dominant greenhouse gas, exerting an important feedback on global warming (e.g., Held and Soden, 2000). According to the Fifth Assessment Report of the Intergovernmental Panel on Climate Change (IPCC, 2014), climate models still perform less well for future changes in precipitation than, e.g., for surface temperature, and processes involving clouds and aerosols are also represented with low confidence. For instance, future climate models reach no consistent prediction of African rainfall, and such uncertainties emphasize the limitations of our current understanding of the global climate system (Giannini et al., 2008a). However, it seems possible that monsoon systems will expand in the future associated with more frequent and more intense precipitation events in the tropics, while subtropical areas, like the Sahara desert, will likely experience increased aridification (IPCC, 2014). Our current state of knowledge on climate dynamics thus remains limited, especially when focusing on the instrumental record since 1850 (e.g., Brohan et al., 2006).

Another possibility to assess the dynamics of a changing climate, including the diverse processes involved and its environmental impacts on the flora and fauna, is achieved by paleoclimate studies. These provide the unique advantage to investigate long-term developments of diverse aspects related to climate, such as temperature, ocean circulation, as well as floral and faunal assemblages adapted to different marine and terrestrial environments. Long, continuous archives are the basis of such studies, particularly found in marine sediments, which accumulated over geological timescales, spanning a range of up to several millions of years (Ma) with a temporal resolution of hundreds to thousands of years (ka). Considering the future climate warming, investigations of analogous conditions in the past are fundamental for our understanding of the underlying mechanisms. A suitable time interval to study a warmer-than-today climate is the Pliocene (~3-5 Ma), which is often referred to as future analog, since it constitutes the last warm period of the geological record, including many boundary conditions similar to today (Dowsett et al., 2013; Haywood et al., 2013b).

A prominent method in paleoclimate research is based on the stable oxygen isotopic composition ($\delta^{18}O$) of marine organisms (like planktonic and benthic foraminifera) preserved in marine sediments or from O_2 gas inclusions trapped in continental ice sheets, which can be either related to changes in temperature, salinity and/or ice volume (e.g., Petit et al., 1999; Shackleton, 2000; Haug et al., 2001). Equally, the stable carbon isotopic composition ($\delta^{13}C$) of benthic foraminifera can be used as indicator for past changes in deep-sea ventilation, which is mostly a function of the intensity of the Meridional Overturning Circulation (MOC), an integral part of the global climate system, also called thermohaline circulation (Raymo et al., 1990; Vidal et al., 1997). In this context, it becomes clear that the relevance of paleoclimate studies is also based on the fact that there is no observational evidence of a long-term trend in Atlantic MOC (AMOC) variations available (IPCC, 2014). In contrast to marine settings, continental paleo-archives are by far more fragmentary and less frequent. Therefore, our understanding of climate-driven shifts in the terrestrial biosphere also heavily relies on marine sediments (Larrasoaña et al., 2013), which are supplied with terrigenous material by aeolian and fluvial transport (e.g., Holz et al., 2004; Huang et al., 2000).

Typical (paleo)environmental proxies to assess variations in terrestrial climate and vegetation are dust (based on chemical, grain size, clay mineral and Sr/Nd isotopic compositions) and palynological records (pollen assemblages of different plant taxa), indicating changes in aridity (e.g., Tiedemann et al., 1994) and the composition and distribution of plants adapted to different environments (e.g., Dupont, 2011). The development of new analytical methods provides the basis for the application of more sophisticated proxies like compound-specific carbon (e.g., Freeman et al., 1989; Hayes et al., 1990; Collister et al., 1994; Simoneit, 1997) and hydrogen (e.g., Estep and Hoering, 1980; Sternberg, 1988; Sessions et al., 1999) isotopes, which are both influenced by environmental and biochemical effects.

This thesis investigates the long-term development of the West African monsoon and vegetation during the Pliocene and the Last Glacial cycle, in order to identify the links between low-latitude climate variability and orbital changes, as well as to the global climate reorganization related to, for instance, ocean gateway closure (Central American Seaway), Northern Hemisphere Glaciation and associated changes in AMOC and the atmospheric circulation. Another key aspect is to improve the application of plant-wax-specific stable hydrogen and carbon isotopes preserved in marine sediments as proxy for past changes in hydrology and vegetation within the West African setting.

The following chapters provide a brief overview of today‘s rainfall variability (section 1.1.1) and vegetation belts in Africa (section 1.1.2), dust sources and sinks (section 1.1.3) and the North Atlantic circulation (section 1.1.4). The second part of the Introduction has a focus on the role of extra-terrestrial forcing (section 1.2.1) and presents evidence for climate change during the past 5 Ma, covering the Pliocene (section 1.2.2), Northern Hemisphere Glaciations (section 1.2.3), Last Glacial cycle (section 1.2.4) and some background information on the

implications for hominin evolution and migration (section 1.2.5). Scientific objectives, approach and outline are given in Chapter II, including a summary of sample material (section 2.2.1), a short discussion on age models (section 2.2.2) and a brief description of the applied methods (sections 2.2.3-2.2.7). Details on the analytical procedures are provided in each Methods section of Chapters III, IV and V. These chapters form the main part of this thesis, comprising three manuscripts, that are either published in (Chapter III), submitted to (Chapter IV) or ready for submission (Chapter V) to international scientific journals. The final Chapter VI presents, in a nutshell, a synthesis of the main findings that have been generated during this PhD project and extends the discussion on these topics, including further implications and new approaches for the assessment of past environmental changes in the (sub-)tropics.

1.1 Environmental setting of West Africa

1.1.1 Rainfall variability

The amount and distribution of precipitation in West Africa is a function of latitude (Nicholson, 2009; **Fig. 1.1**). This is related to seasonal shifts of the pressure field over the Sahara and the position of the convergence zones, notably the Intertropical Convergence Zone (ITCZ; **Fig. 1.2**). During boreal summer (July/August), a low pressure system is formed over the Sahara due to stronger heating of the North African continent (sensible heating) relative to the adjacent ocean (latent heating), and is situated between the NE trade winds (NETW) and the moist "SW monsoon" (SE trade winds turning to SW after crossing the equator due to the

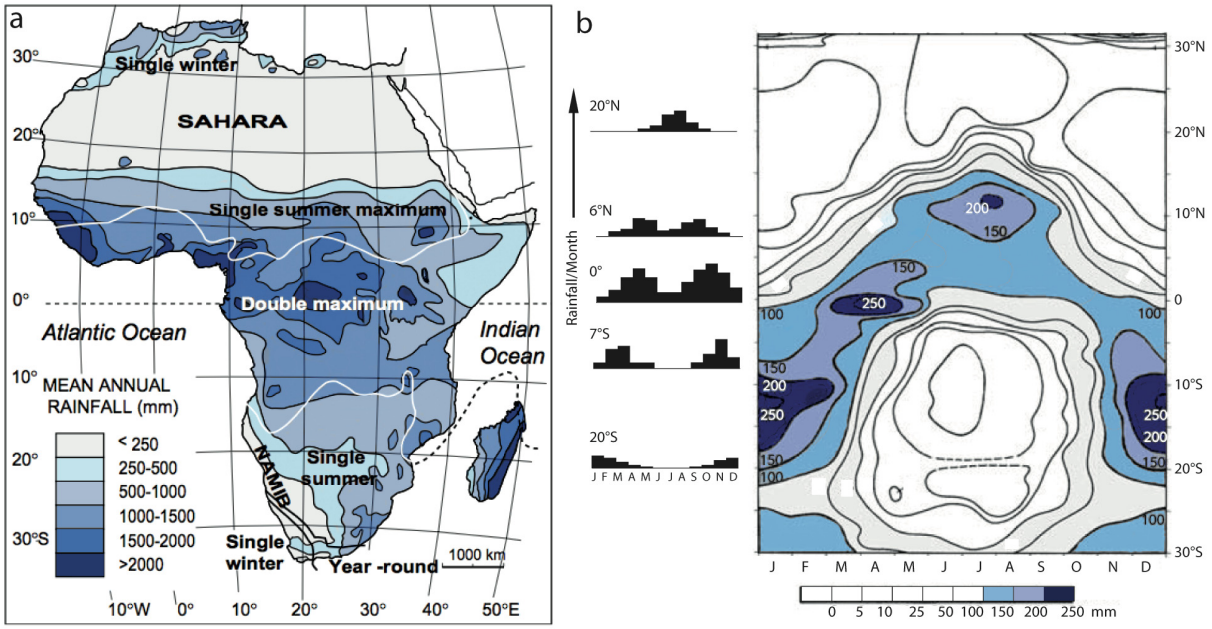

Fig. 1.1: Rainfall distribution in Africa with (a) the spatial pattern of mean annual rainfall (modified after Gasse et al., 2008) and (b) monthly rainfall amounts as a function of latitude, following the seasonal migration of the ITCZ (modified after Nicholson, 2009). The seasonal cycle at selected meteorological stations is displayed on the left in (b).

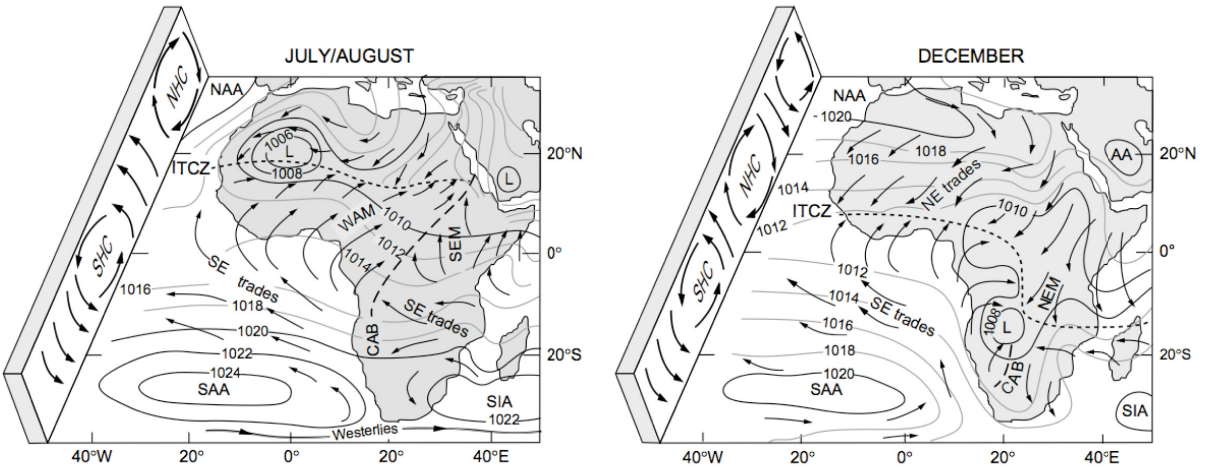

Fig. 1.2: Low-level atmospheric circulation over Africa during boreal summer (left) and winter (right) (adapted from Gasse et al., 2008; modified after Nicholson, 1996). NAA, North Atlantic Anticyclone; SAA, South Atlantic Anticyclone; AA, Arabian Anticyclone; SIA, South Indian Anticyclone; L, major low pressure cell; WAM, West African Monsoon; NEM, northerly East African monsoon; SEM, southerly East African monsoon; dotted line: Intertropical Convergence Zone (ITCZ); dashed line: Congo Air Boundary (CAB). Latitudinal cross section: SHC, southern Hadley Cell; NHC, northern Hadley Cell.

Coriolis effect). The ITCZ lies in-between at ~18°-20°N and results from the convergence of these two wind systems. Another convergence zone (Zaire/Congo Air Boundary) in the eastern part of Africa separates the inflows of the Atlantic and Indian Oceans. Over southern Africa, high pressure dominates during austral winter. Seasonal changes of these pressure systems and associated winds lead to a reversed pattern, with high pressure forming over the Sahara and low pressure over southern Africa. This forces the convergence zones to move southward, most obvious for the ITCZ, which reaches far into the Southern Hemisphere (**Fig. 1.2**). Tropical rainfall is tightly linked to atmospheric dynamics in higher altitudes, involving the African Easterly Jet (AEJ) and the Tropical Easterly Jet, rather than only to processes at the surface (Nicholson, 2009). Highest precipitation amounts are found in the equatorial region, where it easily exceeds 2000 mm in the course of a year. The equatorial regions are marked by a double rainfall maximum, occurring during the transition seasons, which is mostly attributed to the latitudinal migration of the ITCZ. In contrast, precipitation of the temperate regions in northern and southern Africa is influenced by the mid-latitude westerlies, with mean annual rainfall of ~800-1000 mm, maximizing during the winter season. Regionally, high-altitude areas, like those of eastern Africa and the coastal regions of Liberia, Sierra Leone and Guinea, also experience high precipitation amounts. The Sahara desert separates the summer and winter precipitation regimes in the Northern Hemisphere and thus, exhibits a more complex pattern. Most of the rainfall in the desert occurs during the transition seasons and has an extra-tropical origin related to the mid-latitude westerlies (Nicholson, 1981), interacting with the tropical easterlies (Nicholson, 2000). In exceptional cases, such as the intense rainfalls in Algeria and Tunisia in September of 1969, which led to catastrophic floods, winter rainfall is occasionally penetrating further south, being responsible for the

majority of rain events in the central parts of the desert. The rainfall regime in the Southern Hemisphere is similarly complex. A precipitation maximum is mostly reached during austral summer (January), while many regions like the western part are more influenced by the transition seasons and are often linked to SST changes of the adjacent South Atlantic (Nicholson, 2000). High sensitivity to tropical SST changes was also observed for rainfall variability in the Sahel on interannual and interdecadal timescales (Giannini et al., 2003, 2008a,b). This is also supported by Nicholson (2009), who attributed this relationship to the accompanying changes in the pressure gradient.

The seasonal migration of the tropical atmospheric circulation is asymmetric, as its southward shift occurs much faster than the northward, explaining the generally abrupt ending of the rainy season (Nicholson and Grist, 2003). In turn, precipitation during the wet season moderates the surface temperatures, thus enhancing the temperature contrast to the hyperarid Sahara in the north, which strengthens the AEJ during its northward displacement after rainfall (Nicholson and Grist, 2003). In addition, mesoscale (10-40 km) soil-moisture gradients appear to be important to promote storm initiation during the wet season in the Sahel, indicating the importance of land-atmosphere feedbacks on atmospheric convection (Taylor et al., 2011). This also includes changes in the vegetation cover, that are seen as amplifiers of the oceanic forcing through feedback mechanisms related to surface albedo and the moisture balance (Giannini et al., 2008a,b).

1.1.2 Vegetation distribution and composition

Rainfall variability is of primary importance for the distribution and composition of African biomes (White, 1983; Mayaux et al., 2004; **Fig. 1.3** and **1.4**): Focusing on West Africa, vegetation to the north of the Sahara generally comprises forests and steppes. The former consists of (among others) *Quercus* (oak tree), *Pinus* (pine tree) and *Cedrus* (Cedar), while the latter has grasses (e.g., *Stripa*) and shrubs (*Ephedra* and *Artemisia*). Some *Artemisia sp.* are also abundant in mountainous areas. The semi-desert grasslands and shrublands of the steppe form the northern transition zone to the Sahara desert in the south. A special feature of southwestern Morocco is the argan tree (*Argania spinosa*), which are endemic to this region and very appreciated for the production of consumable oil. The desert harbors only a sparse vegetation of C_4 plants (e.g., *Amaranthaceae*) and rarely CAM (Crassulacean Acid Metabolism) plants. Comparable to the steppe in the north, the Sahel constitutes the southern transition zone to the Sahara. The northern part of the Sahel consists of semi-desert grass-/ shrubland, whereas the southern part comprises *Acacia* wooded grassland and deciduous bushland. Opposite to the C_3 vegetation north of the Sahara, subtropical grass species of the Sahel are almost exclusively of C_4-type, which have an evolutionary advantage (relative to C_3 plants) under warm and arid climates (e.g., Ehleringer et al., 1997). The Sahel is most prone to climate perturbations, as evidenced by repeated severe droughts during the last century (Heinrigs and Perret, 2009; see also **Fig. 1.4**). Towards the tropics at lower latitudes, the

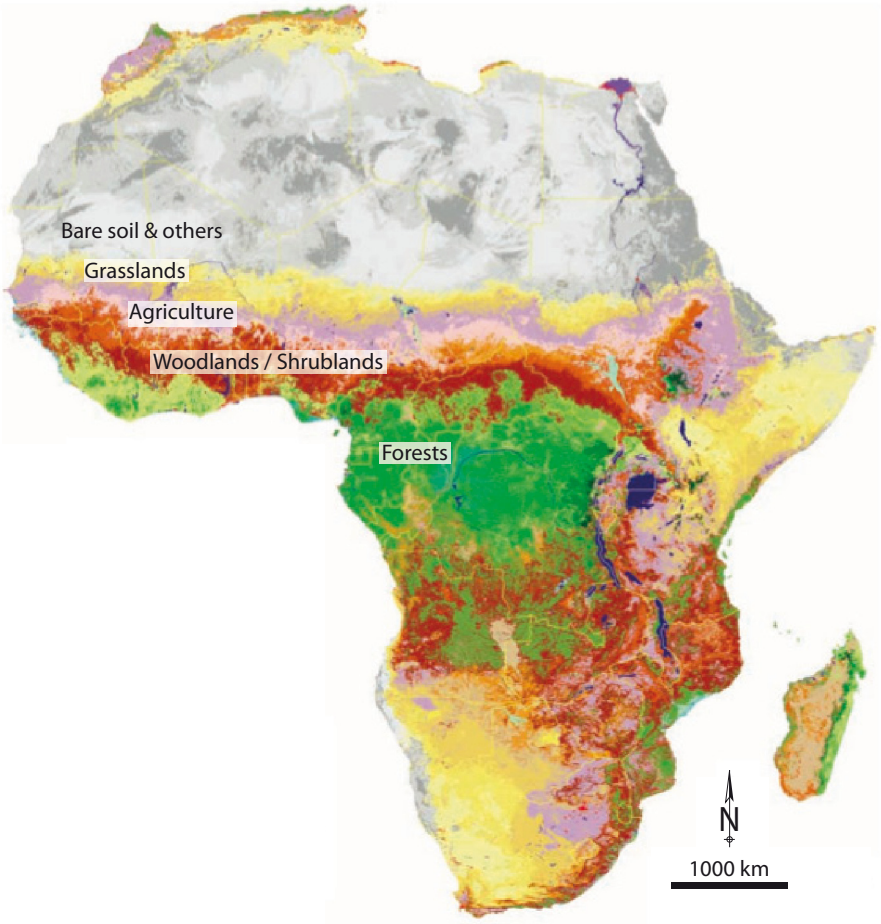

Fig. 1.3: Modern distribution of African biomes (modified after Mayaux et al., 2004). The detailed subdivision of the vegetation is simplified as indicated on the map.

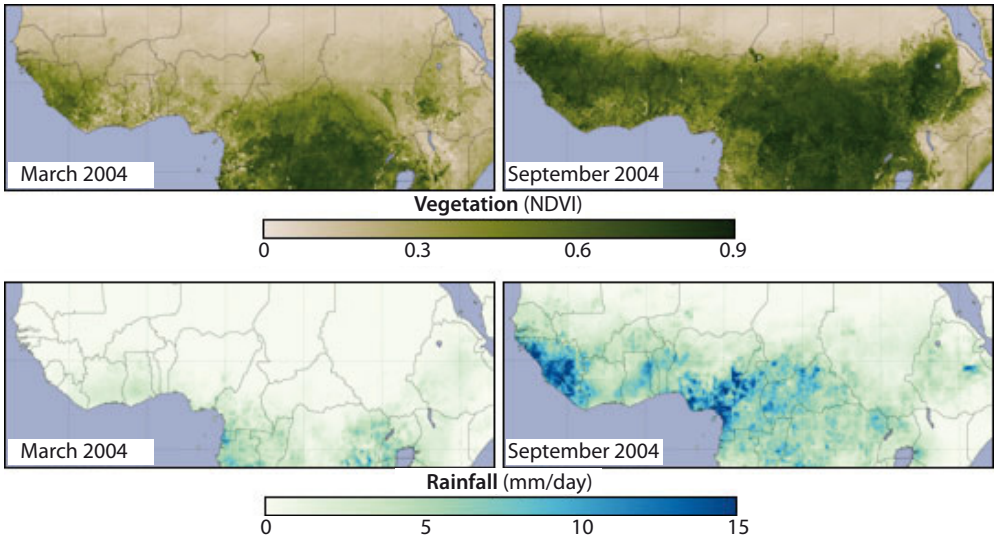

Fig. 1.4: Seasonal extremes in vegetaion (top) and rainfall (bottom) in sub-Saharan Africa: Boreal winter (left) vs. summer (right) (available at: www.earthobservatory.nasa.gov). NDVI, Normalized Difference Vegetation Index.

contributions of C_3 plants become dominant again in the Sudanian and Guinean vegetation belts, peaking in the Guinean and Congolian tropical rain forests. In addition, mangroves occur along the coastline in the vicinity of rivers.

1.1.3 Dust generation, transport and sedimentation

Atmospheric dust may influence the climate system by its feedbacks on the radiative balance, chemical interactions with other aerosols and by acting as natural fertilizer for terrestrial and marine ecosystems (Goudie and Middleton, 2001; Kohfeld and Harrison, 2001 and references therein). The Sahara is the largest desert in the world, covering an area of about 9,000,000 km^2 (equivalent to 33% of the whole African continent; Mayaux et al., 2004). As such, it is also the world‘s largest dust source, probably accounting for nearly half of the terrigenous material supplied to the world‘s oceans by aeolian transport (Goudie and Middleton, 2001). The spatial extent of atmospheric dust over Africa is well captured by satellite images derived from the Total Ozone Mapping Spectrometer (TOMS; **Fig. 1.5**), which provides a means to monitor dust outbreaks from the continent on a daily basis. Provenance studies on present-day dust samples are based on physical, chemical, mineralogical and isotopic properties of the aerosols combined with modern observational data, including backward air trajectories and satellite images (e.g., Chiapello et al., 1995, 1997; Moulin and Chiapello, 2004; Stuut et al., 2005; Meyer et al., 2011). While the grain size of dust particles has been shown to correlate with barometric pressure and wind speed in some areas (e.g., Clemens, 1998), the relationship is more complicated for the West African setting, since it became evident that grain size variations incorporate a combination of wind speed and the distance to the dust source (Stuut et al., 2005). Still, different grain size fractions can be attributed to different transport mechanisms (aeolian vs. fluvial) and carry different Sr isotopic signatures, linked to variations in chemical weathering intensity (Meyer et al., 2011).

As mentioned in section 1.1.1, the main wind systems over West Africa are the low-altitude NETW and the high-altitude AEJ. Aeolian transport of terrigenous material to the NE Atlantic offshore West Africa is mostly dominated by the NETW, in contrast to the long distance transport of the AEJ, which carries dust from the southern fringe of the Sahara and the Sahel westward across the Atlantic Ocean (e.g., Pye, 1987; Chiapello et al., 1995, 1997; Prospero, 1996; Ratmeyer et

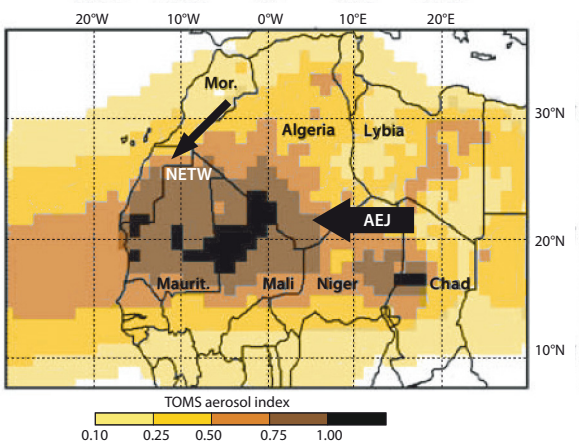

Fig. 1.5: Atmospheric dust over Africa and the adjacent Atlantic indicated by satellite-based daily images of the Total Ozone Mapping Spectrometer (TOMS) for the period 1979-2000 (modified after Moulin and Chiapello, 2004). Major wind systems are indicated (arrows). AEJ, African Easterly Jet; NETW, Northeast Trade Winds.

al., 1999a,b; Stuut et al., 2005). This NETW predominance is illustrated by a coherent NE-SW-striking trend in the spatial pattern of Sr-Nd isotopes in marine surface sediments (Grousset et al., 1998) and aerosols (Skonieczny et al., 2011), as well as in grain sizes (Stuut et al., 2005) and clay minerals (Lange, 1982). The seasonal variations are well assessed by the distinct temporal offsets in atmospheric dust concentrations at either side of the Atlantic Ocean, with a winter maximum in the east (proximal to the African continent), related to the NETW, and a summer maximum in the west, attributed to the long distance transport of the AEJ (Chiapello et al., 1995; Goudie and Middleton, 2001; **Fig. 1.6**). Both wind systems are responsible for the delivery of terrigenous organic material, including plant waxes, to the marine depositional environment (e.g., Simoneit et al., 1977; Gagosian et al., 1981; Huang et al., 2000; Schefuß et al., 2003a). Proximal to the coast, river discharge may contribute significantly to the accumulation of terrigenous material in marine sediments and the aeolian-derived fraction thus mixes with fluvial contributions (Holz et al., 2004; Huang et al., 2000). The comparison of Sr-Nd isotopes in dust and marine sediments even suggest that the terrigenous fraction is predominantly derived from major dust storms, which have the potential to integrate various dust sources from a large area, including Mauritania, Mali and southern Algeria (Skonieczny et al., 2011). In addition, the Bodélé depression in the central Sahara (near Lake Chad) constitutes another major dust source, as also seen in TOMS data (**Fig. 1.5**). Overall, the Sahel was identified as the major dust source for the supply of terrigenous material, including organic constituents, to the study area (ODP Site 659) in the adjacent NE Atlantic (Chiapello et al., 1995, 1997; Simoneit, 1997; Huang et al., 2000; Schefuß et al., 2003a). The multi-annual TOMS data (1979-2000) also demonstrates that dust outbreaks are likely determined by the vegetation dynamics immediate south of the Sahara, revealed by a large-scale correlation between drought events in the Sahel and increased dust export during the subsequent year (Moulin and Chiapello, 2004).

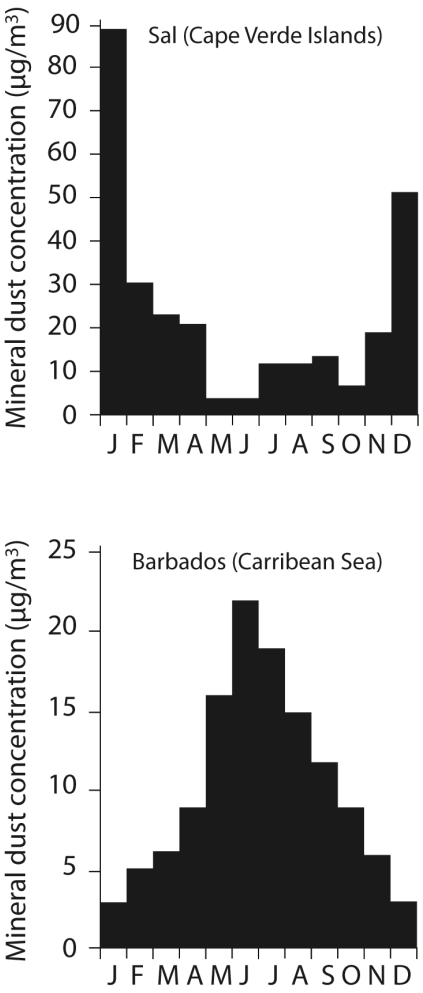

Fig. 1.6: Averaged dust concentrations measured at Sal (Cape Verde Islands) offshore West Africa and Barbados (Carribean Sea) for the periods 1992-1994 and 1973-1992, respectively (after Chiapello et al., 1995). The winter dust maximum at Sal is associated with the low-altitude NETW, which maximize in strength during winter. The summer dust maximum at Barbados is attributed to the long-distance transport by the AEJ, which is strongest in summer, carrying mineral dust across the Atlantic.

1.1.4 North Atlantic circulation

The main ocean surface currents offshore West Africa are mainly wind-driven and comprise the Canary Current, Guinea Current, North Equatorial Current and North Equatorial Counter Current (Sarnthein et al., 1982; Mittelstaedt, 1991; **Fig. 1.7**). The Canary Current is part of the Eastern Boundary Current of the subtropical North Atlantic Gyre, transporting cool waters southward along the West African continental margin to 25°N-20°N and continues southwestward, gradually merging into the North Equatorial Current. Coastal upwelling of cold and nutrient-rich waters in the Cape Blanc (permanent) and Cape Verde (seasonal) areas is linked to NETW intensity (Mittelstaedt, 1991). The North Equatorial Counter Current flows south of 10°N with an eastward direction, reaching a maximum in strength during summer and early fall. Close to the African continent, this current splits into a northern and eastward continuing component. The northern branch extends to ca. 14°N in early spring and propagates northward to 20°N until early fall, while the eastward continuation of the North Equatorial Counter Current is incorporated in the Guinea Current.

The western counterpart of the Canary Current is the Gulf Stream, which transports tropical waters from the Carribean Sea and tropical Atlantic towards higher latitudes. This inflow water is more saline than the surrouding North Atlantic water masses and is introduced to cooling, which further increases its density, resulting in deep-water formation in the northern North Atlantic (especially in the Barrents shelf area), regarded as the key position for AMOC initiation (and termination) and the global thermohaline circulation (e.g., Schmitz, 1995; Sarnthein et al., 2000). Sinking water masses lead to the displacement of deeper water masses and, consequently, maintain a southward flowing current comprising the North Atlantic Intermediate Water and North Atlantic Deep Water (NADW). A comparable situation is found in the Southern Hemisphere with the formation of Antarctic Intermediate Water and Antarctic Bottom Water (AABW), with the latter having the highest density, thus under-cutting the NADW by penetrating into the North Atlantic. Variations in AMOC strength are related to and thus detectable by latitudinal shifts of the contributing deep water masses and their distinctive chatracteristics recorded in deep-sea proxy records (Sarnthein et al., 1994; Vidal et al., 1997). NADW formation is associated with the transfer of heat and moisture

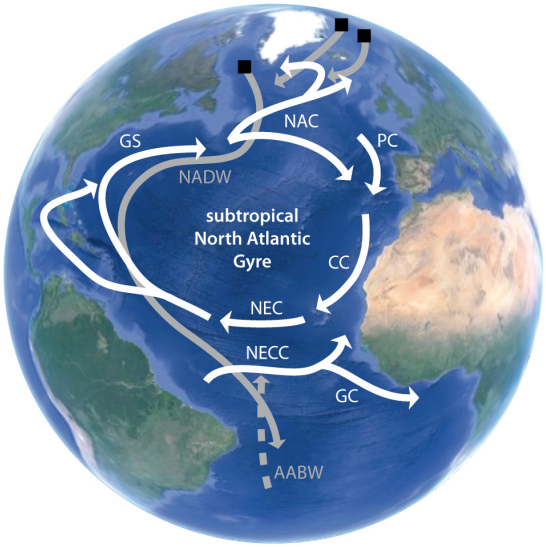

Fig. 1.7: North Atlantic circulation (simplified after Sarnthein et al., 1982, 2001). Major currents at the surface (white) and in the deep sea (grey, dashed) are indicated. CC, Canary Current; GC, Guinea Current; NEC, North Equatorial Current; NECC, North Equatorial Counter Current; GS, Gulf Stream; NAC, North Atlantic Current; PC, Portugal Current; AABW, Antarctic Bottom Water. Black squares indicate major locations of North Atlantic Deep-water (NADW) formation. Globe: Google Earth.

to the atmosphere, which contributes significantly to the relatively bland European climate of today (Berger et al. 1987).

Considering the depositional environment of the NE Atlantic, it has been shown that the potential displacement of the sinking terrigenous material by ocean currents is negligible in this setting, reflected by the coherent latitudinal distribution of vegetation belts and marine sedimentary pollen assemblages (Hooghiemstra and Agwu, 1986; Dupont and Agwu, 1991; Hooghiemstra et al., 2006) and stable carbon isotopes ($\delta^{13}C$) of plant waxes (Huang et al., 2000). Time-series data of sediment traps support these observations, indicating a significant correlation between the fluxes of organic carbon and lithogenic particles, with a fast and nearly unaffected sinking to the seafloor (Ratmeyer et al., 1999a,b).

1.2 Climate change and its implications over the past 5 Ma

1.2.1 The role of extra-terrestrial forcing

Explaining cyclical variations in proxy records is a basic challenge in paleoclimatology. It has become clear that the global climate system strongly depends on periodic and quasi-periodic variations in the Earth‘s orbital position and distance to the sun, with three main parameters determining the amount and distribution of sunlight received by the Earth: These include the shape of the Earth‘s orbit around the sun (eccentricity), the tilt of the Earth‘s axis of rotation (obliquity) and its tumbling (precession), which vary on timescales of 400/125 ka, 41 ka and 23/19 ka, respectively (**Fig. 1.8**; Hays et al., 1976; Berger, 1978; Berger and Loutre, 1991; Laskar et al., 1993, 2004). The Earth‘s current tilt is ca. 23.43°, but varies between 22.04° and 24.50° on the 41 ka obliquity cycle. Eccentricity (i.e., a more elliptical or circular orbit) modulates the amplitude of precession, with the latter controlling seasonal insolation intensities, as it shifts the occurrence (or positions) of seasons along the Earth‘s orbit. This causes a strengthening of the sesonal contrast in one hemisphere, while the other hemisphere experiences a decrease (**Fig 1.8**). The influence of precession is strongest at the equator and diminishes towards higher latitudes. Also obliquity influences the latitudinal distribution of insolation and thus seasonality, but in contrast to precession, it is (1) most pronounced at high latitudes and (2) has a symmetric effect on both hemispheres. Additional mechanisms related to, for instance, ice sheet and vegetation feedbacks can act as amplifiers of the orbital forcing (e.g., Willeit et al., 2013). The climatic influence of changes in solar activity is rather limited to shorter timescales and is likely a second-order effect (Bard and Frank, 2006). However, solar (11 a) and lunar (18.6 a) cycles have been demonstrated to influence the latitudinal temperature gradient (Davis and Brewer, 2011), which was recently supported by further empirical evidence (Soon and Legates, 2013).

Since the direct influence of eccentricity on insolation changes is considered too small (<0.1%) to explain the observed climate changes (the “100 ka problem”), “eccentricity-

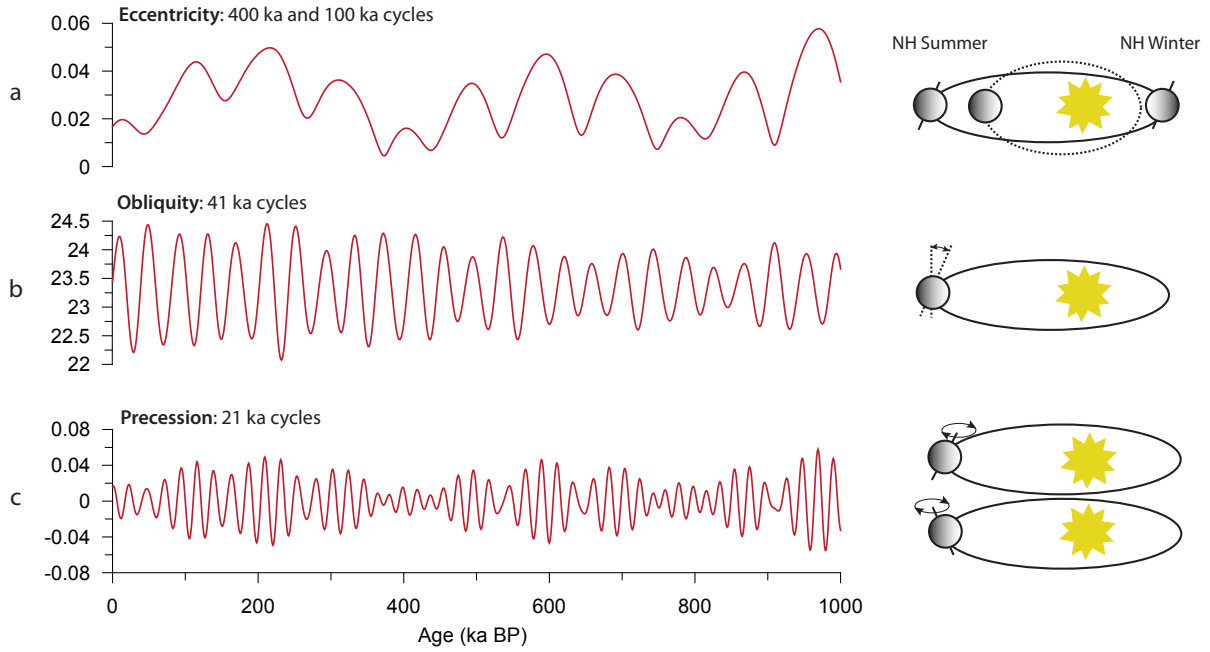

Fig. 1.8: Main orbital parameters of Earth for the last 1 Ma (Laskar et al., 2004). The variations result from the gravitational forces exerted by other celestial bodies on the Earth's orbit, affecting (a) eccentricity (near circular to elliptical orbit), (b) obliquity (tilt of Earth's axis of rotation) and (c) precession (wobble of the axis of rotation).

like" (100 ka) cycles in climate proxy records are typically ascribed to non-linear feedback mechanisms between insolation and the dynamic response of the internal components, like the atmosphere, oceans, ice sheets and lithosphere, rather than originating directly from eccentricity forcing (e.g., Imbrie et al., 1993; Shackleton, 2000). In contrast, it was also argued that the modulation of the precession cycle by eccentricity provides a sufficient indication for the presence of its low-frequency cycles in proxy data (e.g., Muller and MacDonald, 2002). Spectral analysis of the benthic $\delta^{18}O$ record from subtropical ODP Site 659 indicates that its eccentricity component derives from the preferential response to the warm phases of the eccentricity-modulated precession cycle, thus supporting the link between 400/125 ka cycles and eccentricity (Clemens and Tiedemann, 1997). Alternatively, Muller and MacDonald (e.g., 1995, 1997a,b,c) suggest that the low-frequency periodicity of 100 ka may even result from changes in the inclination of the Earth's orbit relative to the (invariable) plane of the solar system, and that eccentricity seems to affect climate only locally. This "inclination hypothesis" is based on the findings that inclination produces a single narrow spectral peak at 100 ka (as do many proxy records), withouth a 400 ka peak and solves their so-called "causality problem" (abrupt glacial terminations preceeded insolation-driven warming; see Karner and Muller, 2000). The authors note that the basic problem of this hypothesis is the fact that inclination has no influence on insolation, but maybe still on climate linked to the extraterrestrial accretion of meteoroids and dust within the invariable solar plane and its effect on insolation. However, the theory remains speculative, since there is

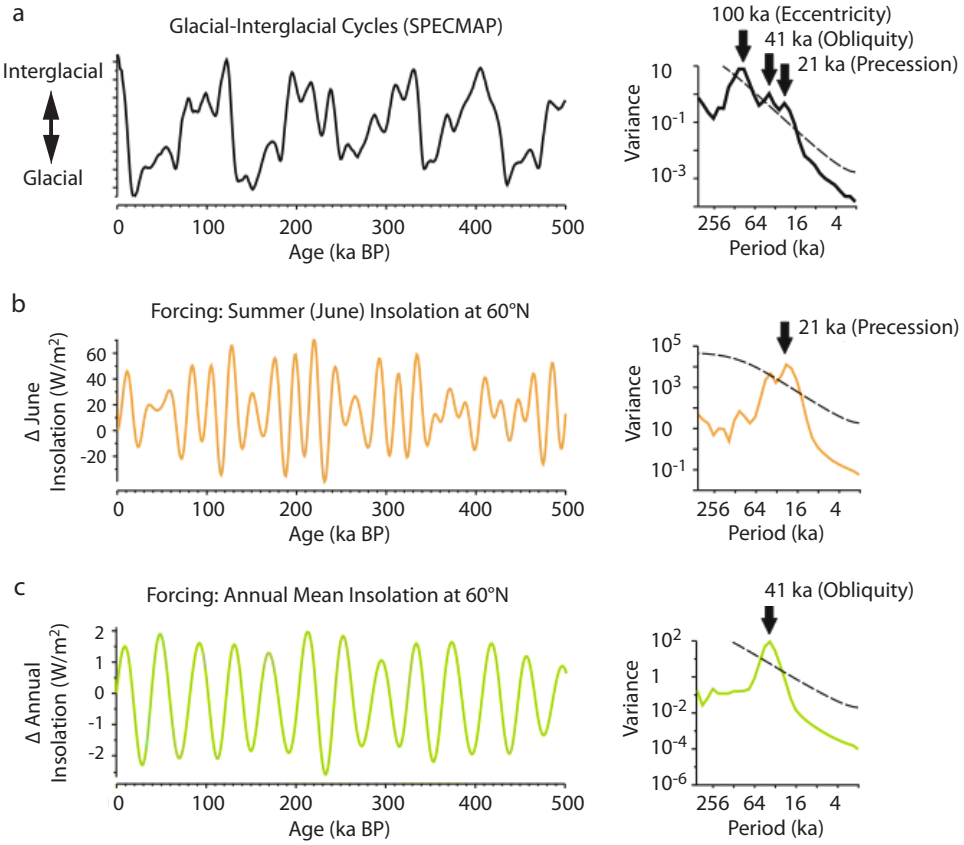

Fig. 1.9: Comparison of (a) simplified representation of glacial-interglacial cycles during the last 500 ka (SPECMAP; Imbrie et al., 1984) with two alternative orbital forcings, (b) high-latitude summer insolation and (c) annual mean insolation (after Davis and Brewer, 2009). The corresponding spectral analyses are shown on the right (after Torrence and Compo, 1998). While the SPECMAP record contains all main orbital cycles, high-latitude summer insolation is dominated by precession and cannot account for the obliquity signal in the record. Annual mean insolation is mainly controlled by obliquity, but the changes are very small. Equally, the eccentricity signal in the insolation parameters is weak, relative to the glacial-interglacial record.

no evidence for the presence of a meteoroid or dust band that captures all necessary features to imprint a 100 ka inclination signal on climate records (Muller and MacDonald, 1997c).

High-latitude summer insolation is generally regarded as the most influential orbital parameter, especially in driving glacial-interglacial cycles (e.g., Milankovich, 1930/1972; Imbrie et al., 1992, 1993; **Fig. 1.9**), though also winter insolation has been tentatively suggested as main cause of the high-latitude climate cycles during the late Pliocene and early Pleistocene (Muller and MacDonald, 2002). But still, since seasonal variations in insolation (summer and winter) are dominated at all latitudes by precession, it has become clear that the obliquity signal within the glacial record is difficult to explain by only assuming this forcing mechanism (the "41 ka problem"; see Muller and MacDonald, 2002; Raymo and Nisancioglu, 2003). Equally, mean annual insolation varies with obliquity, but its changes are considered too small to have an influence on climate (**Fig. 1.9**). Complementary to high latitudes, African monsoon variability on orbital timescales is mostly explained by variations in local summer insolation (e.g., Kutzbach, 1981; Rossignol-Strick, 1983; Kutzbach and Street-Perrott, 1985; Tiedemann et al., 1994; deMenocal, 1995, 2004; Gasse, 2006; Ruddiman, 2006; Trauth et al.,

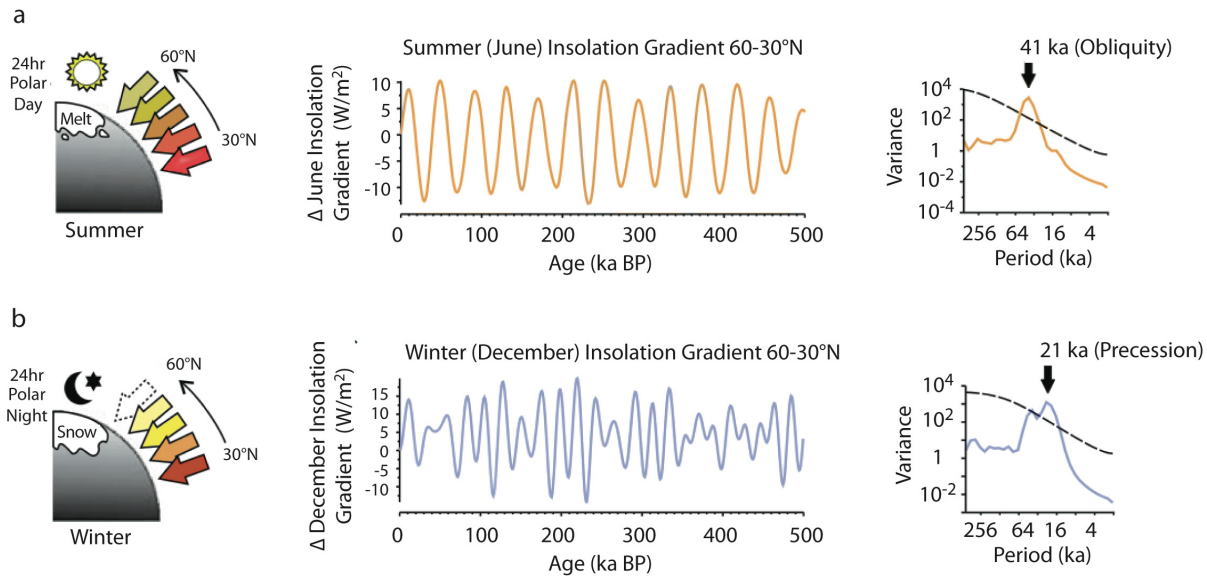

Fig. 1.10: The latitudinal insolation gradient (LIG) during (a) summer and (b) winter (after Davis and Brewer, 2009). Corresponding spectral analyses are displayed on the right (after Torrence and Compo, 1998). During summer, polar day conditions at high latitudes amplify the obliquity signal imprinted on the LIG. In contrast, polar night conditions during winter result in a dominant control of low-latitude insolation, which is dominated by precession, on the LIG.

2009; Larrasoaña et al., 2013). Maximum insolation intensities are thus expected to enhance the tropical monsoon circulation, analogous to modern seasonal variations (see section 1.1.1). Still, obliquity cycles are clearly evident in a number of low-latitude climate records, including Mediterranean sapropels (Lourens et al., 1996a), dust (Tiedemann et al., 1994) and pollen (Dupont et al., 1989) flux rates from West Africa, as well as Indian and East Asian monsoon records (Clemens and Prell, 2007). Considering African vegetation changes, a synthesis of pollen records revealed different forcing mechanisms, depending on the latitude (Dupont, 2011). As such, it was found that the tropical rain forests varied with precession-driven summer insolation, while the subtropical vegetation seems to be controlled by changes in obliquity and glacial boundary conditions (assumed for the 100 ka cycle). For the same reason as in the case of the glacial record, these observations are difficult to explain, since changes in obliquity have no considerable influence on low-latitude insolation (e.g., Laskar, 1990).

A plausible mechanism that incorporates (1) a strong obliquity signal, (2) high-amplitude changes and (3) the climatic linkage between low and high latitudes is found in the latitudinal insolation gradient (LIG) between high and low latitudes (e.g., Davis and Brewer, 2009; **Fig. 1.10**). This leads to differential heating between the cold polar regions and the hot tropics and creates the latitudinal temperature/pressure gradient, which ultimately controls the poleward heat and moisture transport, a mechanism that has been invoked in the so-called "gradient hypothesis" by Raymo and Nisancioglu (2003) to explain the strong obliquity rhythm of glacial-interglacial cycles between 0.8-3.0 Ma (the "41 ka world"). Interestingly, a comparison of temperature records from Antarctica and the tropical Pacific revealed coherent

changes in the obliquity band, for which changes in tropical heat export were considered to be in part responsible (Jouzel et al., 2007), as already suggested by Vimeux et al. (1999). Furthermore, also the Indian and East Asian monsoon systems are better correlated with obliquity than with precession, at least for the last 75 ka (Clemens and Prell, 2007). In this context, it is important to emphasize that obliquity changes are in phase between hemispheres, so that it appears plausible that the link between the climatic conditions of the northern/ southern high latitudes and the tropics is established by the LIG, which is dominated by obliquity during the summer season of each hemisphere (Raymo and Nisancioglu, 2003; Davis and Brewer, 2009). This is supported by recent climate models that simulate an enhanced mid-latitude eddy circulation (which is important for the heat and moisture transport from low to high latitudes) in response to low obliquity (and thus a strong summer LIG), and a concomitant shift of the poleward boundaries of the tropical rain belt towards the equator (Mantsis et al., 2014). It was also found that the orbital forcing associated with a change in obliquity is qualitatively (not mechanistically) analogous to global warming simulations (Kang and Lu, 2012) and El Niño Southern Oscillation (ENSO) heating scenarios (Lu et al., 2008). On the one hand, under high obliquity and global warming, the mid-latitude eddy activity weakens and the Hadley cell expands poleward and thus, a northward shift of the ITCZ, while on the other hand, low obliquity and ENSO heating shift the ITCZ towards the equator (Kang and Lu, 2012; Mantsis et al., 2014).

Considering the *strength* of interglacials, the Antarctic temperature record of the past 800 ka suggests that the phasing between precession and obliquity may serve as an explanation for their varying intensities (Jouzel et al., 2007). In this way, strong interglacials are expected to result from summer insolation maxima in-phase (within 5 ka) with obliquity maxima, while an anti-phasing between the two seems to have a compensating effect inducing weak interglacials. Specific focus on the *duration* of interglacials during the past 800 ka revealed that the onset of interglacials coincides with a maximum in boreal summer insolation (i.e., precession minimum), consistent with Milankovitch forcing (Milankovitch, 1941; Hays et al., 1976), while glacial inception occurred during decreasing obliquity and never after its minimum (Tzedakis et al., 2012). The authors emphasize the importance of the phase relationship between precession and obliquity for the persistence of interglacials over one or two insolation maxima, thus explaining interglacials with shorter (ca. 13 ka) and longer (ca. 28 ka) duration.

Further discussion on these topics, in light of the herein presented findings, can be found in sections 4.4.2 and 6.5, with the former having an emphasis on the variable presence of obliquity cycles in West African monsoon records and the latter providing a stronger focus on the phase relationships between precession and obliquity.

1.2.2 The Pliocene Epoch

The Pliocene Epoch (*Plio* more, *Cene* recent) comprises the time interval between 2.588 and 5.332 Ma and is a period of fundamental changes in the Earth's climate system, spanning the transition from globally warm conditions with low-amplitude variability to high-amplitude climate shifts associated with the onset of NHG (Dowsett et al., 2013).

The major climatic reorganization during the Pliocene is linked to the shoaling of the Central American Seaway (CAS) since ~4.8 Ma, which diverted warm saline waters from the western tropical Atlantic to the North Atlantic, enhancing the heat transport to northern high latitudes (Haug and Tiedemann, 1998; Steph et al., 2010). Further proxy evidence (Bartoli et al., 2005), as well as climate models (e.g., Prange and Schulz, 2004; Klocker et al., 2005; Lunt et al., 2008) confirm the role of the final CAS closure in triggering increased poleward heat transport and AMOC. It is argued that this led to increased humidity, which increased rainfall in NW Eurasia and runoff from Siberia, resulting in a freshening of the Arctic Ocean and finally, to the development of large ice sheets in the Northern Hemisphere ("Panama Hypothesis"; Driscoll and Haug, 1998) starting at ~3.3 Ma (Jansen et al., 2000; see next section). In contrast to future projections, the Pliocene world was marked by expanded tropical warm pools linked to reduced SST gradients (Brierley et al., 2009; Brierley and Fedorov, 2010; Dowsett et al., 2013) and enhanced tropical cyclone activity (Fedorov et al., 2010) and AMOC (Raymo et al., 1996), with the latter leading to warming of high-latitude surface waters (Bartoli et al., 2005). Increased Mediterranean outflow waters further contributed to AMOC strengthening (Khélifi et al., 2009).

The U.S. Geological Survey's Pliocene Research, Interpretation and Synoptic Mapping (PRISM) group focuses on the last time interval of global warmth in Earth's history, called the mid-Piacenzian Warm Period (MPWP; 3.025-3.264 Ma), with higher mean annual temperatures (~3°C) than pre-industrial levels, most pronounced at higher latitudes, and maximum sea level highstands of ~25 m (Haywood et al., 2002, 2009; Dowsett, 2007). This temperature increase was accompanied by only a small increase in pCO_2 (e.g., Raymo et al., 1996; Pagani et al., 2010), indicating a higher sensitivity of global warming to CO_2 levels than previously expected (Lunt et al., 2010; Pagani et al., 2010), likely due to underestimated feedback mechanisms linked to terrestrial ecosystems. The MPWP is of particular importance for paleoclimate studies, since most of the first-order boundary conditions were close to the modern situation, involving the geographic distribution of the continents and oceans, while also the flora and fauna was largely similar to today, thus permitting near-future-like paleo-reconstructions (Dowsett, 2007). In this way, the MPWP has been intensively investigated during the last two decades, providing various paleoenvironmental reconstructions (PRISM0 - PRISM5; Dowsett et al., 2013 and references therein). These data have been subsequently used for a series of climate models (e.g., Haywood et al., 2002, 2009; Haywood and Valdes, 2006; Salzmann et al., 2008, 2011; Lunt et al., 2010; Dolan et al., 2011; Dowsett et al., 2011; Sun et al., 2013; Willeit et al., 2013; Zhang et al., 2013a,b). Consequently, the Pliocene Model

Intercomparison Project (PlioMIP) was established as part of the Palaeoclimate Modelling Intercomparison Project (PMIP; Braconnot et al., 2007a,b). So far, uncertainties within these PlioMIP simulations are attributed to prescribed forcings and proxy data, indicating the need for a more tightly temporal and spacial data assessment. For instance, data-model mismatches for terrestrial temperature estimates in the tropical realm are likely due to limited proxy data (Salzmann et al., 2013). Equally, inconsistencies in tropical precipitation estimates (Haywood et al., 2013b) indicate the need for more data on tropical hydrology. Furthermore, it is also suggested to focus on near-modern orbital configurations, in order to improve the utility of the MPWP for a better characterization of the various aspects of a warmer-than-today climate, as well as to improve model evaluations (Haywood et al., 2013a). Thus, the next phase (PRISM4) of paleoenvironmental reconstructions will focus on Marine Isotope Stage (MIS) KM5c (KM5.3; 3.204-3.207 Ma), which was identified as a representative timeslice for warm conditions (interglacial) under a modern-like orbital setting.

1.2.3 Intensification of Northern Hemisphere Glaciations

Global ice volume mostly varied with 41 ka periodicities (related to the obliquity cycle) between 3.0 – 0.8 Ma, while after ~0.8 Ma, the 100 ka cycle (related to the eccentricity cycle) dominates (Imbrie et al., 1992). This poses a significant challenge to the paleoclimate community, since the traditional Milankovich theory (Milankovich, 1930/1972) suggests that changes in summer insolation at high latitudes (related to the 23 ka precession cycle) exerts the dominant control on the climate system (see section 1.2.1).

As recently suggested, geodynamic processes formed the initial cause in preconditioning the northern polar regions to sustain large-scale ice sheets, including the uplift of East Greenland to more than 3 km above sea level and its tectonic movement towards higher latitudes (Steinberger et al., 2015). Also, it is widely recognized that variations in Earth‘s orbit contribute to glaciation, the exact mechanisms still remain unsolved (Raymo and Huybers, 2008). In this way, various hypotheses have been proposed to explain the intensification of NHG at ~3 Ma (Mudelsee and Raymo, 2005; Raymo et al., 2006). These involve changes in pCO_2 (Berger and Wefer, 1996; Crowley and Kim, 1996; Raymo, 1998; Seki et al., 2010; Bartoli et al,. 2011) related to continental weathering (Raymo et al., 1988), increased stratification in high latitudes (Driscoll and Haug, 1998; Bartoli et al,. 2011), a more efficient biological pump (Haug et al., 1999) and/or shoaling of the tropical ocean thermocline (Philander and Fedorov, 2003). Other hypothesis include changes in ice-sheet dynamics (Thiede et al., 1998), ocean circulation (Billups et al., 1999; Bartoli et al., 2005) or ocean gateway closures (Haug and Tiedemann, 1998; Cane and Molnar, 2001) resulting in changes of oceanic heat and moisture transport or a mix of the above factors (Ravelo et al., 2004).

Marine sedimentary evidence for the onset of major NHG comes from the discharge of ice-rafted debris (IRD) of drifting icebergs originating from NE Greenland and the Arctic Ocean (e.g., Jansen et al., 2000; Bartoli et al., 2005). Recent analysis of the IRD fluxes and Pb-

isotope compositions indicate that the provenance of IRD was not constant and that North America was not a significant source, relative to Greenland and Europe, until 2.64 Ma (Bailey et al., 2013). Variations in IRD input covary with those in benthic $\delta^{18}O$ records, indicating that the latter is a suitable indicator for the waxing and waning of ice sheets (Raymo et al., 1989; Ruddiman et al., 1989b). It is important to note that, before 2.7 Ma, the degree to which changes in benthic $\delta^{18}O$ records can be attributed to either changes in deep-sea temperature and/or ice volume is uncertain, while both can be still related to high-latitude climate variability (e.g., Clemens and Tiedemann, 1997).

Interestingly, variations in IRD abundance also follow the succession of major events of the CAS closure with a persistent lag of 40 ka, which emphasizes significant memory effects in global climate, but also indicates that changes in eustatic sea level due to varying continental ice volume cannot have influenced the closure history of the CAS and thus, proofs the causality between the CAS closure and the onset of NHG (Sarnthein et al., 2009). Another mechanism that comes into consideration is based on model simulations, which reveal a strengthening of the Arctic Throughflow carrying low-saline and cold surface waters from the N Pacific through the Bering Strait as a result of the CAS closure (Sarnthein et al., 2009). It is suggested that these freshwater fluxes have readily compensated the increased heat transport, leading to cooling, sea ice expansion and higher albedo ~3.2-3.0 Ma and consequently, the intensification of NHG, first maximizing ~2.82 Ma. The cooling process likely involved a positive feedback identified as the thermal isolation of Greenland from the poleward heat transport (Sarnthein et al., 2009).

The intensification of NHG has led to stronger NETW and thereby to enhanced upwelling (Marlow et al., 2000; Steph et al., 2010). In this way, most of the major coastal (wind-driven) upwelling regions were marked by increased diatom and opal production during global cooling (Etourneau et al., 2012). In addition, the heat redistribution in the Atlantic Ocean due to the CAS closure resulted in the so-called upwelling seesaw, i.e. intensified (weakened) upwelling off SW (NW) Africa, controlled by interhemispheric heat transfer linked to AMOC (Prange and Schulz, 2004).

The implications of an enhanced AMOC on NHG have been first accounted for by Driscoll and Haug (1998), related to their “Panama Hypothesis”. This theory attempts to reconcile the effects of counteracting forcings, i.e. increased heat *and* moisture transport following the CAS closure. The authors suggest that heating of the North Atlantic at high latitudes acts to enhance evaporation and moisture transport (via westerlies), followed by increased river discharge from northern Eurasia, leading to sea ice extension and, in turn, to higher albedo, thus preconditioning the growth of ice sheets in the Northern Hemisphere. Climate models have still shown that these forcings appear too weak to trigger major glaciations (Klocker et al., 2005; Lunt et al., 2008). However, these models are seen with caution due to large uncertainties related to sea ice cover and associated changes in albedo (Sarnthein et al., 2009). Another mechanism is related to the progressive increase in obliquity amplitudes between 3.1

and 2.5 Ma, which has been suggested as final cause for the intensification of NHG (Haug and Tiedemann, 1998). The authors argue that low obliquity results in colder summer conditions at high latitudes, which is a prerequisite to prevent snow melt and thus, favors ice sheet growth.

Recently, a compilation of marine and terrestrial records identified four globally evident glaciation events that occurred already prior to the intensification of NHG (De Schepper et al., 2014). These comprise two events in the early Pliocene (~4.9-4.8 Ma and ~4.0 Ma), one event close to the early/late Pliocene boundary (~3.6 Ma) and during MIS M2 (~3.3 Ma). Based on the global data synthesis, it is not clear what caused the earlier glacial events during the Pliocene, whereas it seems that the glaciation at 3.3 Ma was linked to ocean gateways (like the CAS) and its subsequent intensification during the latest Pliocene most likely resulted from the decline in pCO_2 (De Schepper et al., 2014).

1.2.4 The Last Glacial cycle

During the last 130 ka, the Last Glacial Maximum (LGM; 18-23 ka) was the most recent period when global ice volume reached its maximum (e.g., Mix et al., 2001). During the LGM, most proxy records from both hemispheres indicate generally cooler and drier conditions than today (Gasse, 2000; Gasse et al., 2008), along with ca. 100ppmv lower than pre-industrial CO_2 levels (Sigman and Boyle, 2000) and a ca. 120 m lowered sea level (Waelbroeck et al., 2002). Climate models simulate a damped global hydrologic cycle relative to today, with decreasing precipitation in most of the tropics (Pinot et al., 1999; Braconnot et al., 2000), in line with proxy data (Gasse, 2000). In contrast, the African Humid Period (AHP; ~5-11 ka) was the last time interval with exceptionally warmer and wetter conditions (deMenocal et al., 2000; Weldeab et al., 2007; Tjallingii et al., 2008; Tierney and deMenocal, 2013). During the AHP, large parts of the modern hyper-arid Sahara desert featured numerous lakes, and more humid conditions sustained a diverse ecosystem consisting of savanna grasslands, tropical forests and shrubs (Gasse, 2000; Hooghiemstra et al., 2006). Interestingly, these climate shifts occurred synchronous in northern and southern Africa (Collins et al., 2011).

Comparable to the AHP, model simulations and proxy data (grain-size-based humidity index) indicate recurrent humid conditions during the Last Glacial cycle and suggest abrupt expansion and retreat of subtropical grasslands (mostly C_4 plants) into the Sahara, which were primarily attributed to precession-driven insolation forcing (Tjallingii et al., 2008). These humid periods were also accompanied by expansions of tropical C_3 plants during MIS 3 (~45-50 ka) and MIS 5 (~110-120 ka), based on a marine plant-wax $\delta^{13}C$ record (Castañeda et al., 2009). In addition to the local insolation forcing, West African monsoon records revealed a high sensitivity to high-latitude climate variability or more precisely, climate instability, such as during deglaciation periods, explained by atmospheric teleconnections (e.g., greenhouse gases; Weldeab et al., 2007).

Short-term, but large-amplitude climate shifts have also been identified in the course of the Last Glacial cycle and are seen as the result of abrupt N Atlantic cooling (Dansgaard-Oeschger Events; Bond et al., 1993; Dansgaard et al., 1993) during deglacial melting and the rafting of icebergs associated with maxima in IRD abundance (Heinrich Events; Bond et al., 1992). Such events have a strong impact on ocean circulation, leading to a weakening of the AMOC, like during Heinrich Event H1 (17.5 ka; McManus et al., 2004), for which severe drought in the Afro-Asian monsoon region is reported (e.g., Stager et al., 2011). Earlier works already suggested the potential link between reduced NADW formation and reduced precipitation in the Sahel, inferred from lake-level fluctuations in East Africa (Street-Perrott and Perrott, 1990). Further evidence is based on the comparison of major elemental ratios (Mulitza et al., 2008) with alkenone-derived SST and benthic $\delta^{13}C$ records spanning the last 44 ka (covering H1-H4), which revealed that millennial-scale droughts in the Sahel were not induced by SST changes in the tropical NE Atlantic, but rather linked to cooling of the N Atlantic at high latitudes (Heinrich events) associated with a reduced AMOC (Niedermeyer et al., 2009). Such a remote northern high-latitude forcing was even detected in SE Africa (Schefuß et al., 2011). This supports previous model and proxy results, indicating that abrupt high-latitude climate events trigger simultaneous aridification in West Africa (Tjallingii et al., 2008). Other results extend this relationship for the last 192 ka and indicate a strong influence of AMOC variations (or more generally, high-latitude climate changes) on West African monsoon variability (Castañeda et al., 2009). Notably, these vegetation shifts were unrelated to changes in local summer insolation. Equally, it was found that central African hydrology is strongly affected by the subtropical-tropical SST gradient (Schefuß et al., 2005) and the land-ocean temperature (and thus pressure) contrast (Weijers et al., 2007), whereas other proxy records indicate persistent insolation forcing of humidity changes in the Sahel during the Last Glacial cycle (Tjallingii et al., 2008; Niedermeyer et al., 2010), similar as it was deduced for SW Africa (Collins et al., 2014).

1.2.5 Implications for hominin evolution and migration

The relevance of environmental change in hominin evolution over the past 6 Ma is a permanent subject of debate (e.g., deMenocal, 1995; White et al., 2009; Cerling et al., 2011). In general, archeological and fossil evidence point to recurrent occupation of the Sahara since the late Miocene (Larrasoaña et al., 2013 and references therein), while it is also largely accepted that anatomically modern humans (*Homo sapiens*) evolved around 150-200 ka in sub-Saharan Africa (e.g., McDougall et al., 2005). One main problem is that the fossil record becomes more fragmentary with increasing age. In this way, human occupation of the entire Sahara during the AHP is documented by widespread archeological evidence, whereas Earlier and Middle Stone Age relicts are far less frequent than Neolithic ones. Scattered remains throughout the Sahara also indicate the presence of humans before 0.5 Ma, but older evidence is restricted to a few well-dated sites of the Early Stone Age in Ain Hanech and El-Kherba in

Algeria (1.7-1.8 Ma) and to fossil hominin remains in Koro Toro (3.5-3.7 Ma) and Toros Menalla (6.9-7.3 Ma; both North Chad basin). The common feature of all these sites is that they were associated with more humid conditions (Larrasoaña et al., 2013 and references therein).

A recent compilation of paleoenvironmental data from Africa clearly proofs the high relevance of the West African monsoon system for the greening of the Sahara (Larrasoaña et al., 2013). This is further illustrated by the existence of several fossil (and buried) river channels extending across the Sahara to the Mediterranean coast (detected by space-born radar images), which have been shown to originate from south of the Sahara between 117-130 ka (Osborne et al., 2008). Such humid corridors connected the sub-Saharan environments with North Africa and provided migration pathways that allowed the dispersal of *H. sapiens* out of Africa (Balter, 2011). These were particularly important during moderate humid periods, in order to enable the dispersal of humans across the Sahara (Larrasoaña et al., 2013). The C_3 expansions that are evident throughout the Last Glacial cycle also correlate with major periods of hominin migration between 40-60 ka and 90-120 ka (Castañeda et al., 2009). An alternative out-of-Africa hypothesis favors the migration along coastlines, which means hominins would have been able to circumvent the high degree of habitat fragmentation faced by inland populations during extremely variable climate conditions (Stringer, 2000).

Overall, the recurrent greening and drying of the Sahara likely provided the necessary habitat for hominin population dynamics, when considering the large areal extent of the North African savannas under humid conditions, followed by a relatively fast (2-3 ka), mosaic-like fragmentation due to aridification (Larrasoaña et al., 2013). Changes in African climate, vegetation and faunal assemblages have been shown to be roughly synchronous during the Pliocene and Pleistocene (deMenocal, 2004). In this way, periods of extreme climate variability, as such associated with high eccentricity/precession, have been suggested as triggers for evolutionary speciation and dispersal (Trauth et al., 2007, 2009), according to the variability selection hypothesis. Opposed to this is the habitat-specific hypothesis, focusing on the establishment of open landscapes, which influenced hominin evolution and behavior (see deMenocal, 2004). Complementary to the climatic impact on speciation events during the Pliocene and Pleistocene (deMenocal, 1995), also the cultural behavior of humans during the late Holocene shows immediate responses to climate perturbations like droughts, leading to population displacement and even the collapse of states (deMenocal, 2001).

II

Scientific objectives, approach and outline

2.1 Rationale and approach

Overall, little is known about the development of tropical hydrology and the associated vegetation changes during the Pliocene. The well-known dust records off West Africa display periodically alternating arid-humid cycles, which have been interpreted to reflect different forcings (deMenocal and Rind, 1993; Tiedemann et al., 1994; deMenocal, 1995, 2004): Throughout the last 2.4 Ma, North Atlantic SST variations are generally considered as main driver of humidity changes, owing to the large-amplitude climate variability at high latitudes associated with glacial-interglacial cycles, while prior to 2.4 Ma, i.e., before the intensification of NHG, low-latitude summer insolation dominated. However, a statistical reassessment of the paleo-environmental significance of the dust records revealed that they are rather indicators for the transition from humid to (hyper-)arid conditions, instead of directly recording aridity (Trauth et al., 2009), in line with modern observations (Prospero et al., 2002). This is also linked to the potential of highly localized dust sources to create the apparent impression of large-scale continental aridity (Prospero et al., 2002). In contrast to previous conclusions (e.g., deMenocal, 1995, 2004), Trauth et al. (2009) suggested a decoupling of the tropical African climate variability from the onset and intensification of NHG, since eccentricity-modulated precession forcing is evident back to 5 Ma. This seems to be in contrast to other findings that indicate a clear link between AMOC (which is strongly influenced by varying ice sheets) and West African climate (e.g., Mulitza et al., 2008; Castañeda et al., 2009; Niedermeyer et al., 2009). In this way, it becomes clear that more insights are necessary to strengthen our understanding of orbital-scale changes of the West African monsoon system. The hydrogen isotopic composition of plant waxes (δD_{wax}) enables the assessment of these variations, since it is tightly coupled to the hydrologic regime (see below).

According to the generally warmer and wetter mean climate state during the Pliocene, it can be expected that terrestrial environments from low latitudes indicate more humid conditions and expansion of tropical vegetation, such as rainforest and tree savanna, during this time interval. Pollen records provide detailed insights into vegetation composition and indicate repeated northward extensions of woodland and savanna during the Mid-Pliocene, while the composition was unlike the modern vegetation (Leroy and Dupont, 1994; Vallé et al., 2014). Complementary to pollen, the $\delta^{13}C$ signature of plant waxes indicates shifts

between C_3 and C_4 plants (e.g., Collister et al., 1994). In East Africa, it has been shown that the Pliocene-Pleistocene grassland expansion was not associated with an increase in C_4 biomass (Feakins et al., 2013), while in Southwest Africa, C_4 grass expansion was triggered by increased fire activity during the Miocene (Hötzel et al., 2013). For West Africa, however, the timing of C_4 grass expansion and its causes is still unknown. Plant-wax $\delta^{13}C$ ($\delta^{13}C_{wax}$) is a suitable proxy for C_3/C_4 contributions in West Africa, as evidenced in marine surface sediments (Huang et al., 2000) and aerosols (Schefuß et al., 2003a), which are both in good agreement with pollen data (Dupont and Agwu, 1991), all indicating the distribution of African biomes.

The overall aim of this thesis is to provide new insights into the paleo-hydrologic evolution of West Africa during two Pliocene time intervals (3.0-3.6 Ma and 4.6-5.0 Ma) and the whole Last Glacial cycle (last 130 ka) by a combination of $\delta^{13}C_{wax}$ and δD_{wax} records from well-dated continuous marine archives retrieved in the subtropical NE Atlantic. Considering the paleoclimatic background described so far, the following hypotheses formed the initial basis for the accomplishment of the thesis:

I. The MPWP is the result of the CAS closure, redirecting warm tropical waters to the North Atlantic and, in turn, causing elevated humidity and extensions of woodlands and forest biomes in West Africa.
II. West African aridity and vegetation changes are mainly driven by AMOC variations, as postulated by Mulitza et al. (2008), Castañeda et al. (2009), Niedermeyer et al. (2009) and others.

In detail, the following questions were addressed:

1. Was the MPWP characterized by a generally warmer and wetter West African climate or were arid events just less intense?
2. Were AMOC reductions during the MPWP related to increases in African aridity?
3. Was the time interval preceding the MPWP even warmer and wetter in West Africa?
4. What were the triggers of dust export events and how do they relate to West African climate variability?
5. When did the modern West African savanna develop?
6. Before the CAS closure, i.e., before intensification of the AMOC, was West Africa generally drier and less vegetated?

These hypotheses and questions were tested by a comparison of the Pliocene development of vegetation and continental hydrology in West Africa before and during the MPWP, that is before and during the final CAS closure and before NHG intensified, i.e., without influence of large Northern Hemisphere ice sheets. The Last Glacial cycle (last 130 ka) was similarly analyzed to generate a benchmark for the evaluation of Pliocene environmental changes against glacial-interglacial conditions recorded at the same core position.

Initially, it was intended to compare the plant-wax isotopic data with sea surface temperature (SST) estimates from the same sediments, in order to investigate the influence of oceanographic changes on West African hydrology. While this was achieved for the Last Glacial cycle (Chapter III), the Pliocene samples (Chapter IV) unfortunately yielded insufficient material for reliable SST reconstructions. In order to compensate for this lack, an alternative approach was conducted on marine surface sediments (Chapter V), which serves as a proxy calibration study for the regional setting of West Africa by addressing the following questions:

1. How is the relationship between δD_{wax} and the isotopic signature of precipitation?
2. Are there additional (and detectable) influences on δD_{wax} unrelated to those of precipitation?
3. Does the isotopic composition of different long-chain *n*-alkanes record the same environmental signal in terms of hydrology (δD_{wax}) and vegetation ($\delta^{13}C_{wax}$)?

2.2 Materials and methods

Materials and methods are briefly introduced in the following, while analytical procedures are detailed in each Methods section of Chapters III, IV and V.

2.2.1 Core locations

Paleoclimate studies presented in this thesis (Chapter III and IV) are based on a deep-sea drilling core retrieved at Ocean Drilling Program (ODP) Site 659 (18°05'N; 21°02'W), which is located approximately 300 km offshore West Africa at the top of the sub-marine Cape Verde Plateau in 3070 m water depth. The core was retrieved during ODP Leg 108 (ODP Sites 657-661) as a non-upwelling reference site relative to ODP Site 658 located within a major upwelling cell near Cape Blanc (Ruddiman et al., 1989a). Since ODP Site 659 was considered to reflect the general development of West African climate, attributed to its strategic position beneath the main dust-bearing wind systems (Ruddiman et al., 1989a; Tiedemann et al., 1989), many studies have focused on these records (e.g., Tiedemann et al., 1994; deMenocal, 1995, 2004; Tiedemann and Clemens, 1997; Haug and Tiedemann, 1998; Clemens, 1999; Zachos et al., 2001; Trauth et al., 2009; Nie, 2011; Vallé et al., 2014). Preliminary lipid analysis, though carried out on just one sample, indicated a generally poor preservation of organic matter at this site, while resistent compounds, mainly long-chain *n*-alkanes derived from plant waxes, made up the majority of extractable lipids (ten Haven et al., 1989). This already revealed the high potential for further plant-wax analyses on these sediments, which are presented in the following chapters.

The calibration study (Chapter V) uses 57 samples of marine surface sediments (coretops), which were recovered by multicorer during cruises M53/1 (2002), M58/2 (2003), M65/1

(2005) and MSM11/2 (2009) of the German research vessels Meteor (M) and Maria S. Merian (MSM). In total, the available sample material covers a N-S-transect along the West African continental margin between Morocco (31°N) and Guinea (9°N). In addition, the diverse locations of the coretops within various water depths (18-4167 m) and distances to the coast (15-400 km) provide a good basis for the evaluation of the spatial distribution patterns of plant-wax isotopic signatures offshore West Africa.

2.2.2 Age models of ODP Site 659

The marine sedimentary record of ODP Site 659 has an astronomically calibrated timescale back to 5 Ma, which was initially established based on $\delta^{18}O$ of benthic foraminifera (Sarnthein and Tiedemann, 1989). Given the low-amplitude variability of the Pliocene benthic $\delta^{18}O$ record, the dust record was then used for fine-tuning the timescale before 2.85 Ma to the precession cycle/local summer insolation (hereafter termed T94 age model), which is regarded as the main forcing of West African aridity changes (Tiedemann et al., 1994). Later on, the Pliocene timescale has been readjusted by Clemens (1999), focusing again on benthic $\delta^{18}O$ for tuning (hereafter termed T94R age model).

A main concern about orbital tuning strategies in general is related to the necessary assumption of a climate model (or forcing) for the attribution of cyclical changes in proxy records to similar variations in orbital parameters (like local summer insolation), meaning that tuning approaches have a potentially circular effect, if the tuned proxy data is used to confirm the climate model used for tuning (Muller and MacDonald, 1997b). But still, strong evidence for orbital cyclicity derives from spectral analyses of (untuned) $\delta^{18}O$ records from deep-sea sediments (e.g., Muller and MacDonald, 1997a,b). In terms of the T94 age model, it was found that the statistical significance of the main spectral peak in the untuned record was reduced after tuning, interpreted as an indication for overtuning (Muller and MacDonald, 2002). In general, these authors are very critical when it comes to orbital tuning strategies (see also section 1.4.1), based on their statement that it appears risky to assume a fixed forcing mechanism of the climate system, as mentioned above (the circular effect). In this way, the suggested persistence of local insolation forcing of African climate (Trauth et al., 2009) may be related to the age model of the investigated record, which is based on tuning to precession (Tiedemann et al., 1994). Most important is the observation that there is no fixed (orbital) forcing through time, such as the dominant 41 ka cycle before and the 100 ka cycle after the mid-Pleistocene transition (~0.8 Ma), meaning that "we must look at the data again, as if for the first time, regard climate to be multidimensional, and be open to new ideas unbiased by our prior theoretical prejudices" (Karner and Muller, 2000; p. 2144).

For the Last Glacial cycle (Chapter III), the Ti/Ca ratio is used for fine-tuning of the ODP 659 record to the same element ratio of a nearby sediment core, which has a radiocarbon-based age model and yields the same variations. For the Pliocene (Chapter IV), the revised age model T94R was chosen, since it better matches the benthic $\delta^{18}O$ stack (LR04; Lisiecki

and Raymo, 2005). which is used for the δD correction for changes in global ice volume. The correction is obviously more important for the Last Glacial cycle record with large fluctuations in NH ice sheets (~8‰ when converted to δD values), while for the Pliocene, it is almost negligible (in the range of ±2‰). However, as a matter of consistency, the procedure (δD adjustment) determines the use of the T94R age model (Clemens, 1999), in order to achieve a proper comparison between the Pliocene and the Last Glacial cycle records.

2.2.3 X-ray fluorescence (XRF) scanning for major element distribution

X-ray fluorescence (XRF) scanning provides a non-destructive tool to measure the element composition at the split core sediment surface at high spatial resolution (Röhl and Abrahams, 2000; Tjallingii et al., 2007). Elemental ratios presented in this thesis are the titanium/calcium (Ti/Ca) and aluminium/silicium ratios (Al/Si), used as indiator for aeolian transport (Ti/Ca) and weathering intensity (Al/Si) in Chapter III.

In general, the major elemental composition is influenced by contributions from different sources and their environmental conditions. The Ca content is mainly assigned to marine carbonates in the study area (Tiedemann et al., 1989, 1994; Govin et al., 2012), while Ti is typical for Saharan dust (e.g., Nicolás et al., 2008). Equally, Si is the major constituent in mineral dust, mostly bound in quartz grains (Scheuvens et al., 2013). Biogenic opal as a potential source for Si can be excluded, since opal concentrations are considered negligible at ODP Site 659 (Tiedemann et al., 1989). High Al contents are characteristic for deeply weathered soils under warm and humid conditions (Gac and Kane, 1986). The Al/Si ratio has been proven successfully in this area as a humidity indicator (Mulitza et al., 2008), though in this case, it was also linked to discharge from the Senegal River. Recently, the Ti/Ca ratio has been correlated to dust input at ODP Site 659 (Vallé et al., 2014).

2.2.4 Alkenone-based ($U^{k'}_{37}$) sea-surface temperatures

Alkenones are long-chained mono-ketones originating from the ubiquitous haptophyte algae *Emiliania huxleyi* and related species, which live within the photic zone (Volkman et al., 1980; Marlowe, 1984). The global occurrence and persistence of alkenones throughout the geological record (Marlowe et al., 1990) make them a valuable paleoceanographic tool. Many calibration studies have investigated the relationship between alkenones produced by the algae and its growth temperature (see review by Conte et al., 2006). However, clear differences have been detected between sea surface and coretop data. It was found that the exact water depth may vary, as does growth rate and seasonal blooms, all of which bias the relationship. In addition, lateral advection and extreme temperature gradients may cause significant bias in the calibration of alkenones as a paleothermometer. In contrast to the data obtained from sea surfaces, the coretop calibration yielded a robust linear correlation with mean annual SST (Conte et al., 2006).

The application of the alkenone unsaturation index ($U^{k'}_{37}$) for estimating SST is based on the ratio between the di- and triunsaturated C_{37} alkenones (Prahl and Wakeham, 1987), which is defined as

$$U^{k'}_{37} = [37:2]/[37:2 + 37:3].$$

In this thesis, SST estimates are used in Chapter III and were obtained from the global coretop calibration after Müller et al. (1998) with

$$SST\ (°C) = (U^{k'}_{37} - 0.044)/0.033.$$

2.2.5 Plant-wax-derived long-chain n-alkanes

Land plants cover their leaves with waxes as protection against external stress (e.g., Samuels et al., 2008). These wax coatings contain, among others, long-chain *n*-alkanes with an odd-over-even carbon number (C_{25}-C_{35}) predominance (Chibnall et al., 1934; Eglinton and Hamilton, 1967), conventionally given as the carbon preference index (CPI) with commonly values above 3 for plant-wax-derived *n*-alkanes (e.g., Collister et al., 1994). Since these compounds are meant to be stable, *n*-alkanes remain intact during transport by winds and rivers and after final deposition (Eglinton and Eglinton, 2008). Their resistance to degradation and diagenetic effects leading to isotope exchange (e.g., Sessions et al., 2004; Schimmelmann et al., 2006) constitutes their increasing application in paleoclimate studies. In addition to CPI, *n*-alkane distributions can also be expressed with regard to their average chain-length (ACL; Poynter et al., 1989). For instance, C_4 grasses have a characteristic lipid distribution dominated by the *n*-C_{31} and *n*-C_{33} alkanes, while most trees maximize at the *n*-C_{29} alkane (Rommerskirchen et al., 2006a,b; Vogts et al., 2009). Varying abundances of these compounds may therefore provide an indication for vegetation changes.

In general, variations in plant-wax concentrations can be related to two main aspects: Changes in wind strength and/or vegetation cover. Since the terrigenous fraction at ODP Site 659 is considered to be purely aeolian in origin (Tiedemann et al., 1989), the concentrations of marine sedimentary plant waxes is likely more influenced by wind strength than changes in the extent of the vegetation cover. This is constrained by a comparison of the herein generated results with the available dust record (Tiedemann et al., 1989, 1994).

2.2.6 Plant-wax $\delta^{13}C$ as vegetation proxy

The $\delta^{13}C$ signature of plant-wax-derived *n*-alkanes ($\delta^{13}C_{wax}$) is primarily determined by the photosynthetic pathway and associated differences in plant physiology (e.g., Collister et al., 1994). While the C_3-type, the evolutionary more primitive C-fixation pathway, leads to a $\delta^{13}C_{wax}$ in the range of −32‰ to −39‰, the C_4-type results in more enriched values within a range of about −18‰ to −25‰ (Rieley et al., 1991, 1993; Collister et al., 1994;

Rommerskirchen et al., 2006a,b; Vogts et al., 2009). This is related to various structural and biochemical modifications of the evolutionary older C_3 pathway, which resulted in a more efficient photosynthesis, including an improved CO_2-concentrating mechanism (Ehleringer et al., 1997; Tipple and Pagani, 2007). The earliest origin of C_4 photosynthesis still remain tentative, given the lack of fossil evidence. Overall, low CO_2 levels appear as the initial evolutionary pressure on plants to develop a mechanism to store CO_2 more effectively, implemented by the C_4 pathway. However, the geographical expansion of C_4 plants (mainly grasses) since the Miocene was not globally synchronous, indicating regionally different triggers (Tipple and Pagani, 2007; Edwards et al., 2010; Strömberg, 2011). It was suggested that increased aridity and associated wildfire activity would lead to clearing of large areas, thus providing new habitats for C_4 plants (Ehleringer et al., 1997). Indeed, this was first evidenced by a combination of pollen, $\delta^{13}C_{wax}$ and microscopic charcoal data from southwestern Africa, indicating a clear link between fire occurrence and C_4 grass expansion during the Miocene and Pliocene (Hötzel et al., 2013).

However, further studies revealed that $\delta^{13}C_{wax}$-based estimates of C_3/C_4 contributions are afflicted with huge uncertainties, considering the large $\delta^{13}C_{wax}$ variability observed for modern plants (Castañeda et al., 2009; Diefendorf et al., 2010; Garcin et al., 2014). It will be shown that the $\delta^{13}C_{wax}$ record from ODP Site 659 is in a reasonable range relative to the vegetation of West Africa, but rather sensitive to contributions from different source regions with contrasting biomes dominated by either C_3 or C_4 plants. As such, the $\delta^{13}C_{wax}$ variability in the paleoclimatic context (Chapter III and IV) is primarily a qualitative proxy of "wind strength" (NETW), which is also discussed in the calibration study (Chapter V).

2.2.7 Plant-wax δD as hydrologic proxy

The stable hydrogen isotopic composition of plant waxes (δD_{wax}) offers a valuable tool to assess past precipitation variability (Schefuß et al., 2005, 2011; Pagani et al., 2006; Huang et al., 2007; Tierney et al., 2010, 2011; Tipple and Pagani, 2010; Collins et al., 2013, 2014; Magill et al., 2013b; Niedermeyer et al., 2010, 2014). However, several factors may contribute to the final δD_{wax} signature. A growing number of studies thus focuses on the linkages between δD_{wax} and climatic conditions by analyzing living plants, soils, aerosols, lake and marine surface sediments from different environmental settings (Sternberg, 1988; Sessions et al., 1999; Chikaraishi and Naraoka, 2003; Sachse et al., 2004, 2006, 2009; Liu et al., 2006; Smith and Freeman, 2006; Pedentchouk et al., 2008; Aichner et al., 2010; Feakins and Sessions, 2010a,b; Polissar and Freeman, 2010; Garcin et al., 2012; Leider et al., 2013; Shanahan et al., 2013; Gao et al., 2014).

The most important influence on δD_{wax} is the stable hydrogen isotopic composition of precipitation (δD_p), while the apparent fractionation (ε) between δD_{wax} and δD_p can be affected by additional factors (see review by Sachse et al., 2012). In this way, distinct ε variations have been identified for different plant types (e.g., Chikaraishi and Naraoka, 2003;

Feakins and Sessions, 2010a,b; McInerney et al., 2011; Smith and Freeman, 2006; Sachse et al., 2006, 2009; Tipple et al., 2013), indicating that grasses utilizing the C_4-type photosynthesis are more D-depleted (mean of −136‰ for the *n*-C_{31} alkane) relative to C_3 trees (−110‰), while being more D-enriched compared to C_3 grasses (−151‰; Sachse et al., 2012). Another classification is based on plant life-forms, with shrubs (especially long-lived ones and shrub-like trees) having the least negative ε, followed by trees, forbs and grasses (Sachse et al., 2012). Climatic factors (e.g., relative humidity) may cause evaporative D-enrichment of soil-water (Smith and Freeman, 2006; McInerney et al., 2011) and leaf-water (Kahmen et al., 2013a,b). Differences in rooting depth are also important in this context, since this leads to water uptake from different groundwater levels with varying degrees of evaporative alteration (Sachse et al., 2012). Some plants, such as woody shrubs and trees, are able to increase their rooting depth, depending on water availability, while herbaceous plants are mainly limited to the upper 20 cm of the soil (Asbjornsen et al., 2008). It has been found that a larger ε in grasses (monocots) is mainly caused by physiological/biosynthetic variations, in contrast to other classes (dicots such as trees, shrubs, herbs), which are more sensitive to climatic perturbations triggering soil/leaf water D-enrichment. Furthermore, it is necessary to consider that clear differences in the timing of wax formation exist between monocots and dicots, thus integrating different δD_p ranges (Sachse et al., 2012). In contrast to deciduous leaf waxes, which are synthesized rather early during the growing season (Tipple et al., 2013), continuous wax formation in grasses provides a high potential for integrating environmental conditions of the entire growth phase (Smith and Freeman, 2006; Gao et al., 2012). Overall, this means that the δD_{wax} signature incorporates a combination of biosynthetic fractionation, source-water δD and the local environmental conditions.

2.3 Outline

The main part of this thesis comprises three manuscripts, which are either published in, submitted to or in preparation for peer-reviewed scientific journals. A brief outlook is presented in the following.

Chapter III - NW African hydrology and vegetation during the Last Glacial cycle reflected in plant-wax-specific hydrogen and carbon isotopes

Rony R. Kuechler, Enno Schefuß, Britta Beckmann, Lydie Dupont and Gerold Wefer

Published in Quaternary Science Reviews

This study presents orbitally resolved, marine records of tropical hydrology (δD_{wax}) and vegetation ($\delta^{13}C_{wax}$) changes from offshore West Africa (ODP Site 659) covering the Last Glacial cycle (last 130 ka). Elemental ratios (Al/Si, Ti/Ca), obtained by XRF scanning, are used as indicators for weathering and aeolian transport and for fine-tuning

of the age model. Alkenone-based SST estimates provide further insights into the linkages between oceanographic changes and the hydrologic regime. The importance of varying NETW strength for the interpretation of the plant-wax isotopic records is highlighted, as is the relevance of different forcing mechanisms of the West African monsoon (local summer insolation vs. SST). These data sets form the baseline for the evaluation of Pliocene climate changes (Chaper IV) related to either proxy application and forcing interpretation.

Chapter IV - Hybrid insolation forcing of Pliocene monsoon dynamics

Rony R. Kuechler, Lydie Dupont, Gerold Wefer and Enno Schefuß

Submitted to Geology

Here, the orbital-scale approach of the previous study is extended to early and middle Pliocene time intervals (5.0-4.6 Ma, 3.6-3.0 Ma), in order to investigate the impact of the CAS closure on West African monsoon variability and associated vegetation changes. The δD_{wax} and $\delta^{13}C_{wax}$ records are discussed in light of the previous results from the Last Glacial cycle, as well as available dust and pollen records. The data sets provide a new view on tropical monsoon variability on geological timescales, leading to the dynamic concept termed hybrid insolation forcing. This monsoonal forcing concept explains the shifting influences of precession and obliquity cycles identified in the δD_{wax} and dust records by accounting for the influence of latitudinal insolation gradients, in addition to the conventional summer insolation forcing.

Chapter V - Tracking the meridional hydrologic gradient across West Africa by plant-wax-specifc hydrogen and carbon isotopes in marine surface sediments

Rony R. Kuechler, Eva M. Niedermeyer, Britta Beckmann, Lydie M. Dupont, Matthias Prange, Gerold Wefer and Enno Schefuß

In preparation for Geochimica et Cosmochimica Acta

This study aims at strengthening our knowledge on the (paleo)environmental significance of the δD_{wax} signature by investigating the link between δD_{wax} in marine surface sediments and continental precipitation (δD_p) across a transect between Morocco and the Gulf of Guinea (31-9°N) spanning a large climatic gradient. Additional $\delta^{13}C_{wax}$ analyses were performed to assign the marine sedimentary hydrologic signal (δD_{wax}) to continental sources. These data sets are then compared with previously published plant-wax, pollen and climatic data from this area to discuss the influences on the final δD_{wax} signature. The study underscores the feasibility of (paleo) hydrologic reconstructions in West Africa based on marine sedimentary δD_{wax} and introduces a new proxy for climate and vegetation shifts, derived from the isotopic offsets between single long-chain *n*-alkanes.

III

NW African hydrology and vegetation during the Last Glacial cycle reflected in plant-wax-specific hydrogen and carbon isotopes

Rony R. Kuechler, Enno Schefuß, Britta Beckmann, Lydie Dupont and Gerold Wefer

MARUM – Center for Marine Environmental Sciences, University of Bremen, 28359 Bremen, Germany

Keywords: NW Africa; hydrology; vegetation; marine sediments; plant leaf waxes; isotopes; major element ratios; sea surface temperatures

Published in *Quaternary Science Reviews*

Citation: Kuechler, R.R., Schefuß, E., Beckmann, B., Dupont, L., Wefer, G., 2013. NW African hydrology and vegetation during the Last Glacial cycle reflected in plant-wax-specific hydrogen and carbon isotopes. *Quat. Sci. Rev.* **82**, 56–67.

3.1 Abstract

We present a hydrologic reconstruction of the Sahara-Sahel transition, covering the complete Last Glacial cycle (130 ka), based on a combination of plant-wax-specific hydrogen (δD) and carbon isotopes ($\delta^{13}C$). The δD and $\delta^{13}C$ signatures of long-chain *n*-alkanes from ODP Site 659 off NW Africa reveal a significant anti-correlation. Complementary to published pollen data, we infer that this plant-wax signal reflects sensitive responses of the vegetation cover to precipitation changes in the Sahel region, as well as varying contributions from biomes north of the Sahara (C_3 domain) by North-East Trade Winds (NETW). During arid phases, especially the northern parts of the Sahel likely experienced crucial water stress, which resulted in a pronounced contraction of the vegetation cover, thus reducing the amount of C_4 plant waxes from the region. The increase in NETW strength during dry periods further promoted a more pronounced C_3-plant-wax signal derived from the North African C_3 plant domain. During humid periods, the C_4-dominated Sahelian environments spread northward into the Saharan realm, in association with lower NETW inputs of C_3 plant waxes. Arid-humid cycles deduced from plant-wax δD are in accordance with concomitant changes in weathering intensity reflected in varying major element distributions. Environmental shifts are generally linked to periods with large fluctuations in Northern Hemisphere summer insolation. During Marine Isotope Stages 2 and 3, when insolation variability was low, coupling of the hydrologic regime to alkenone-based estimates of NE Atlantic sea-surface temperatures becomes apparent.

3.2 Introduction

North Africa has experienced extreme environmental variations in the past. During the early and middle Holocene, the area of the modern Sahara desert was covered with extensive meadows, forests and lakes, which offered favorable conditions for modern human civilizations to thrive (Kuper and Kröpelin, 2006) and for human migrations out of Africa (Osborne et al., 2008). Orbitally-forced insolation variability is thought to be one of the major drivers of African monsoon dynamics (deMenocal et al., 2000; Gasse, 2000) that induces these climate and vegetation changes. In contrast, NW African monsoon activity during the Last Glacial was found to be decoupled from insolation forcing due to decreasing variability in solar intensities over the northern tropics and subtropics (Tjallingii et al., 2008; Weldeab et al., 2007). Another inferred forcing component of tropical and subtropical rainfall variability is the strength of the Atlantic meridional overturning circulation (AMOC), linking arid conditions in NW Africa to a weaker AMOC (Jullien et al., 2007; Mulitza et al., 2008; Tjallingii et al., 2008; Castañeda et al., 2009). Modeling studies have demonstrated that AMOC reduction via freshwater input leads to sea-surface cooling in the North Atlantic, which causes a positive anomaly in sea level pressure over North Africa and thus restricts the northward migration of the tropical rain belt (Mulitza et al., 2008). Additional non-linear feedback mechanisms influencing and accelerating shifts between dry and wet phases include changes in sea surface temperatures (SST), vegetation cover and atmospheric teleconnections (Claussen et al., 1999; Schefuß et al., 2003b; Weldeab et al., 2007).

Previous studies have focused, for instance, on plant-wax stable carbon isotopic composition ($\delta^{13}C$) and/or pollen assemblages to reconstruct hydrologic changes at the Sahara-Sahel transition (Dupont, 1993; Zhao et al., 2003; Castañeda et al., 2009). Sedimentary plant-wax $\delta^{13}C$ records are primarily controlled by relative contributions of plants with different preferences for more humid (C_3 type) and more arid (C_4 type) conditions (e.g., Huang et al., 2000). Thus, a hydrologic assessment of a certain catchment area, based on vegetation changes reflected in plant-wax $\delta^{13}C$, is usually achieved as implication. In contrast, the stable hydrogen isotopic composition (δD) of plant waxes provides a more direct view on past continental hydrology, due to its closer link to the water source that is utilized by plants (Sachse et al., 2012 and references therein). Recent studies on African paleoenvironments have proven the interpretive strength of combined plant-wax-specific hydrogen and carbon isotopes, in both marine and lacustrine sediments, to decipher substantial shifts in hydrology (via δD) and vegetation (via $\delta^{13}C$) (Schefuß et al., 2005, 2011; Tierney et al., 2008; Niedermeyer et al., 2010; Berke et al., 2012; Magill et al., 2013a,b). However, the isotopic records off NW Africa are still scarce and the sole continuous plant-wax δD record so far spans the time interval of the past 44 ka and seems to reflect Intra-Sahelian climate and vegetation variability (Niedermeyer et al., 2010). Therefore, we investigated the abundance of plant-wax lipids and their isotopic composition (δD, $\delta^{13}C$) in a marine sediment core from the

deep-sea Cape Verde Plateau off Mauritania, spanning the Last Glacial cycle (i.e., 130 ka). As the temporal resolution (~3 ka sample spacing) does not resolve millennial-scale climatic events, we limit our investigation to the evaluation of general changes in NW African hydrology and vegetation. For this, a comparison is made with similar data sets from NW Africa to capture the spacial and temporal pattern of environmental changes. In order to assess the underlying forcing mechanisms, the plant-wax-specific biomarker and isotope records are compared with (1) alkenone-based SST estimates generated from the same sample material, (2) deep water circulation changes indicated by the $\delta^{13}C$ signature of benthic foraminifera (Sarnthein and Tiedemann, 1989), (3) major element ratios (terrigenous vs. marine sediment input, continental weathering intensity) in high resolution obtained by X-ray fluorescence scanning, (4) the dust (= carbonate-free sediment) record (Tiedemann et al., 1994) and (5) variations in solar insolation (Berger, 1978).

3.3 Environmental setting

The seasonal N-S-migration of the tropical rain belt exerts the most crucial impact on NW-African climate (Feakins and deMenocal, 2010). These latitudinal shifts are caused by changes in annual solar insolation, leading to a principal decrease in precipitation amounts from the equator towards higher latitudes (Nicholson, 2009). Precipitation in the West African Sahel is mainly sourced by moisture from the Gulf of Guinea with further contributions from continental evapotranspiration (Gong and Eltahir, 1996; Nicholson, 2009). The rainy season covering approximately 80% of the annual precipitation amount occurs typically during boreal summer (July to September) when the tropical rain belt reaches its northernmost position at ~20°N (Nicholson, 2009). Consequently, dry conditions prevail over most of the year and are related to a southward migration of the rain belt to ~10°N during boreal winter. In contrast, areas north of the Sahara are under the influence of winter rainfall (Nicholson, 2000). Abnormally intense rainfall events during the winter season can even extend from their Mediterranean origin to 10°N and account for most of the major rainfall events in the central Sahara (Nicholson, 2000).

The availability of water strongly determines the distribution and composition of the vegetation, and is reflected in the large-scale transition from the Guinean rain forest dominated by C_3 plants to the Sahara desert with a sparse vegetation of mostly C_4 plants and negligible occurrences of CAM plants (White, 1983). Among the NW African biomes, the C_4-dominated savannas of the Sahel constitute the transition zone towards the desert (White, 1983) and as such it is most susceptible to climate variability, reflected in catastrophic droughts reported in the recent past (1909-13, 1940-44, 1969-73, 1983-85; Heinrigs and Perret, 2009), but also in large latitudinal migrations of up to 9° during glacial-interglacial cycles (Dupont, 1993).

During boreal winter, the atmospheric circulation over NW Africa is governed by low-altitude North-East Trade Winds (NETW), which supply most of the terrigenous material to the adjacent NE Atlantic (e.g., Chiapello et al., 1995). At higher altitudes, the African Easterly Jet (AEJ) is strongest in boreal summer, carrying dust from the southern Sahara and Sahel westward (Pye, 1987). These two wind systems are also responsible for the export of plant waxes to the ocean (Huang et al., 2000). In the NE Atlantic off NW Africa, however, dust deposition is dominated by the NETW, compared to the long distance transport by the AEJ (Chiapello et al., 1995, 1997; Stuut et al., 2005). The terrigenous fraction in marine sediments off NW Africa seems to be mostly derived from major dust outbreaks, which was inferred from similar Sr-Nd isotopic compositions in dust and sediments (Skonieczny et al., 2011). In addition, an obvious shift from northwestern to southeastern source regions was apparent during one single storm event in March 2006, integrating signals from a large catchment area (Mauritania, Mali, S Algeria, N Niger; Skonieczny et al., 2011). Interestingly, recent dust outbreaks from the Sahel seem to supply most of the terrigenous material to the NE Atlantic, but occur only during December and January (Chiapello et al., 1997). This also implies that the export of most plant waxes is restricted to the winter season. Though the timing of wax formation is not uniform in all plants (see discussion in section 5.3), we may assume that plant waxes are generally produced during the growing/summer season (Sachse et al., 2012), and therefore incorporate the corresponding environmental signal, which is then preserved in marine sediments.

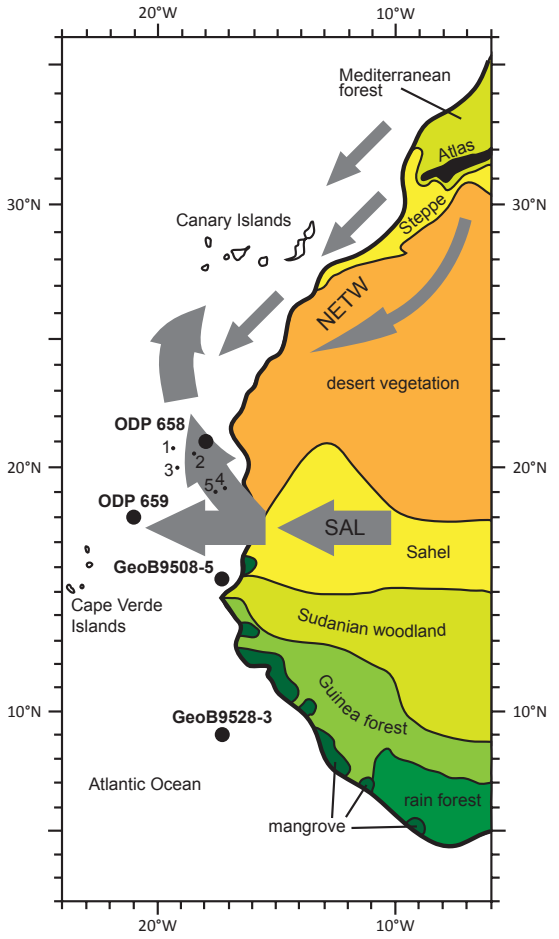

Fig. 3.1: Today's vegetation belts and wind systems of NW Africa and locations of cores (black circles) discussed in the text, including the positions of coretops used as modern analog, (1) GeoB7919-2, (2) GeoB7922-3, (3) GeoB7927-1, (4) GeoB7928-3, (5) GeoB7932-2 (see also **Table 3.1**). Dominant wind systems are indicated by arrows, Saharan Air Layer (SAL), North-East Trade Winds (NETW). The thickness of the arrows marks the different altitudes of the SAL (> 3000 m) and the NETW (< 1000 m) (modified after Hooghiemstra et al., 2006).

3.4 Materials and methods

3.4.1 Core specifications and sampling

Ocean Drilling Program (ODP) Site 659 (18°05‘N, 21°02‘W) is located on the submarine Cape Verde Plateau in 3070 m water depth (**Fig. 3.1**). Sediments consist mainly of pelagic foraminifer-nannofossil ooze with varying contributions of silt and clay (Faugères et al., 1989). The latter is considered to be of purely eolian origin due to (1) insignificant carbonate concentrations in the terrigenous dust composition, and (2) its distal position on a submarine rise excluding fluvial input and influences of turbidites (Tiedemann et al., 1989, 1994).

The original age model of ODP 659 for the last 130 ka (Sarnthein and Tiedemann, 1989; Tiedemann et al., 1994) has an average temporal resolution of 5 ka and is based on the correlation of foraminiferal stable oxygen isotopes ($\delta^{18}O$) to the benthic isotope record of the Pacific ODP Site 677 (Shackleton et al., 1990). Because there is evidence that Atlantic and Pacific $\delta^{18}O$ records do not vary synchronously, a stratigraphic correlation between the two holds the potential for large chronological uncertainties of several thousand years, most apparent during deglaciations (Skinner and Shackleton, 2005, 2006; Lisiecki and Raymo, 2009). For this reason, the ODP 659 stratigraphy was fine-tuned by visual peak-to-peak correlation of the titanium-calcium ratio (Ti/Ca), obtained from X-ray fluorescence scanning (section 3.4), to the same element ratio from the nearby core MD03-2705 (18°05’N; 21°09’W; Jullien et al., 2007; **Fig. 3.2**). Its better resolved age model includes eight AMS-^{14}C ages over the last 36 ka, dated on planktonic foraminifera *Globigerina bulloides* (> 150 µm). ^{14}C dates were corrected by accounting for a reservoir age of 500 years (deMenocal et al., 2000) and subsequently calibrated to calendar ages (Bard, 1988; Stuiver et al., 2005). Additional age control points are based on microfaunal and isotopic events (for a complete compilation see Fig. 2 and Table 1 from Matsuzaki et al., 2011). While chronological uncertainties were minimized for the last deglaciation by radiocarbon dating, they largely remain unchanged for the oldest part of the record, with a potential deviation of ~4 ka at about 128 ka (Lisiecki and Raymo, 2009).

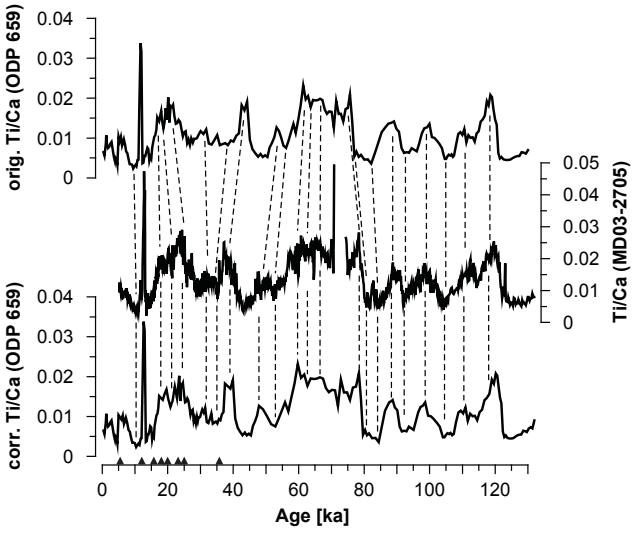

Fig. 3.2*:* Stratigraphic fine-tuning by visual peak-to-peak correlation of Ti/Ca ratios of ODP 659 (this study) and MD03-2705 (Jullien et al., 2007). AMS-^{14}C ages of core MD03-2705 are indicated on bottom (black triangles). Upper ODP 659 curve plotted against the original (orig.) time scale (Tiedemann et al., 1994); lower ODP 659 curve plotted against the corrected (corr.) time scale.

In total, 43 samples were collected from the upper 4.3 m of ODP core 108-659B-1H, covering the past 130 ka, with an average temporal resolution of ~3 ka, similar to the dust [%] record (Tiedemann et al., 1994). Additionally, five coretop samples serve as modern analog in marine surface sediments (**Table 3.1**).

3.4.2 Lipid extraction and analyses

All samples were dried, ground and an internal standard (IS; squalane) was added before extraction. Lipid extraction was performed with a DIONEX Accelerated Solvent Extractor (ASE 200) using a mixture of dichloromethane:methanol (DCM:MeOH, 9:1) under controlled pressure (1,000 psi) and temperature (100°C). The resultant total lipid extracts were concentrated via rotary evaporation and subsequently saponified with 6% KOH in MeOH at 85°C for 2 h. Neutral compounds were then isolated with hexane and separated by column chromatography with silica gel (60 mesh). Further column chromatography with $AgNO_3$-coated silica gel was used to purify the saturated hydrocarbons by removing all unsaturated compounds. Due to very low alkenone concentrations, ketones and polar compounds were obtained in a single fraction by elution with DCM:MeOH (1:1) to avoid potential loss during column chromatography.

Identification and quantification of *n*-alkanes and alkenones was carried out by gas chromatography/flame ionization detection (GC-FID) using a reference mixture with known *n*-alkane concentrations as external standard. Calculation of the $U^{k'}_{37}$ index based on the di- and triunsaturated C_{37} alkenones was performed according to Prahl and Wakeham (1987), with $U^{k'}_{37}$ = [37:2]/[37:2 + 37:3]. Based on this, SST estimates were obtained from the global coretop calibration after Müller et al. (1998) with SST (°C) = ($U^{k'}_{37}$ − 0.044)/0.033.

3.4.3 Plant-wax-specific stable hydrogen and carbon isotopes

Compound-specific δD analyses were accomplished using a Thermo Trace GC coupled to a Thermo Fisher Scientific MAT 253 irm-MS via a pyrolysis furnace operated at 1,430°C. All measurements are calibrated against H_2 reference gas with known isotopic composition and the H^{3+} factor was monitored daily (values between 6.7 and 6.8). All δD values are reported in permil [‰] relative to the VSMOW standard. An external standard mixture with known δD values of *n*-alkanes was analyzed repeatedly with the samples, and yielded a standard deviation (1σ) of 2‰. In addition, squalane (IS) yielded a standard deviation (1σ) of 2.9‰. It was not possible to perform replicate analyses on all samples due to low concentrations (3 samples). The mean standard deviation (1σ) of replicates for the *n*-C_{31} alkane is 1‰.

The $\delta^{13}C$ values of *n*-alkanes were measured using a Thermo Trace GC coupled to a Finnigan MAT 252 irm-MS via a modified Finnigan GC/C III combustion interface operated at 1,000°C. The $\delta^{13}C$ values were calibrated against an external reference gas (CO_2) with known isotopic composition. $\delta^{13}C$ values are reported in the delta notation relative to the

VPDB standard. Duplicate measurements yielded a standard deviation (1σ) for the *n*-C_{31} alkane of 0.2‰ and for squalane of 0.3‰.

The same analyses were carried out on five coretop samples (**Table 3.1**) from the NW African margin. Data were averaged to obtain an estimate for the recent sedimentary plant-wax signal in marine surface sediments for comparison with the ODP 659 record. The mean standard deviation of δD and $\delta^{13}C$ values for the *n*-C_{31} alkane of surface samples is 1.4‰ and 0.2‰, respectively. For squalane (IS), the corresponding values are 2‰ and 0.1‰, respectively.

3.4.4 X-ray fluorescence (XRF) core scanning

Element data were collected in 2-cm-intervals down-core over a 1 cm^2 area with slit size of 10 mm using generator settings of 10 kV, a current of 0.25 mA, and a sampling time of 20 s directly at the split core surface of the archive half with XRF Core Scanner II at the MARUM - University of Bremen. The split core surface was covered with a 4 µm thin SPEXCerti Prep Ultralene1 foil to avoid contamination of the XRF measurement unit and desiccation of the sediment. The data have been acquired by a Canberra X-PIPS Silicon Drift Detector (SDD; Model SXD 15C-150-500) with 150eV X-ray resolution, the Canberra Digital Spectrum Analyzer DAS 1000, and an Oxford Instruments 50W XTF5011 X-Ray tube with rhodium (Rh) target material. Raw data spectra were processed by the analysis of X-ray spectra by Iterative Least square software (WIN AXIL) package from Canberra Eurisys. Reliable, i.e., sufficient, elemental counts were achieved for the following elements: Al, Si, K, Ca, Ti, and Fe.

3.5 Results

Sedimentary concentrations of *n*-alkanes are dominated by long-chain *n*-$C_{25\text{-}35}$ homologues, ranging from 0.08 to 1.84 (average 0.46) µg g^{-1} dry weight (**Fig. 3.3**) and carry typical plant wax signatures with carbon preference-indices (CPI) between 2.2 and 7.1 (average 4.9). Most samples (88%) exhibit *n*-alkane concentrations of 0.2 to 0.8 µg g^{-1} dry weight. Comparable values were obtained from the coretops with average *n*-alkane concentrations of 0.59 µg g^{-1} dry weight and an average CPI of 3.5. The isotope records obtained from the *n*-C_{29}, *n*-C_{31} and *n*-C_{33} alkanes correlate strongly (correlation coefficients $r_{29/31}$ of 0.80 and $r_{31/33}$ of 0.74 and $r_{29/33}$ of 0.73 for δD, and $r_{29/31}$ of 0.86 and $r_{31/33}$ of 0.78 and $r_{29/33}$ of 0.62 for $\delta^{13}C$). For further discussion we focus on the *n*-C_{31} alkane as the most abundant homologue in all samples.

The δD record of the *n*-C_{31} alkane (δD_{C31}) is corrected for changes in ice volume fluctuations throughout the Last Glacial cycle (Schrag et al., 2002). This correction is based on the sea level record of Waelbroeck et al. (2002) with the highest shift of about -8.3‰

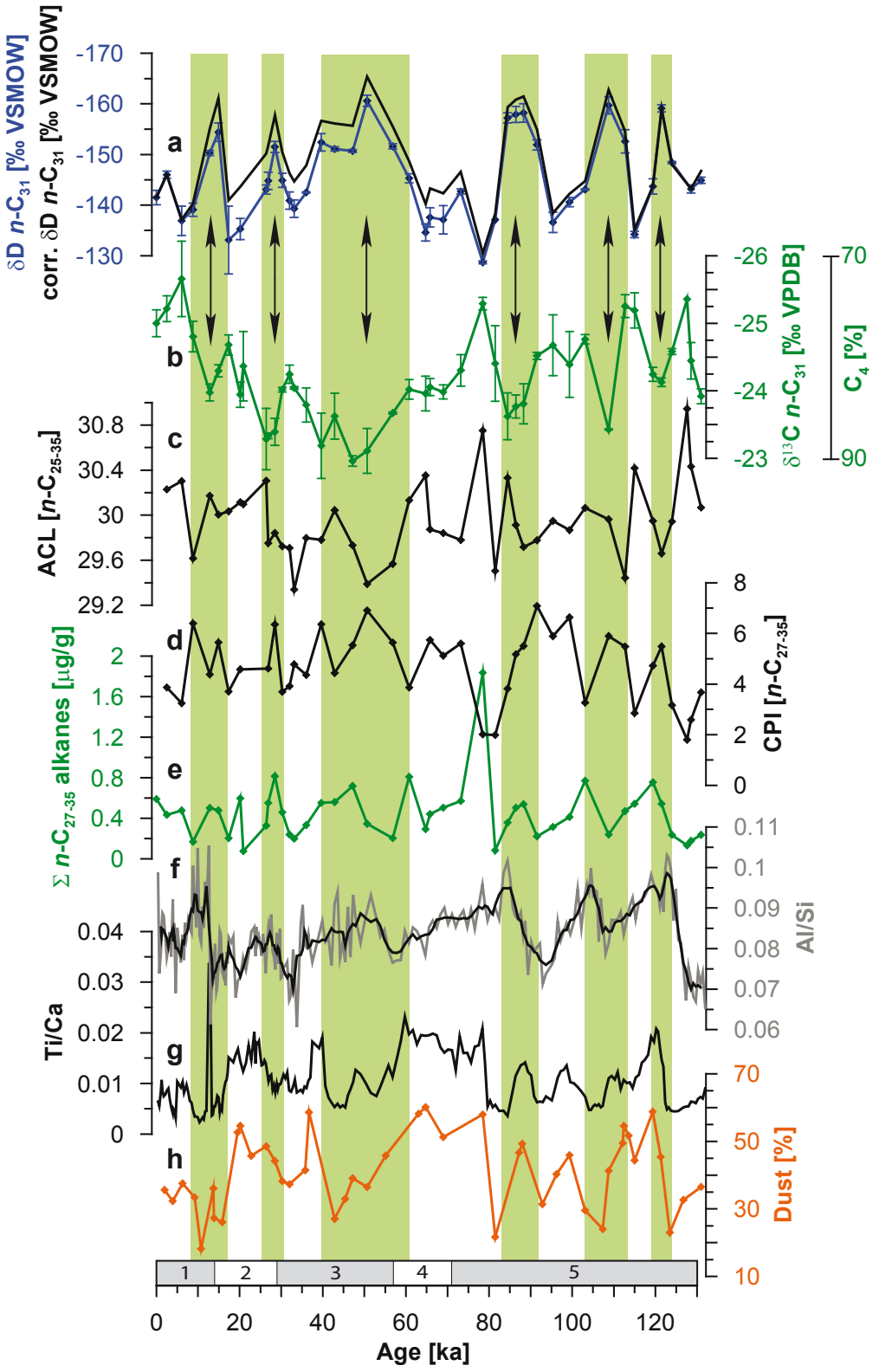

Fig. 3.3*:* Compilation of results from ODP 659: (a) original (blue) and ice-volume-corrected δD (black) and (b) $\delta^{13}C$ values of the *n*-C_{31} alkane and corresponding C_4 [%] estimates (see section 3.6.2); (c) average chain-length (ACL) of long-chain *n*-alkanes (C_{25-35}); (d) carbon preference index (CPI) of long-chain *n*-alkanes (C_{25-35}); (e) long-chain *n*-alkane (C_{25-35}) concentrations (per g dry sediment); (f) Al/Si ratio with 5-point running mean (black curve) indicating higher weathering intensity with increasing values; (g) Ti/Ca ratio (terrigenous vs. marine input); (h) dust [%] record (Tiedemann et al., 1994). Modern values ("0 ka") of plant-wax data are calculated from the averaged results of the coretops. Marine Isotope Stages (MIS) are indicated on bottom. Error bars indicate the standard deviation of multiple measurements. Green bars highlight humid periods reflected in the δD_{C31} signature.

VSMOW corresponding to the Last Glacial Maximum (LGM; 18-23 ka). Overall, δD_{C31} values range between −165.4‰ and −130.5‰ (uncorrected −160.6‰ and −128.7‰) and $\delta^{13}C$ values of the *n*-C_{31} alkane ($\delta^{13}C_{C31}$) vary between −25.7‰ and −23‰ (**Fig. 3.3**). The coretop samples yield $\delta^{13}C_{C31}$ values between −25.7‰ and −24.5‰, with an average of −25‰ and δD_{C31} values between −142.8‰ and −140.6‰, with an average of −141.5‰ (**Table 3.1**). We use these mean values as analogs for the present-day plant-wax signal in marine surface sediments.

The $U^{k'}_{37}$-derived SST record of ODP 659 shows the typical decrease towards the LGM, with values between 18.6 and 29°C ($U^{k'}_{37}$ values between 0.66 and 1) and an average standard deviation for duplicate measurements of 0.28°C (0.01 for $U^{k'}_{37}$ values; **Fig. 3.5**). SST values of the coretops range between 22 and 27.5°C ($U^{k'}_{37}$ values between 0.77 and 0.95) with an average SST of 25.3°C ($U^{k'}_{37}$ value of 0.88; **Table 3.1**).

To achieve a more comprehensive interpretation, we additionally measured the elemental distribution throughout the investigated time interval. Because carbonate is almost absent in Saharan dust (Tiedemann et al., 1989 and references therein), we focused on the titanium-calcium ratio (Ti/Ca) as a proxy for terrigenous input, comparable to the Al content (not shown) (e.g., Prospero, 1996). The aluminum-silicon ratio (Al/Si) is used as proxy for (chemical) weathering intensity (Mulitza et al., 2008). We found good agreement between our and previously published records. The Ti/Ca ratio and Al content (XRF-counts) consistently parallels the dust [%] record of ODP 659 (Tiedemann et al., 1994) and is also clearly reflected in the XRF data of the neighboring core MD03-2705 (Jullien et al., 2007). In addition, highest Al/Si ratios are found during dust minima (**Fig. 3.3**).

Table 3.1: Compilation of coretop data used as modern analog in marine surface sediments. Numbers (No.) refer to core locations in **Fig. 3.1**. SD, standard deviation (1σ).

No.	Coretops	Latitude	Longitude	Depth (m)	*n*-C_{27-35} [µg/g]	$\delta^{13}C_{C31}$	SD	C_4%	δD_{C31}	SD
1	**GeoB7919-2**	20.942°N	19.387°W	3429	2.42	-25.74	0.45	70.10	-142.32	0.69
2	**GeoB7922-3**	20.667°N	18.262°W	1289	2.58	-24.98	0.17	75.71	-140.59	2.56
3	**GeoB7927-1**	19.937°N	19.152°W	3128	5.42	-25.04	0.02	75.24	-140.77	1.88
4	**GeoB7928-3**	19.100°N	17.047°W	1348	4.47	-24.54	0.04	78.97	-140.95	0.92
5	**GeoB7932-2**	19.002°N	17.283°W	1964	2.27	-24.55	0.11	78.89	-142.80	0.85
	Mean					**-25.00**	**0.20**	**75.78**	**-141.50**	**1.40**

Table 3.2: Reference data of cores discussed in the text.

Core	Position	Depth	Time interval	Proxies	Signal	Reference
ODP 658	20°45'N, 18°35'W	2263 m	0.8 – 154 ka	$\delta^{13}C_{wax}$, pollen	more humid = more C_4 plants	Zhao et al., 2003
ODP 659	18°05'N, 21°02'W	3070 m	2.5 – 131 ka	$\delta^{13}C_{wax}$, δD_{wax}	more humid = more C_4 plants	this study
GeoB9508-5	15°30'N, 17°57'W	2384 m	1.4 – 43.6 ka	$\delta^{13}C_{wax}$, δD_{wax}	more humid = more C_3 plants	Niedermeyer et al., 2010
GeoB9528-3	09°10'N, 17°40'W	3057 m	6.9 – 192 ka	$\delta^{13}C_{wax}$	more humid = more C_3 plants	Castañeda et al., 2009

3.6 Discussion

3.6.1 n-Alkane distribution patterns

n-Alkanes are a major constituent of leaf waxes of terrestrial higher plants, which are produced to minimize transpiration and to protect the leaves against physical and biological stress (Eglinton and Hamilton, 1967). Wax compounds can be effectively removed from leaves by eolian dust (Simoneit et al., 1977), but also after the decay of plants and subsequent burial and/or transport via winds or rivers, they remain relatively resistant against degradation (Eglinton and Eglinton, 2008). Plants typically produce long-chain *n*-alkanes in the range of *n*-C_{25} to *n*-C_{35} with a characteristic odd-over-even carbon number predominance (Chibnall et al., 1934; Eglinton and Hamilton, 1967). This is numerically given in the carbon preference index (CPI) with conventionally higher (>3) values for plant-wax-derived *n*-alkanes (Bray and Evans, 1961; Eglinton and Hamilton, 1963; Mazurek and Simoneit, 1984). Significantly lower CPI values (~1) may point to other carbon sources like petroleum (Bray and Evans, 1961; Simoneit, 1984), but have also been assigned to thermal degradation via biomass burning/wildfires (Standley and Simoneit, 1987), microbial degradation of plant litter (Vogts et al., 2012), or even marine sources (Lichtfouse et al., 1994). CPI values from ODP 659 (average 4.9) thus reflect major contributions by terrestrial higher plants (**Fig. 3.3**). A recent survey of plant-wax data by Bush and McInerney (2013) has demonstrated a wide CPI range among various plant types, which suggests discarding the use of CPI as a strict source or degradation indicator. Nevertheless, studies on recent African dust revealed the lowest *n*-alkane CPI values occurring off NW Africa (Eglinton et al., 2002; Schefuß et al., 2003a). This is explained by low concentrations of leaf-wax lipids in aerosols from arid regions being highly sensitive to admixture of fossil fuel or marine lipids. Despite such contributions, the isotopic composition of major (odd-numbered) homologues remained unaffected (Eglinton et al., 2002; Schefuß et al., 2003a).

Maxima in *n*-alkane concentrations are generally coupled to dust pulses, emphasizing the role of eolian transport for plant wax deposition at ODP Site 659 (**Fig. 3.3**). This observation is in accordance with the model of dust/plant-wax export during aridification events (Trauth et al., 2009). For instance, the African Humid Period (AHP; 14.8 – 5.5 ka BP) was the last wet interval in the Saharan realm (deMenocal et al., 2000). The underlying monsoon displacement, caused by variations in solar insolation and additional vegetation-albedo feedbacks (Gasse, 2000), also involves the wind systems responsible for moisture (SW monsoon) and dust (NETW, AEJ) transport (Nicholson, 2009). It is argued that erosional processes like desiccation and deflation of lacustrine and fluvial sediments of a former wet Sahara/Sahel lead to high dust production (Trauth et al., 2009). This interpretation can be transferred to the whole investigated time interval, since insolation-driven changes in dust accumulation at ODP Site 659 are evident (Tiedemann et al., 1989, 1994). Accordingly, admixture of reworked, older plant material should be considered, as this may bias the climate

signal of a given region and time. It can be expected that such contributions are highest during aridifications and the subsequent dry periods like today, when desiccated lake beds and soils serve as dust source (Heinrigs and Perret, 2009). There is evidence that the vegetation-derived fraction in NW African aerosols is not exclusively recent. Radiocarbon dating of *n*-alkanols, another prominent class of plant-wax compounds, in dust collected by a buoy, yielded a ^{14}C-age of 647 ±150 years (Eglinton et al., 2002). However, because of the low resolution of the ODP 659 plant-wax records (~3 ka), the reported age offsets are only of minor consequences for our climate reconstructions. It is thus assumed that contributions from ancient sedimentary and pedogenic sources are efficiently superimposed by the prevailing contributions from vegetation and organic matter of contemporary soils (Simoneit et al., 1988; Simoneit, 1997; Schefuß et al., 2003a).

3.6.2 Vegetation types

The stable carbon isotopic composition of plants is mainly determined by two principal photosynthetic pathways of carbon fixation. Plants using the C_3 pathway are considerably more ^{13}C-depleted relative to those utilizing the C_4 type, which is true for the whole leaf tissue and also on a molecular level for their epicuticular wax coating (Collister et al., 1994). The $\delta^{13}C$ values of long-chain *n*-alkanes in leaf waxes range from −32‰ to −39‰ in C_3 plants and −18‰ to −25‰ in C_4 plants (Rieley et al., 1991, 1993; Collister et al., 1994; Rommerskirchen et al., 2006a; Vogts et al., 2009). Changes in the isotopic composition of atmospheric CO_2 are negligible (Indermühle et al., 1999). Thus, $\delta^{13}C_{C31}$ values can be used to estimate C_3 and C_4 plant contributions (%) to the sedimentary *n*-alkane record. For this, we applied a binary mixing model with isotopic end-members for C_3 and C_4 plants derived from a data compilation by Castañeda et al. (2009) with averaged $\delta^{13}C_{C31}$ values of −35.2‰ and −21.7‰ for C_3 and C_4 plants, respectively. We are aware of the large ranges in this data set, leading to an uncertainty in C_3/C_4 estimates of about ±20%. This uncertainty is even twice as high (about ±45%) when considering a global survey of published leaf $\delta^{13}C$ values of woody C_3 plants (Diefendorf et al., 2010). Findings like these challenge the applicability of C_3/C_4 estimates based on plant-wax $\delta^{13}C$ and is thus rather avoided at present. In the same way, using globally averaged $\delta^{13}C$ end-members for C_3 and C_4 plants in regional-scale studies is also disputable. Nevertheless, relative changes in plant-wax $\delta^{13}C$ should still enable a qualitative interpretation of the record.

Other approaches focus on the estimation of woody plant cover derived from the $\delta^{13}C$ signature of soil organic matter (Cerling et al., 2011), and built on this, directly from $\delta^{13}C_{C31}$ (Magill et al., 2013a). Still, this method is originally based on a relative C_3/C_4 relationship (Cerling et al., 2011 and references therein; Magill et al., 2013a). According to Magill et al. (2013a), the ODP 659 $\delta^{13}C_{C31}$ record would reflect a total woody plant variability of only 2-12%, indicating that there is almost no detectable change. Furthermore, considering the regional setting, contributions from multiple source regions are likely and thus, estimates of

woody plant cover for a specific area would be meaningless. Instead, C_3/C_4 estimates in this particular setting may be helpful to assess relative changes in the magnitude of supplied plant material from different catchments (Zhao et al., 2003), which is also evident in marine sedimentary pollen distributions (Hooghiemstra and Agwu, 1986; Hooghiemstra et al., 2006). Hence, the approach of converting $\delta^{13}C_{C31}$ values into estimates of relative C_4 contribution changes is mainly limited to its comparison to relative changes documented in the published pollen data sets.

Quantitative estimates are further complicated by different *n*-alkane amounts in plant waxes, with angiosperms (all C_4 grasses) producing considerably more *n*-alkanes than gymnosperms (Diefendorf et al., 2011; Bush and McInerney, 2013). It cannot be excluded that enriched $\delta^{13}C_{C31}$ values throughout the ODP 659 record are overrepresenting the relative C_4 contributions, but with regard to the provenance of plant waxes deposited in that area, the Sahel (predominantly C_4 plants) is most likely their source (see section 5.4). This is also supported by the averaged $\delta^{13}C$ value of the *n*-C_{29} alkane obtained from the coretops (−26.3‰) as modern analog, which is in good agreement with a compound-specific isotope map off NW Africa, yielding most enriched values in that particular area ($\delta^{13}C_{C29}$ approx. −26‰, see Fig. 3 in Huang et al., 2000). A clear predominance of C_4 plant waxes (about 70-90%) is also reflected in the $\delta^{13}C_{C31}$ records of ODP 659 (values between −25.7‰ and −23‰) and the coretops (values between −25.7‰ and −24.5‰), identifying the Sahel as the major source region.

Previous plant-wax studies off NW Africa show similar ranges of C_4 plants contributing to the marine sedimentary record (54-99% by Castañeda et al., 2009; 85-100% by Niedermeyer et al., 2010; **Fig. 3.4**). Nevertheless, these records also show opposite signals compared to our results. For instance, the results obtained from core GeoB9528-3 at 9°N show maxima in C_3 plants during Marine Isotope Stages (MIS) 3 and 5 (at 50-45 ka and 120-110 ka, respectively), attributed to expansions of the vegetation cover across the Saharan-Sahelian realm (Castañeda et al., 2009), while the ODP 659 records simultaneously exhibit C_4 maxima (**Fig. 3.4**). Similarly, the $\delta^{13}C_{C31}$ record of core GeoB9508-5 at 15°N shows highest values during the LGM and is thus more comparable to the GeoB9528-3 record in the south. These contrasting signals are most likely related to the different core locations (9°N vs. 15°N vs. 18°N), with ODP 659 being further north and thus closer to the latitude of the Sahara-Sahel-transition. A stronger monsoon activity at these latitudes favors C_4 plants to extend northward into the Sahara desert (Dupont and Hooghiemstra, 1989), whereas C_3 plants are increasingly dominating towards the equator and become even more abundant during times of enhanced precipitation. From this perspective, it becomes evident that the GeoB9528-3 $\delta^{13}C_{C31}$ record tracks the transition between Guinean forest and Sudanian woodland, while GeoB9508-5 seems to reflect either shifts of the southern Sahel boundary or Intra-Sahelian variability.

Unfortunately, sediments of ODP 659 are generally too poor in pollen for reliable palynological analysis hampering a direct comparison with our stable isotopes results.

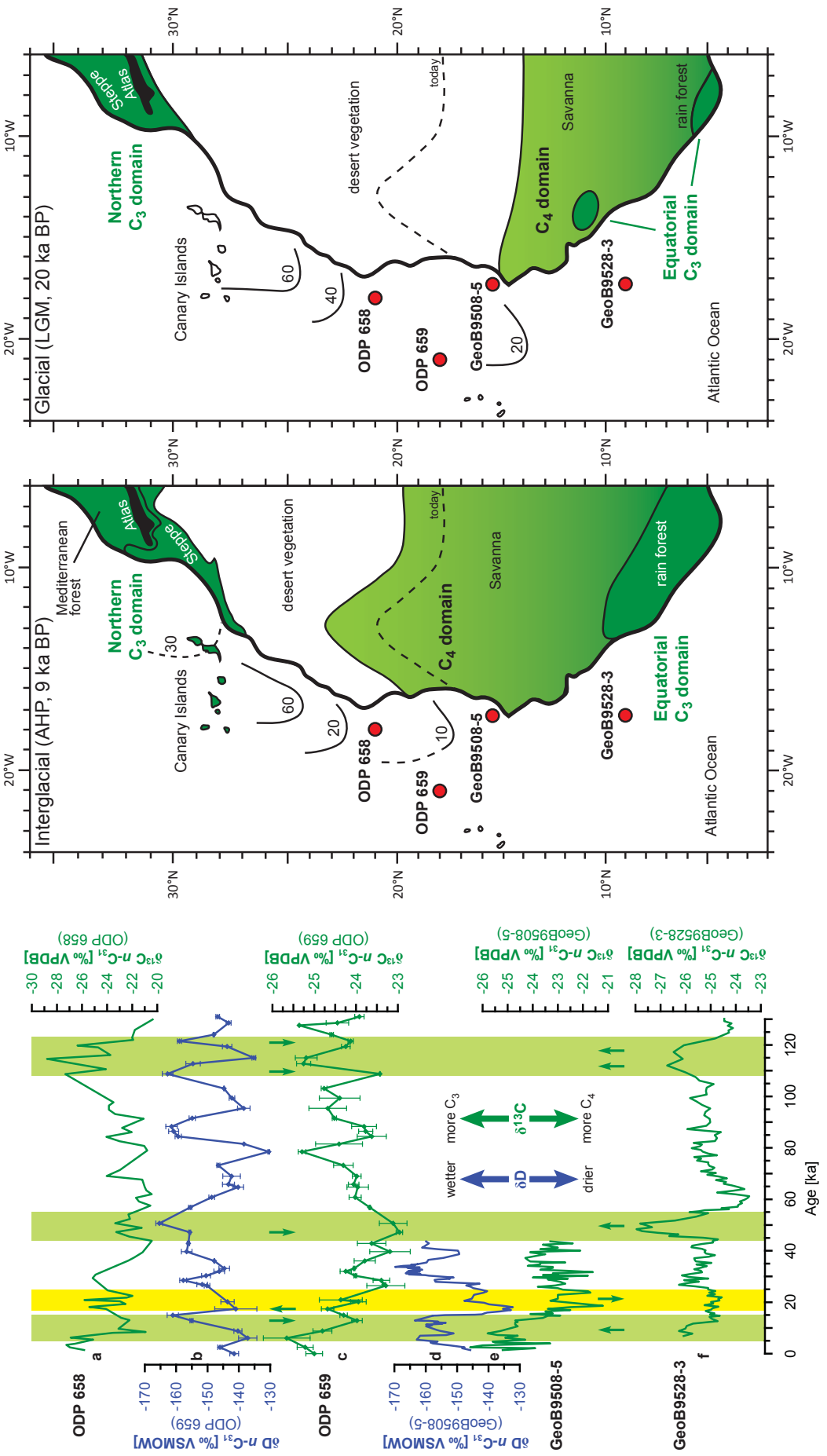
Glacial (LGM, 20 ka BP)
Interglacial (AHP, 9 ka BP)
Northern C3 domain
Equatorial C3 domain
C4 domain
Mediterranean forest
Steppe
Atlas
Canary Islands
desert vegetation
today
Savanna
rain forest
Atlantic Ocean
ODP 658
ODP 659
GeoB9508-5
GeoB9528-3
10°W
20°W
30°N
20°N
10°N
ODP 658
ODP 659
GeoB9508-5
GeoB9528-3
δD n-C31 [‰ VSMOW]
δ13C n-C31 [‰ VPDB]
(ODP 659)
(GeoB9508-5)
(ODP 658)
(GeoB9528-3)
wetter
drier
more C3
more C4
δD
δ13C
Age [ka]
0
20
40
60
80
100
120

Fig. 3.4: Comparison of plant-wax isotope records off the NW African coast (see also **Table 3.2**): (a) $\delta^{13}C_{C31}$ values from ODP 658 (Zhao et al., 2003); (b) δD_{C31} and (c) $\delta^{13}C_{C31}$ values from ODP 659 (this study); (d) δD_{C31} and (e) $\delta^{13}C_{C31}$ values from GeoB9508-5 (Niedermeyer et al., 2010); (f) $\delta^{13}C_{C31}$ values from GeoB9528-3 (Castañeda et al., 2009). For a proper comparison, all reported δ-values are derived from the *n*-C_{31} alkane. δD_{C31} records are corrected for changes in ice volume (see section 3.5). Error bars indicate the standard deviation of multiple measurements. Modern values ("0 ka") of ODP 659 records are calculated from the averaged results of the coretops (locations in **Fig. 3.1**). Vertical bars highlight humid (green) and arid (yellow) phases as discussed in the text and exemplified in the maps (right). Note the opposite carbon isotopic signals, highlighted by arrows, in the ODP cores compared to the GeoB cores to the south. Maps: Red dots indicate positions of marine sediment cores compared in this study. Glacial (Last Glacial Maximum, LGM, ca. 20 ka BP) and Interglacial (African Humid Period, AHP, ca. 9 ka BP) isopollen contours of 'NETW indicator' pollen (%) in marine sediments (Hooghiemstra et al., 2006) and corresponding vegetation distributions (Dupont, 1993).

However, pollen and plant-wax analyses on sediments of ODP 658 showed a pattern comparable to that detected for ODP 659, interpreted as the result of the northward extension of C_4 grass-rich vegetation types of the Sahel into the vegetation-poor desert during more humid periods (Dupont and Hooghiemstra, 1989; Zhao et al., 2003).

With respect to a recent study by Vogts et al. (2012), correlating the average chain-length distribution (ACL) with $\delta^{13}C_{C31}$ in SW Africa, it appears noteworthy that this positive correlation is inverted in the ODP 659 records: While $\delta^{13}C_{C31}$ values increase (indicating more C_4 plants), the ACL values decrease (**Fig. 3.3**), though C_4 plants are synthesizing longer chain lengths than C_3 plants (Rommerskirchen et al., 2006a,b; Vogts et al., 2009) and thus, ACL values would be expected to increase. The relationship ($r = -0.53$; $p < 0.01$) is best explained by a previously proposed influence of aridity on chain-length distributions (Schefuß et al., 2003a), which is also supported by the significant correlation ($r = 0.50$; $p < 0.01$) between ACL and δD_{C31}. Considering the protective function of leaf waxes to stabilize the plant's water budget (Hall and Jones, 1961), it appears likely that drier conditions favor the biosynthesis of longer-chain plant-wax compounds (Rommerskirchen et al., 2006a; Bush and McInerney, 2013).

3.6.3 Continental hydrology

The δD signature of leaf waxes is principally linked to the stable hydrogen isotopic composition of its source water, i.e., leaf and xylem water mostly derived from precipitation (Sachse et al., 2012 and references therein). In NW Africa, the high seasonality in precipitation dominates the isotopic fractionation of rain and leads to decreasing δD values with increasing precipitation intensities, expressed as the "amount effect" (Dansgaard, 1964; Worden et al., 2007; Risi et al., 2008a,b). The low seasonal temperature variability reduces the temperature effect and the general proximity to rain-generating atmospheric convection in the tropics minimizes the continental effect (Dansgaard, 1964; Rozanski et al., 1993). Furthermore, altitudinal changes in NW African topography are negligible. We assume that these conditions persisted throughout the investigated time interval. Nevertheless, a simple translation of plant-wax δD values (δD_{wax}) into absolute precipitation amounts would be a misleading simplification of the underlying mechanisms. Apart from the effect of changing ice volume in the course of the Last Glacial cycle (see Section 4.2),

substantial influences on the δD_{wax} composition may result from changes in vegetation type (e.g., photosynthetic pathway, discussed below) and evapotranspiration. The latter generally causes D-enrichment of soil- and leaf-water due to the preferential loss of water with lighter hydrogen isotopes via soil evaporation, as well as leaf transpiration (Sachse et al., 2012). D-enriched *n*-alkanes are the ultimate result of these physical and biochemical processes, as recently evidenced in a greenhouse-field-model comparison (Kahmen et al., 2013a,b). Hence, these authors conclude that the incorporated δD_{wax} signal reflects a mixture of both the state of hydrology (precipitation) and plant physiology (evapotranspiration) at the time of wax formation, mostly affecting the vegetation of arid regions. However, a substantial D-enrichment relative to the original source signal seems unlikely due to the shortness of the rainy season in the Sahara/Sahel region (Heinrigs and Perret, 2009) and the relatively fast water uptake by grasses (Smith and Freeman, 2006; Gao et al., 2012), especially under humid conditions of the growing season. In addition, formation of grass waxes is a continuous process (Smith and Freeman, 2006; Gao et al., 2012), in contrast to deciduous leaf waxes, which record only a brief period during the early growing season (Tipple et al., 2013). This implies that the hydrologic conditions of the entire growing season, including drier phases, are captured and averaged by the δD_{wax} signature of grasses. Considering the amount effect on precipitation in conjunction with the potential for evapotranspirational D-enrichment of leaf water, the resulting δD_{wax} values should thus enable a qualitative assessment of hydrologic changes, as both processes work in the same direction and amplify the variability of the signal.

Therefore, changes in the δD_{C31} signature are attributed to general humidity changes during the growing season. With a few exceptions, this is supported by enriched δD_{C31} compositions during dust pulses and low Al/Si ratios, thus indicating arid conditions in NW Africa (**Fig. 3.3**). Conversely, a shift in the δD_{C31} signature towards more negative values is seen as the result of intensified precipitation during the growing season and/or reduced evapotranspiration resulting from higher humidity. The ODP 659 record displays considerable δD_{C31} variability with a maximal shift of 34.9‰ (32‰ in the uncorrected record) between humid and arid periods. Within this range (−165.4‰ to −130.5‰), a mean value of −141.5‰ in the marine surface sediments indicates relatively dry conditions. Such climatic changes, reflected in the amplitude of δD_{C31} variations, resemble those detected off Senegal for the last 44 ka (Niedermeyer et al., 2010), giving support to further interpretations of arid/humid phases based on this proxy.

Interestingly, the δD_{C31} record is consistently anti-correlated ($r = -0.55$; $p < 0.01$) with the $\delta^{13}C_{C31}$ record, pointing to increased C_4 plant contributions (up to 90%) to the vegetation cover during wetter periods (depleted δD_{C31}). This relationship is even more pronounced for the *n*-C_{33} alkane ($r = -0.70$; $p < 0.01$), being a prominent homologue of C_4 grass waxes (Rommerskirchen et al., 2006a,b; Vogts et al., 2009). Usually, higher contributions of drought-adapted C_4 plants are expected under more arid conditions and vice versa (Ehleringer

et al., 1997). In order to explain this apparent contradiction in the ODP 659 isotope records, several factors have to be considered.

For instance, plant-dependent δD_{C31} variations may be related to differences in leaf anatomy, rooting depth and photosynthetic pathway (Sachse et al., 2012 and references therein). The $\delta^{13}C_{C31}$ signature indicates a total C_3/C_4 plant variability of 20% (70-90% C_4 plants). In general, C_4 grasses are D-depleted by ~20‰ relative to C_3 trees (McInerney et al., 2011) and D-enriched by ~20‰ relative to C_3 grasses (Smith and Freeman, 2006). This means that even in a hypothetical case of a pure contribution of either one of the two C_3 types (trees or grasses), the total C_3/C_4 plant variability of 20% in the ODP 659 $\delta^{13}C_{C31}$ record may account for a maximal shift of only ±4‰ of the total δD_{C31} variability and can thus not explain the observed δD_{C31} shifts of up to 32‰ between humid and arid periods. Hou et al. (2007) investigated 11 tree species from Blood Pond, MA (USA) and also found a negative relationship between plant-wax δD and $\delta^{13}C$ signatures ($R^2 = 0.55$). The authors suggest water use efficiency as an important control on δD_{wax} values in trees. However, with regard to the vast majority of C_4 plants (70-90%) reflected in the $\delta^{13}C_{C31}$ signal of ODP 659, it seems unlikely that minor amounts of C_3 plants exert such an impact on the relationship of plant-wax isotopes. In contrast, Bi et al. (2005) found a positive correlation of isotopes in trees ($R^2 = 0.72$) and a strong anti-correlation in herbaceous C_4 plants ($R^2 = 0.93$), attributed to plant physiology (tree, shrub and herb). The latter finding seems promising to explain the pattern in the isotopic data sets from ODP 659, but comparisons are hampered as the plants used by Bi et al. (2005) were sampled in a botanic garden, which underlies strong anthropogenic overprinting.

3.6.4 Plant-wax provenance

The specific location of ODP Site 659 and the potentially mixed contributions from different source areas provide the most promising interpretation to explain the observed anti-correlation of plant-wax isotopes. The core location is situated right beneath the main axis of today‘s dust plume over the NE Atlantic, which is dominated by low-altitude NETW (Chiapello et al., 1995). This predominance becomes apparent in the NE-SW-trend of Sr-Nd-isotopes in marine surface sediments (Grousset et al., 1998) and atmospheric dust samples (Skonieczny et al., 2011), as well as in grain size (Stuut et al., 2005) and clay mineral (Lange, 1982) distributions. Highest NETW intensities were reported for glacial periods (Sarnthein et al., 1981). It was inferred that the dust plume has been relatively stable during glacial-interglacial timescales (Sarnthein et al., 1981; Hooghiemstra et al., 2006). During times of enhanced NETW, however, an additional source area would contribute eolian dust. This is inferred to be located in southern Algeria and southwestern Libya based on clay mineralogy and Sr/Nd isotopic analyses from core MD03-2705 taken at the same position as ODP 659 (Jullien et al., 2007). If at all, this region would contribute only low amounts of plant-derived lipids, whereas vegetation north of the Sahara is dominated by C_3 plants (White, 1983).

Hence, it is most likely that the intensified trade winds essentially only supplied inorganic dust with minor organic material and that the majority of plant waxes in sediments from ODP 659 were always derived from the Sahel. The decreased relative C_4 plant contribution during arid dust events (as indicated by enriched δD_{C31} values) must thus be explained by decreased C_4 grass cover in the northern part of the Sahel, which is vulnerable to decreased rainfall (Dupont, 1993). The accompanied relative increase in C_3 plant contributions might be attributed to background supply from either one of the two C_3 domains (northern vs. equatorial, **Fig. 3.4**).

An origin of C_3 plant waxes from southern biomes seems unlikely, because the here-observed anti-correlation of isotopes (δD_{C31} vs. $\delta^{13}C_{C31}$) was not detected in the isotopic data sets obtained from a more proximal and southerly sediment core (Niedermeyer et al., 2010). In fact, plant-wax-specific isotopes from that core (GeoB9508-5; 15°N) correlate positively ($r = 0.57$; $p < 0.01$). In addition to the geographical position of core GeoB9508-5, the slight increases in C_3 plants during wet conditions suggest that this more southerly record tracks Intra-Sahelian variability or even the southern Sahel boundary. The fact that the pronounced C_3 maximum during the humid MIS 3 (50-45 ka) recorded at core GeoB9528-3 (9°N) coincides with highest C_4 contributions recorded at ODP 659, as already mentioned above, is another argument against a southern (more equatorial) C_3 source contributing to the ODP 659 wax record.

Alternatively, it has been suggested that an increased input of C_3 plant waxes and pollen in cores beneath the main dust plume may be related to biomes north of the Sahara (northern C_3 domain) due to stronger NETW (Zhao et al., 2003). This second scenario is supported by further palynological evidence for higher NETW intensity during glacial periods (Hooghiemstra and Agwu, 1986; Hooghiemstra et al., 2006). Notably, the difference between glacial (LGM, 20 ka BP) and interglacial (AHP, 9 ka BP), in terms of 'trade wind indicator' pollen distributions in marine sediments off NW Africa, matches well to the relative C_3/C_4 estimates derived from the $\delta^{13}C_{C31}$ record of ODP 659 (**Fig. 3.4**): Low C_3 plant-wax contributions (down to 10%) were found during humid phases (depleted δD_{C31}), in accordance with weaker NETW and a northward migration of the tropical rain belt. In contrast, relatively higher C_3 percentages (up to 30%) were found during arid phases (enriched δD_{C31}), reflecting enhanced southward wax transport from C_3-dominated biomes north of the Sahara. Most essential in this context is that the pollen taxa used as trade wind indicators are always derived from plants with a distinct origin from north of the Sahara and thus indicate input from the northern C_3 domain to the marine sedimentary record. For ODP 659, this also implies that the Canary Islands are the nearest potential source region for C_3 plant material (Dupont and Agwu, 1991; Hooghiemstra and Agwu, 1986; Hooghiemstra et al., 2006; **Fig. 3.4**). Thus, the similar glacial-interglacial variations further support the idea that carbon isotopes of plant waxes reflect relative contributions from two source areas (northern C_3 vs. 'Sahelian' C_4 domain).

Although the pollen indication of NETW strength is not a quantitative measure of the amount of transported C_3 plant material, we may use the difference between values for weak (interglacial) and strong (glacial) NETW (ca. 10% and 20-40%, respectively), which amounts to 2-4 times increased transport from northern latitudes during periods with strong NETW compared to those with weak NETW. The difference between minima and maxima $\delta^{13}C_{C31}$ is about 1-2.5‰, which amounts to less than 2 times C_3 plant-wax increase in most cases. Thus, intensified trade wind transport is more than sufficient to explain the $\delta^{13}C_{C31}$ variability. The impact on δD_{C31} variability is difficult to assess, as the δD_{C31} signature of the northern C_3 domain may vary substantially from that of the biomes south of the Sahara due to the influence of winter rainfall north of the Sahara (Nicholson, 2000). Nevertheless, the detected δD_{C31} amplitudes are in the same range as those detected off Senegal (Niedermeyer et al., 2010), which seem to be unaffected by the northern C_3 domain.

In summary, the consistent anti-correlation of the δD_{C31} and $\delta^{13}C_{C31}$ records is the most striking result and can be described according to Zhao et al. (2003) by changing contributions from generally two source areas (northern C_3 vs. 'Sahelian' C_4 domain). Nevertheless, due to the predominance of C_4 plants reflected in the ODP 659 $\delta^{13}C_{C31}$ record, the corresponding δD_{C31} signal is mainly shaped by the hydrologic conditions of biomes south of the Sahara, i.e. the Sahel, which is supported by proxy comparisons (XRF data and similar δD_{C31} ranges and timing of variability compared to core GeoB9508-5 off Senegal). Thus, episodic northward extensions of the tropical rain belt reflected in depleted δD_{C31} compositions triggered C_4 expansions (increased $\delta^{13}C_{C31}$ values and high *n*-alkane concentrations) into the Saharan realm. Conversely, a stronger C_3-plant-wax signal during arid conditions is seen as the result of both, C_4 retreat/southward shift of the Sahara-Sahel transition and larger contributions from biomes north of the Sahara transported by stronger NETW.

3.6.5 Causes of humidity changes

Transport of moisture is related to the atmospheric circulation, with NETW intensity as the limiting factor for the northward extent of the tropical rain belt and consequently of the vegetation (Nicholson, 2000; Mulitza et al., 2008). This coupling is of particular importance when discussing the underlying causes for the observed changes in our proxy records. Though we report contributions from generally two different source areas, deduced from $\delta^{13}C_{C31}$ variations, the hydrologic information obtained from the plant waxes can still be predominantly attributed to the area with major plant-wax supply. For ODP 659, this constitutes the Sahara-Sahel transition. In order to unravel the drivers of environmental changes, detected in the ODP 659 records, we investigated the relation of humidity indicators (δD_{C31}, Al/Si) to external forcing factors, like SST, AMOC and solar insolation (**Fig. 3.5**). SST off NW Africa, for instance, responds passively to higher North Atlantic SST changes by advective current transport (Niedermeyer et al., 2009). Moreover, a weakening of the AMOC was postulated to be the main trigger of millennial-scale droughts in the Sahel (Mulitza et al.,

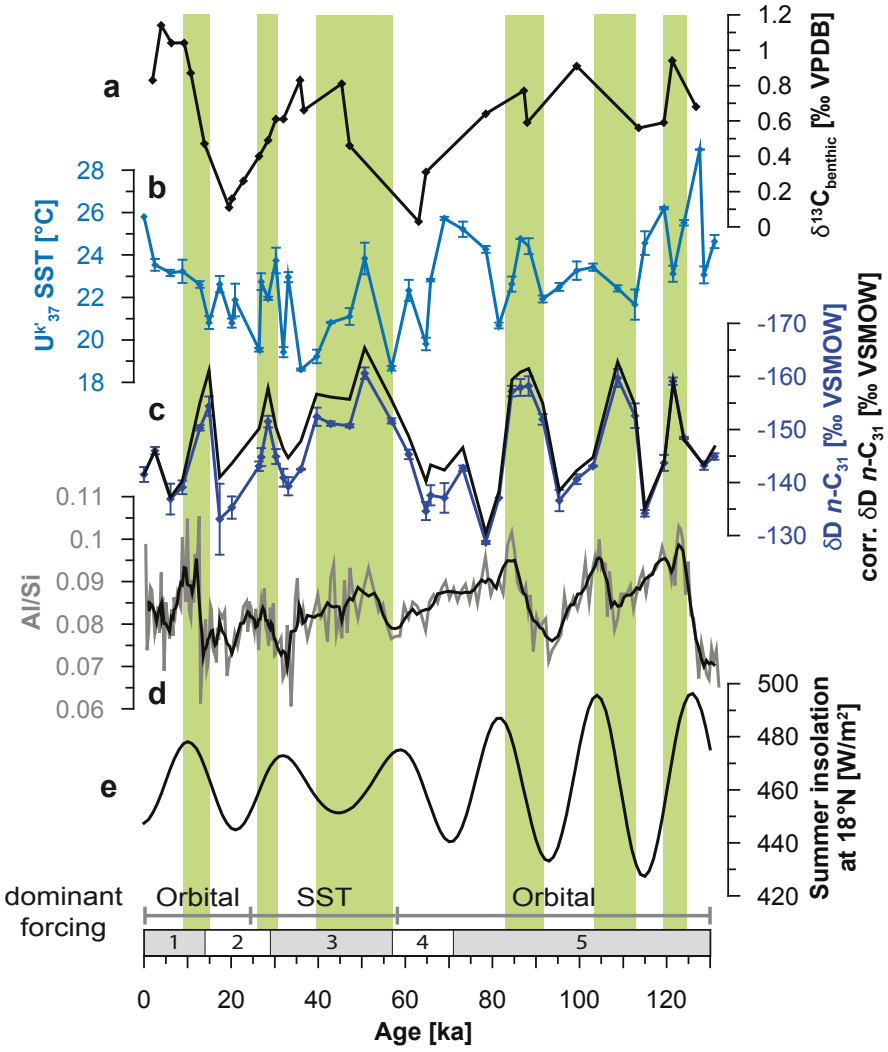

Fig. 3.5: Comparison of humidity changes with major forcings documented in the ODP 659 record: (a) $\delta^{13}C$ signature of the benthic foraminifera *Cibicidoides wuellerstorfi* (Sarnthein and Tiedemann, 1989); (b) $U^{k'}_{37}$-derived SST variability; (c) original (blue) and ice-volume-corrected δD values (black) of the *n*-C_{31} alkane; (d) Al/Si ratio with 5 point running mean (black curve); (e) Summer (JJA) insolation at 18°N (Berger, 1978). Error bars indicate the standard deviation of multiple measurements. Modern values ("0 ka") of the SST and δD records are calculated from the averaged results of the coretops. Marine Isotope Stages (MIS) are indicated on bottom. Green bars highlight humid periods reflected in the δD_{C31} signature.

2008; Tjallingii et al., 2008; Niedermeyer et al., 2009). Also on longer timescales, NW African vegetation distribution shows a link to AMOC variations (Castañeda et al., 2009). At ODP Site 659, however, we only find an insignificant correlation (r = 0.04) of humidity changes to AMOC strength reflected in the $\delta^{13}C$ signature of benthic foraminifera (Sarnthein and Tiedemann, 1989; **Fig. 3.5**). This finding should be regarded with caution as comparisons are hampered due to the different resolution of the records.

The best fit for the timing of δD_{C31} and Al/Si changes in our study is found for Northern Hemisphere solar insolation (**Fig. 3.5**), in agreement with dust flux analyses (Trauth et al., 2009). The general pattern of six humid phases reflected in the ODP 659 records during the last 130 ka coincides with the same number of insolation maxima, whereas the timing is not coherent throughout the whole time interval. In part this could be attributed to chronological

issues, mostly concerning the older part of the record. A potential offset of ~4 ka at ~128 ka BP towards older ages (Lisiecki and Raymo, 2009), as indicated in section 3.1, would indeed result in a better fit for both δD_{C31} and Al/Si with insolation variability. In contrast, hydrologic changes during MIS 3 and the early MIS 2 rather follow SST variability and seem to be decoupled from insolation changes (**Fig. 3.5**), which was also noted in previous studies (Tjallingii et al., 2008; Weldeab et al., 2007). Oceanic forcing of the African monsoon is a typical feature of modern climate variability (Giannini et al., 2003). A recent investigation of core MD03-2705, taken at the same position as ODP 659, showed a strong coupling of regional oceanography, upwelling dynamics and continental climate for the last 220 ka (Matsuzaki et al. 2011). However, the general pattern of our alkenone-based SST estimates only supports such a tight coupling during a restricted time window (**Fig. 3.5**). This is attributed to lower amplitudes in solar insolation allowing other forcing factors to become dominant. It has been suggested that summer insolation intensities have to pass a threshold of approx. 470 W/m^2 to induce rapid climate and vegetation shifts (deMenocal et al., 2000). Our results largely agree with the postulated threshold in terms of a general decrease in insolation forcing, as we infer arid conditions during the moderate insolation maxima at around 30 ka and 60 ka. Humidity changes during the period of reduced insolation forcing are associated with SST changes.

3.7 Conclusions

The δD and $\delta^{13}C$ signatures of long-chain *n*-alkanes from ODP Site 659 off NW Africa revealed a significant anti-correlation throughout the Last Glacial cycle (130 ka). Considering the specific core location and the corresponding catchment areas for plant-wax supply, this pattern reflects sensitive responses of the vegetation cover to precipitation changes in the Sahel region, accompanied by varying contributions from C_3 biomes north of the Sahara by NETW. During arid phases, when the West African monsoon is limited in its northward extent, the northern parts of the Sahel experience crucial water stress, resulting in a pronounced contraction of the C_4 vegetation cover. The corresponding increase in NETW strength during dry periods further promotes a more pronounced C_3-plant-wax signal derived from the northern C_3 domain. During humid periods, the C_4-dominated Sahelian environments spread northward into the Saharan realm, in association with lower NETW inputs of C_3 plant waxes. This interpretation is in accordance with terrigenous proxy comparisons (dust and XRF). Our results point to a shift from strong orbital insolation forcing with high amplitudes in variability (MIS 4 and 5) to SST forcing during low-amplitude insolation changes (MIS 3 and early MIS 2) and a move back to insolation-coupled hydro-variability (MIS 1 and 2). This study demonstrates that the combination of molecular proxies

provides a robust framework for continental paleoenvironmental reconstructions in terms of hydrology, vegetation and transport agents associated with plant-wax export.

3.8 Acknowledgements

This study was financially supported by the Deutsche Forschungsgemeinschaft (DFG) through the priority programme 527 “IODP/ODP“ (Sche903/11) with additional support by the Research Center/Excellence Cluster “The Ocean in the Earth System“ at MARUM — Center for Marine Environmental Sciences, University of Bremen. RRK acknowledges additional support by GLOMAR — Bremen International Graduate School for Marine Sciences. We thank an anonymous reviewer and Claude Hillaire-Marcel for helpful comments that improved the manuscript.

IV

Hybrid insolation forcing of Pliocene monsoon dynamics

Rony R. Kuechler, Lydie Dupont, Gerold Wefer and Enno Schefuß

MARUM – Center for Marine Environmental Sciences, University of Bremen, 28359 Bremen, Germany.

Keywords: Pliocene; West Africa; hydrology; vegetation; stable hydrogen isotopes; stable carbon isotopes; plant leaf waxes; orbital forcing; insolation; gradients

Submitted to *Geology*

4.1 Abstract

The Pliocene is regarded as a potential analog for future climate with conditions generally warmer-than-today and higher-than-preindustrial atmospheric CO_2 levels. Here we present the first orbitally resolved records of continental hydrology and vegetation changes from West Africa for two Pliocene time intervals (5.0-4.6 Ma, 3.6-3.0 Ma). Our results indicate that changes in local insolation alone are insufficient to explain the full degree of hydrologic variations. Generally two modes of interacting insolation forcings are observed: During eccentricity maxima, when precession was strong, the West African monsoon was driven by summer insolation. During eccentricity minima, when precession-driven variations in local insolation were minimal, obliquity-driven changes in the summer latitudinal insolation gradient became dominant. This hybrid monsoonal forcing concept explains orbitally-controlled tropical climate changes, incorporating the forcing mechanism of latitudinal gradients for the Pliocene, which increase in importance during subsequent Northern Hemisphere Glaciations.

4.2 Introduction

For the assessment of Pliocene climate conditions, focus has been on sea surface (Dowsett et al., 2013) and continental temperatures (Salzmann et al., 2013). Global mean annual temperatures were more than 3°C warmer and sea level was about 22 ±10 m higher than at present (Dowsett et al., 2013; Haywood et al., 2013b). However, data-model mismatches have been detected for terrestrial temperature estimates in the tropics likely due to limited proxy data (Salzmann et al., 2013). Moreover, a model intercomparison revealed inconsistencies in tropical precipitation estimates (Haywood et al., 2013b) indicating that more data on tropical hydrology are needed. Hydrogen isotopes of plant leaf waxes (δD_{wax}) provide a proxy for paleohydrologic variations related to the isotopic composition of precipitation (δD_{rain}; Sachse

et al., 2012). In tropical regions, δD_{rain} is negatively correlated to precipitation amounts (Dansgaard, 1964; Rozanski et al., 1993; Risi et al., 2008b), whereas δD_{wax} also incorporates secondary effects of evapotranspiration, plant physiology, and photosynthetic pathway (Sachse et al., 2012; see section 4.7.1). In areas with C_4 grasses, the stable carbon isotopic composition of the same compounds ($\delta^{13}C_{wax}$) provides additional information about vegetation changes and can be used to differentiate between contributions from grassy (C_4) and woody (C_3) vegetation (e.g., Vogts et al., 2009).

The modern vegetation distribution and composition in West Africa (**Fig. 4.1**) reflects the latitudinal migration of the tropical rain belt (White, 1983): Close to the equator, high precipitation rates lead to dense vegetation cover, consisting of tropical rain forests and woodlands (mostly C_3). Further to the north, towards the Sahara desert, increasingly open grasslands (mostly C_4) occur as rainfall decreases and wet season length shortens. North of the Sahara, the Mediterranean vegetation is composed of shrublands, steppes and forests, which consist exclusively of C_3 plants.

In general, orbital-scale African monsoon variability is mainly attributed to variations in low-latitude summer insolation, which is dominated by 19 kyr and 23 kyr periodicities of the precession cycle (Kutzbach, 1981; Rossignol-Strick, 1983; Tiedemann et al., 1994; deMenocal, 1995, 2004; Gasse, 2006; Ruddiman, 2006; Larrasoaña et al., 2013). Consequently, maximum insolation intensities are expected to increase monsoon circulation and thus rainfall, comparable to modern seasonal variations. Nevertheless, also obliquity (41 kyr) cycles have been detected in sequences of Mediterranean sapropels (Lourens et al., 1996a), whose formation depends on monsoonal fresh-water discharge from Africa (see section 4.7.2). Equally, dust flux rates at Ocean Drilling Program (ODP) Site 659 (Tiedemann et al., 1994) and pollen flux rates at ODP Site 658 (Dupont et al., 1989) show obliquity cycles, which are difficult to explain, since obliquity has a negligible effect on low-latitude insolation (e.g., Laskar, 1990).

We focus on ODP Site 659, situated offshore West Africa and centered beneath the main wind trajectories (**Fig. 4.1**). Its dust record provides evidence for the persistence of orbital arid-humid cycles during the last 5 Ma (Tiedemann et al., 1994). Coupled δD_{wax} and $\delta^{13}C_{wax}$ analyses from this site for the LGC have demonstrated their ability to record shifts in West African hydrology and vegetation (Kuechler et al., 2013). However, δD_{wax} studies from West Africa covering the Pliocene do not exist. Here we provide orbitally resolved δD_{wax} and $\delta^{13}C_{wax}$ records for two time intervals (5.0-4.6 Ma and 3.6-3.0 Ma) to evaluate hydrologic changes in Pliocene West Africa. In addition to the well-established precession forcing, we discuss further insolation mechanisms, like interhemispheric and latitudinal gradients, to explain the long-term evolution of the West African hydrologic cycle.

4.3 Materials and methods

ODP Site 659 is located on top of the submarine Cape Verde Plateau at 3070 m water depth (**Fig. 4.1**). The siliciclastic fraction is considered to be of purely eolian origin due to low carbonate concentrations in the dust composition and its distal location on a submarine rise excluding fluvial input (Tiedemann et al., 1994). Two Pliocene age models have been established based on variations in dust accumulation (Tiedemann et al., 1994) and benthic $\delta^{18}O$ (Clemens, 1999). The latter is used in this study, since it allows a more precise correction for the effects of global ice volume on the δD_{wax} record using the global benthic $\delta^{18}O$ stack (Lisiecki and Raymo, 2005).

δD_{wax} and $\delta^{13}C_{wax}$ analyses were carried out on 230 samples with an average temporal resolution of ~4 ka, comparable to the dust record (Tiedemann et al., 1994). A sampling gap between 3.33-3.29 Ma is related to a core break. A detailed description of methods, including lipid extraction, quantification and stable isotope analyses, is given in Kuechler et al. (2013). δD values are reported relative to Vienna Standard Mean Ocean Water (VSMOW). An external *n*-alkane standard yielded a precision (1σ) and accuracy of 2‰, and squalane as internal standard yielded values of 2‰ and 1‰, respectively. The mean precision (1σ) of replicates for the n-$C_{29\text{-}33}$ alkanes is 2‰. δD_{wax} values were adjusted for changes in global ice volume (see section 4.7.1). $\delta^{13}C$ values are reported relative to the Vienna PeeDee Belemnite (VPDB) standard. The external standard yielded a precision (1σ) of 0.3‰ and an accuracy of 0‰. The values for internal standard are 0.2‰ and 0.3‰, respectively. Replicates yielded a mean precision (1σ) for the n-$C_{29\text{-}33}$ alkanes of 0.2‰. Data sets are stored online at PANGAEA (www.pangaea.de).

In order to illustrate the temporal evolution of the dust and δD_{wax} records, we applied continuous wavelet transform (Morlet) after Torrence and Compo (1998) using the software

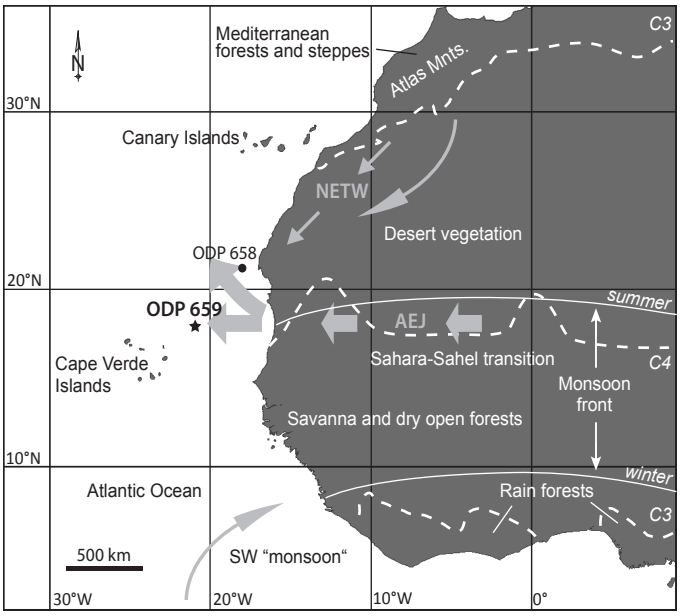

Fig. 4.1: Location of Ocean Drilling Program (ODP) Sites 659 (star; 18°05'N, 21°02'W, 3070 m water depth) and 658 (dot; 20°45'N, 18°35'W; 2263 m water depth) offshore West Africa. Main vegetation zones (dashed lines; simplified after White, 1983), dominant photosynthetic pathways (right), atmospheric trajectories (arrows), and summer/winter position of the monsoon front are indicated. The thickness of the arrows marks the different altitudes of the African Easterly Jet (AEJ; >3000 m) and the North-East Trade Winds (NETW; <1000 m).

PAST 3.0 (Hammer et al., 2001; **Fig. 4.2**). For this statistical procedure, data sets were linearly interpolated to an even spacing of 4 kyr. Signal power of orbital periodicities (precession, obliquity, eccentricity) is expressed in different shadings, with the significance level (p = 0.05; black contours) after a chi-squared test with the null hypothesis of a white noise model. The cone of influence (black line) identifies the area of boundary effects.

4.4 Results and discussion

4.4.1 Plant-wax provenance and vegetation sources

Plant-wax-derived long-chain *n*-alkane concentrations from ODP Site 659 mostly vary between 0.01-0.8 μg g^{-1} dry sediment and are clearly coupled to dust accumulation (Tiedemann et al., 1994), suggesting predominant eolian transport (see sections 4.7.2 and 4.7.3). Carbon preference indices (CPI) yield values of mostly >3, indicating terrestrial plant contributions (Eglinton and Hamilton, 1967). Isotopic signatures of major homologues significantly correlate (see section 4.7.1.3). Therefore, we focus on the *n*-C_{31} alkane as the most abundant compound, attributed to the prevailing C_4 grass input (Vogts et al., 2009).

Pliocene $\delta^{13}C_{wax}$ values display a narrow range between –26.5‰ and –24.4‰, clearly below the enriched values of –23‰ observed for the LGC (Kuechler et al., 2013). The low $\delta^{13}C_{wax}$ variations are attributed to two main aspects: (1) a relatively stable wind system (Tiedemann et al., 1994) and thus a persistent provenance of plant waxes, and (2) the integration of a large source area. The Last Glacial pattern of relative increases in C_3 plant-wax material during arid phases attributed to enhanced contributions by trade winds (Kuechler et al., 2013) is not detected for the Pliocene (see sections 4.7.2). This suggests that only small amounts of plant waxes derived from Mediterranean sources because trade winds were weak, in line with the pollen records of ODP Sites 658 (Leroy and Dupont, 1994) and 659 (Vallé et al., 2014; **Fig. 4.1**). Thus, depleted $\delta^{13}C_{wax}$ values indicate higher C_3 plant coverage at the latitude of the Sahel compared to today suggesting more humid conditions. Relative to the LGC with a C_4 maximum of ~90 %, we estimate a decreased occurrence of C_4 plants by ~20 % in the Sahel during the Pliocene (see also section 4.7.1).

4.4.2 Multiple insolation forcings

δD_{wax} values range from –171‰ to –133‰ and show – in agreement with the dust record (Tiedemann et al., 1994) – alternating arid-humid conditions (**Fig. 4.2**), thus supporting previous dust-based conclusions and the use of δD_{wax} as humidity proxy (see section 4.7.1). However, variations in low-latitude insolation cannot explain the entire variability in the δD_{wax} and dust records since some humid (arid) periods occur prior to insolation maxima (minima) or even coincide with insolation minima (maxima). Moreover, statistical evidence clearly indicates a more complicated pattern with additional periodicities unrelated to

precession. These periods, in which humidity changes do not follow low-latitude insolation, turn out to be linked to obliquity (**Fig. 4.2**).

The mechanistic basis for the obliquity signal in low-latitude climate records is a matter of debate. Modeling studies show contrasting results, both including (Tuenter et al., 2003; Weber and Tuenter, 2011) and excluding (Bosmans et al., 2014) an influence of the high latitudes. On the one hand, obliquity in the tropics is attributed to higher moisture transport from mid/ high latitudes (Tuenter et al., 2003) or varying ice sheets and greenhouse gases (Weber and Tuenter, 2011) that influence the monsoon intensity and timing. On the other hand, recent modeling studies revealed an increase in monsoonal rainfall due to a stronger atmospheric pressure contrast between the West African continent (low pressure) and the South Atlantic (high pressure) under conditions of low precession (i.e. maximum local insolation) and high obliquity. Based on this, the interhemispheric (or cross-equatorial) insolation gradient at lower latitudes was suggested to drive winds and associated moisture transport (Bosmans et al., 2014). Notably, a northward shift of the tropical monsoon front when obliquity was high is in agreement with proxy data, indicating a strong influence of the latitudinal insolation gradient (LIG) between high and low latitudes (Davis and Brewer, 2009), which is dominated by obliquity during summer (**Fig. 4.2**). In general, insolation gradients shape the climate system by differential heating and thus determine spatial temperature patterns, which ultimately steer atmospheric pressure gradients (Nicholson, 2009). On orbital timescales, the so-called "gradient hypothesis" explains the periodicity of glacial-interglacial cycles with the high-to-low-latitude contrast in insolation (i.e. LIG) forcing moisture fluxes poleward via strong gradients, thus triggering ice sheet growth (Raymo and Nisancioglu, 2003). In this context, most studies focus on high latitudes and studies considering a latitudinal gradient forcing of tropical monsoon systems are limited to the LGC (e.g., Davis and Brewer, 2009). It has been suggested that summer LIG weakening during high obliquity would lead to a northward shift of the tropical monsoon front (Davis and Brewer, 2009; **Fig. 4.2**). This was recently supported by another climate model, indicating a tight link between the LIG-controlled mid-latitude eddy circulation (driving the heat and moisture transport from low to high latitudes) and the poleward boundary of the tropical rain belt (Mantsis et al., 2014). For the West African Sahel the strongest monsoonal influence would thus be expected during the weakest summer LIG, shifting the tropical rain belt northward, instead of being purely triggered by local insolation. For the Pliocene, both proxy data and model results confirm reduced meridional and zonal temperature gradients when the tropical monsoon was enhanced (Dowsett et al., 2013; Haywood et al., 2013b). Still, none of the above mentioned forcing mechanisms is able to solely explain the variations in the δD_{wax} and dust records (see also section 4.7.4).

Based on our results from the Pliocene and comparison with the LGC we propose a modified gradient forcing mechanism, which is independent of tectonically-driven changes in ocean circulation (see section 4.7.5). Wavelet analyses show repeated shifts in the periodicity of the δD_{wax} and dust records from the obliquity to the precession band and vice versa,

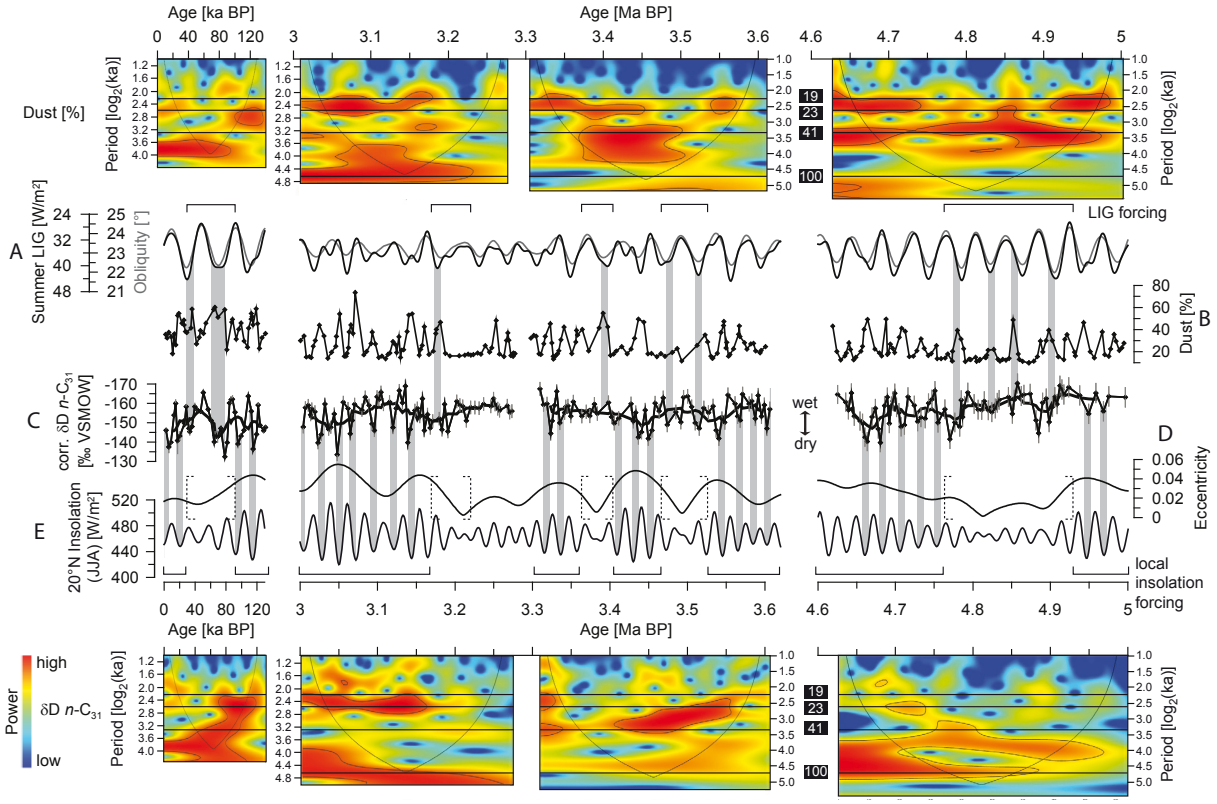

Fig. 4.2: Multiple insolation forcings. A: Latitudinal insolation gradient (LIG; 30-60°N) during boreal summer (JJA; black; Davis and Brewer, 2009) and obliquity (grey). B: Dust record (Tiedemann et al., 1994). C: Ice-compensated δD of the *n*-C_{31} alkane (Last Glacial cycle data from Kuechler et al., 2013). D: Eccentricity. E: Summer (JJA) insolation at 20°N. Orbital parameters calculated after Laskar, (1990). Vertical grey bars link dry phases with the dominant forcing as indicated on top and bottom. Dashed brackets highlight periods of low eccentricity during which the major forcing switches to summer LIG. Continuous wavelet transform (Morlet) of dust and δD for the investigated time intervals are shown on top and bottom, respectively (after Torrence and Compo, 1998). Main orbital periodicities of precession (19/23 kyr), obliquity (41 kyr), and eccentricity (100 kyr) are indicated.

depending on the amplitudes in precession and obliquity. We infer a consistent pattern with generally two modes (**Fig. 4.2**): During periods with strong precession cycles (i.e. high eccentricity), the influence of summer LIG on monsoon variability is superimposed by changes in local insolation. In contrast, during weak precession cycles, summer LIG forms the primary forcing of the West African monsoon and its influence on the northward distribution of atmospheric moisture plays the decisive role for the West African climate. This is also supported by climate models, which show a strong dependency of the obliquity-induced precipitation response to precession, but not vice versa (Tuenter et al., 2003). The indication for LIG forcing during the Mid-Pliocene is less pronounced than during the Early Pliocene and the LGC due to low variations in obliquity and accordingly, a relatively stronger precession component in the summer LIG (**Fig. 4.2**). LIG-induced climate shifts during the LGC are more severe than during the (Early) Pliocene due to increased ice-albedo feedbacks (Raymo and Nisancioglu, 2003). In addition, the duration of humid-arid periods seems to increase in the course of the LGC, reflecting the shift from one dominant forcing to another, i.e. from precession to obliquity. These findings caution against a too simplified view on

orbital forcing mechanisms of the (tropical) hydrologic cycle and hence, related records. In general, our findings highlight the influence of the West African monsoon for Mediterranean sapropel formation, and corroborate a recurrent greening of the Sahara, which might have intermittently allowed hominin migration through otherwise hostile territory (Larrasoaña et al., 2013). However, our new concept affects the timing of these events (see section 4.7.2).

4.5 Conclusions

Our new West African monsoon records suggest that orbital forcing is indeed the major control of monsoon variability, but indicate that changes in local summer insolation are insufficient to explain the full degree of hydrologic variations. We infer a hybrid insolation forcing with two modes, depending on the strength of the precession cycle: During high eccentricity (strong precession fluctuations), the main driver is the precession-controlled local summer insolation, but during low eccentricity, the obliquity-controlled summer LIG dominates. This new forcing concept accounts for the forcing mechanism of subsequent NHG, and should have basic implications for paleoclimate/-environmental records linked to the West African monsoon.

4.6 Acknowledgements

We thank B. Beckmann, W. Bevern, T. Evans and M. Yavuz for assistance in the laboratory, S. Clemens for providing the data of the revised age model, and R. Tiedemann for comments and discussion. This study was financially supported by the Deutsche Forschungsgemeinschaft (DFG) through the priority program 527 “IODP/ODP“ (Sche903/11) with additional support by the Research Center/Excellence Cluster “The Ocean in the Earth System“ at MARUM – Center for Marine Environmental Sciences, University of Bremen. RRK acknowledges further support by GLOMAR – Bremen International Graduate School for Marine Sciences.

4.7 Supplementary information

4.7.1 Influences on the plant-wax δD record

4.7.1.1 Precipitation δD and the amount effect

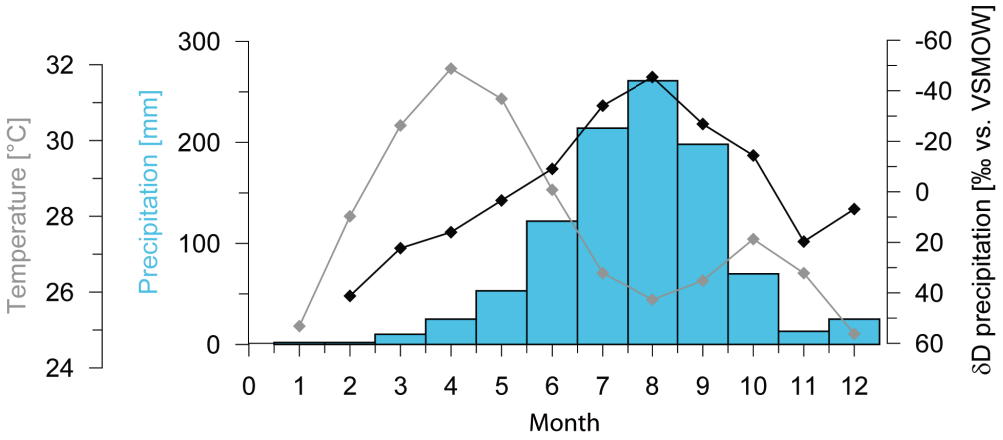

Fig. 4.3. Monthly precipitation amount-δD relationship and temperature at Bamako (Mali, 12° 41' 24", -7° 59' 24", 381 m) exemplifying the amount effect (Dansgaard, 1964) in West African hydrology (IAEA/WMO, 2014). This relationship is shown for monthly means, but also holds true on an annual basis (e.g., Rozanski et al., 1993).

4.7.1.2 Effect of vegetation composition

Differences in leaf anatomy, rooting depth and photosynthetic pathway may contribute to the final plant-wax δD signal (Sachse et al., 2012). Overall, C_4 grasses are D-depleted by ~20‰ relative to C_3 trees (McInerney et al., 2011) and D-enriched by ~20‰ relative to C_3 grasses (Smith and Freeman, 2006). Plant-wax $\delta^{13}C$ provides a hint to vegetation shifts (i.e., C_3 vs. C_4; e.g., Castañeda et al., 2009; Kuechler et al., 2013). The small absolute $\delta^{13}C$ variability of ~2‰ (between –26.5‰ and –24.4‰ for the *n*-C_{31} alkane) would correspond to a vegetation shift between C_3 vs. C_4 plants of less than 20%, when using the $\delta^{13}C$ end-members of –35.2‰ for C_3 plants and –21.7‰ for C_4 plants (Castañeda et al., 2009). The corresponding difference in hydrogen isotopic fractionation would be less than ±4‰. Considering the large variability in the plant-wax δD record (between –171‰ and –133‰ for the *n*-C_{31} alkane), such minor plant-dependent variations are negligible for paleohydrologic conclusions drawn in this study.

Pollen records from ODP Sites 658 (Leroy and Dupont, 1994) and 659 (Vallé et al., 2014) indicate that Pliocene sub-Saharan savannahs have no modern analog, which harbors the potential for further uncertainties in the plant-wax δD record. Nevertheless, modern analogs are also missing for the last African Humid Period (AHP) during the Holocene (Watrin et al., 2009). These authors emphasize that instead of a homogenous latitudinal shift of vegetation zones as a whole, individual plant species likely have an advantage over others. Notably,

δD_{wax} studies from offshore NW Africa covering the AHP yield a robust humid signal among different records (Niedermeyer et al., 2010; Collins et al., 2013; Kuechler et al., 2013), implying that they are apparently unaffected by a "non-analogous" vegetation composition. Finally, residence/transport times of plant waxes extracted from modern dust samples from offshore W Africa yielded a radiocarbon age of 650 ± 150 years (Eglinton et al., 2002). Since our records have a ~4 kyr resolution, such potential contributions from pre-aged plant waxes are considered to have a negligible effect on our interpretations.

4.7.1.3 Effect of evapotranspiration

Aridity may exert a considerable influence on the apparent fractionation (ε) between plant waxes and meteoric water via evapotranspiration and associated D-enrichment (Polissar and Freeman, 2010; Douglas et al., 2012; Kahmen et al., 2013a,b). It was found that such an effect is less pronounced in lake sediments compared to soils, likely due to the higher potential of lakes to integrate large catchment areas and small-scale variability related to differences in microclimate and vegetation (Douglas et al., 2012). In our study, the terrigenous fraction of marine sediments is considered to have a primarily eolian origin from large parts of circum-Saharan environments, especially from the Sahel (Tiedemann et al., 1994). Recently, Gao et al. (2014) investigated aerosols from arid and humid subtropical environments and found only minor deviations in ε (< 10‰), attributed to a possible compensation of isotopic enrichment due to decreasing relative humidity by a shift from trees to grasses in the vegetation.

4.7.1.4 Compensation of the ice volume effect on the plant-wax δD record

The δD record of the *n*-C_{31} alkane was adjusted for changes in global ice volume (Tierney and deMenocal, 2013). The Last Glacial Maximum was scaled to 1‰ (Schrag et al., 2002) in the LR04 global benthic $\delta^{18}O$ stack (Lisiecki and Raymo, 2005) relative to the present (0‰), and subsequently converted into δD values, using the global meteoric water line. Though the δD adjustment for the Pliocene is almost negligible (in the range of ±2‰), the procedure determines the use of the revised age model (Clemens, 1999), which is based on $\delta^{18}O$ variability at ODP Site 659 and thus better matches the LR04 stack (Lisiecki and Raymo, 2005; **Fig. 4.4**).

4.7.2 Link to Mediterranean sapropel formation

In general, sapropel formation in the Mediterranean Sea is documented since the Late Miocene (Colleoni et al., 2012) and linked to peak humid periods in N Africa, when fresh-water discharge through the Nile and additional, but no longer active drainage systems along the N African continental margin west of the Nile disrupted deep-water formation in the Mediterranean resulting in anoxic bottom sediments (Larrasoaña et al., 2013 and references therein). Recently, Larrasoaña et al. (2013) pointed out that sapropels constitute the only continuous record prior 130 ka to identify peak humid periods in N Africa. The mid-point of

each sapropel was tuned to 65°N summer insolation with an assumed response lag of 3 kyr based on the timing of the youngest sapropel (S1) to maximum summer insolation during the Holocene and concomitant humid conditions in Africa (Hilgen, 1991; Lourens et al., 1996a,b). According to Emeis et al., (2000), the inferred ages still remain preliminary. In this context, our concept of a hybrid insolation forcing challenges the assumption of a fixed forcing mechanism related to precession and its application for orbital tuning. The orbital configuration during which sapropel S1 was deposited reveals that the insolation maximum is in-phase with the latitudinal insolation gradient (LIG) minimum, thus obscuring a potential LIG influence (e.g., see **Fig. 4.5**). This also raises the question about the importance of phase relationships between precession and obliquity, as already noted in previous studies (e.g., Kukla et al., 1981; Clemens and Prell, 2007).

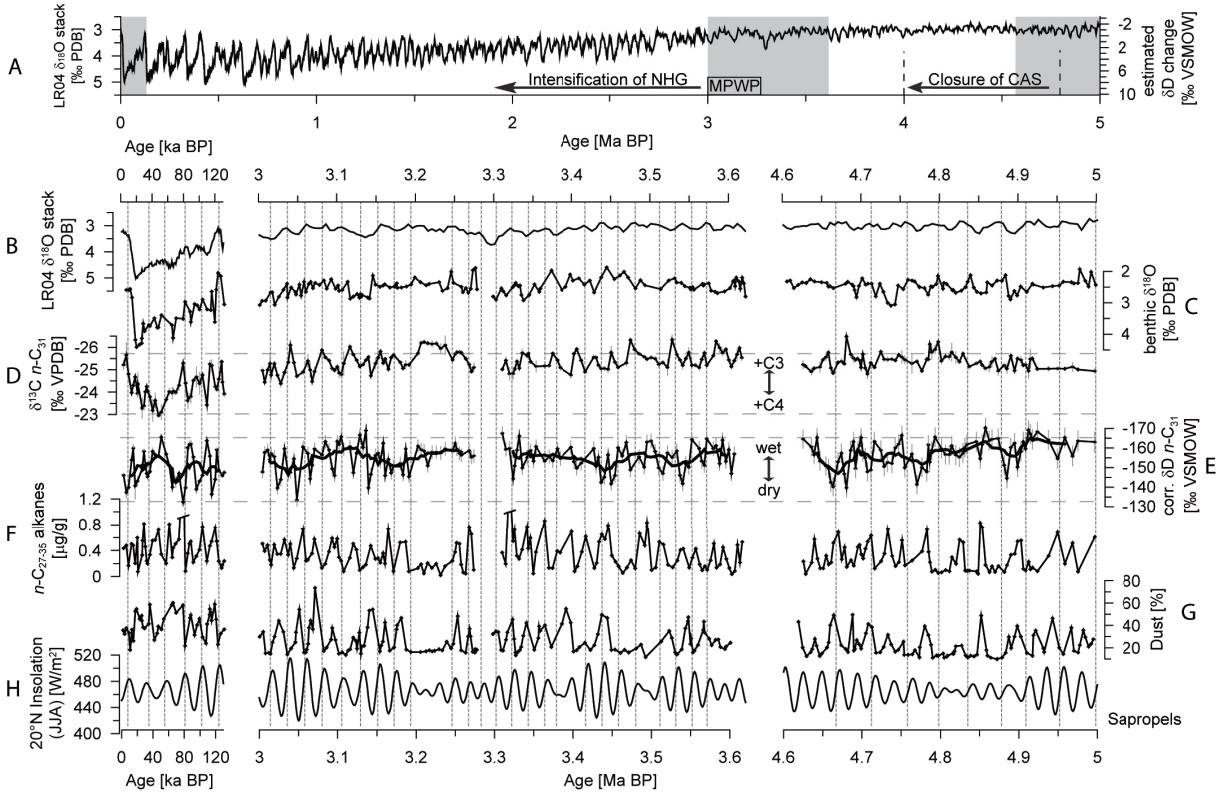

Fig. 4.4: West African hydrology and vegetation during the Pliocene recorded at ODP Site 659, compared to the Last Glacial cycle (Kuechler et al., 2013). A: LR04 benthic $\delta^{18}O$ stack (left axis; Lisiecki and Raymo, 2005) and, based on this, estimated δD change (right axis) used for adjustment of the plant-wax δD record for varying ice volume (see above), with major events (horizontal arrows) and time intervals discussed in this study (grey bars). The progressive closure of the Central American Seaway (CAS; Steph et al., 2010), the Mid-Piazencian Warm Period (MPWP; Dowsett et al., 2013), and the intensification of Northern Hemisphere Glaciations (NHG) are indicated. B: Close up of (A) for the investigated time intervals. C: benthic $\delta^{18}O$ record of ODP 659 (Tiedemann et al., 1994). D: Plant-wax $\delta^{13}C$ and E: δD values of the *n*-C_{31} alkane. Ice-compensated δD is based on (A). Long-term variability is indicated by the 7 pt. running mean (thick line). Horizontal dashed lines in (D) and (E) are isotopic ranges during the Last Glacial cycle. F: Long-chain *n*-alkanes (*n*-$C_{27\text{-}35}$; µg g^{-1} dry sediment). Note two off-scale maxima at 78.5 ka and 3.319 Ma. The corresponding values are 1.84 and 1.57 µg g^{-1}, respectively. G: Dust record (Tiedemann et al., 1994). H: Summer (JJA) insolation at 20° N (Laskar, 1990). Mediterranean sapropel layers (Emeis et al., 2000) are indicated by vertical dashed lines. Offsets between sapropels and insolation maxima increase back in time due to different astronomical solutions used for tuning, i.e., Laskar et al. (1993) and Laskar (1990), respectively. The same accounts for the slight offsets between the LR04 stack and the ODP 659 $\delta^{18}O$ record. Note the longer (obliquity-scale) periodicities in the sapropel record during the Early Pliocene coinciding with humid conditions reflected in the δD_{wax} and dust records.

4.7.3 Correlations

Table 4.1: Correlations (r- and p-values) for plant-wax-specific stable isotopes, long-chain *n*-alkanes and dust concentrations at ODP Site 659

n-C_x	LGC	p	MPWP	p	pre-MPWP	p	EP	p
δD								
29/31	0.80	< 0.01	0.85	< 0.01	0.70	< 0.01	0.70	< 0.01
31/33	0.74	< 0.01	0.83	< 0.01	0.58	< 0.01	0.63	< 0.01
29/33	0.73	< 0.01	0.79	< 0.01	0.52	< 0.01	0.56	< 0.01
$\delta^{13}C$								
29/31	0.86	< 0.01	0.87	< 0.01	0.82	< 0.01	0.60	< 0.01
31/33	0.78	< 0.01	0.70	< 0.01	0.64	< 0.01	0.51	< 0.01
29/33	0.62	< 0.01	0.66	< 0.01	0.73	< 0.01	0.41	< 0.01
δD vs. $\delta^{13}C$								
29	*-0.08*	*0.67*	0.42	< 0.01	*0.20*	*0.08*	*0.12*	*0.24*
31	-0.55	< 0.01	0.36	< 0.01	*-0.04*	*0.76*	*-0.23*	*0.03*
33	-0.70	< 0.01	*0.01*	*0.91*	*-0.10*	*0.38*	*0.05*	*0.61*
δD_{31} vs. dust%								
	0.34	*0.02*	0.41	< 0.01	*0.21*	*0.06*	*0.23*	*0.02*
n-$C_{27\text{-}35}$ vs. dust%								
	0.36	*0.02*	0.48	< 0.01	*0.16*	*0.16*	0.70	< 0.01

Note: For statistical analyses (PAST 3.0; Hammer et al., 2001), the Mid-Pliocene interval was split into the Mid-Piazencian Warm Period (MPWP; 3.273-3.007 Ma) and the preceding one (pre-MPWP; 3.616-3.309 Ma) separated by a stratigraphic gap of ~36 kyr in the sedimentary record. The Early Pliocene (EP) interval ranges from 4.997-4.625 Ma. Data sets were re-sampled to create evenly spaced records, according to the original average temporal resolution of 4 kyr. Values for the Last Glacial cycle (LGC; last 130 kyr) are given for comparison. Most r-values exhibit p < 0.01, except were highlighted (in italics).

4.7.4 Equal orbital signatures

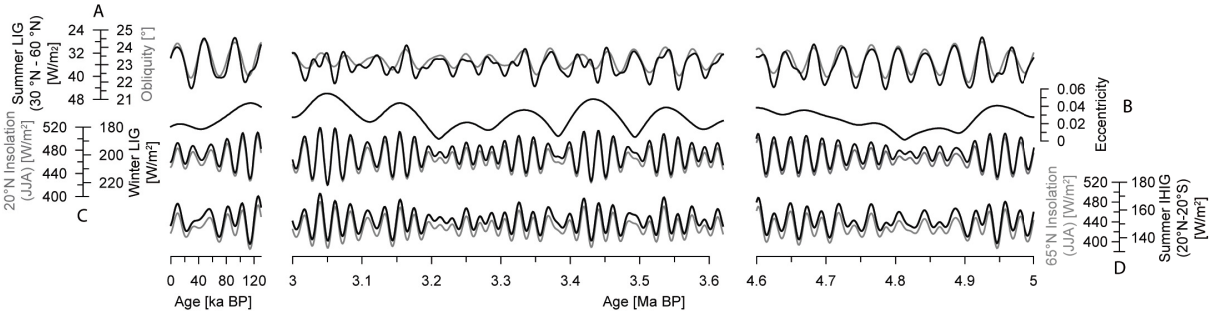

Fig. 4.5: Equal orbital signatures (Laskar, 1990). A: Latitudinal insolation gradient (LIG) during boreal summer (JJA) between 30 and 60 °N (black) and obliquity (grey). B: Eccentricity, modulating the influence of precession on insolation changes. C: Summer (JJA) insolation at 20 °N (grey) and LIG during boreal winter (DJF; black). The similarity arises from the dominant influence of the lower latitude component on the winter LIG due to polar night conditions at high latitudes. D: Interhemispheric insolation gradient (IHIG) during boreal summer (JJA) between 20 °N and 20 °S (black) and summer (JJA) insolation at 65 °N (grey). Both are under the influence of the same orbital forcing, but contain a stronger obliquity component than the low-latitude insolation. Note that insolation maxima are in-phase with IHIG maxima and reduced winter LIG due to the dominant precession forcing in the orbital records.

4.7.5 Closure of the Central American Seaway

For the Last Glacial cycle, several studies showed a strong impact of the Atlantic Meridional Overturning Circulation (AMOC) on vegetation and climate of the Sahel during Heinrich Events (Mulitza et al., 2008; Niedermeyer et al., 2009; Bouimetarhan et al., 2012; Handiani et al., 2013). Therefore, it was expected that during the Pliocene, the progressive shoaling of the Central American Seaway (CAS) between 4.8-4.0 Ma (Steph et al., 2010) should have had an impact on West African hydrology via increased AMOC and deep-water formation presumably leading to overall wetter conditions in West Africa. However, the δD_{wax} record shows the same pattern before and after the CAS closure, comparable to the variability during the LGC (Kuechler et al., 2013; **Fig. 4.4**) indicating orbital forcing as the main driver of West African hydrology. Therefore we conclude that the CAS closure (Steph et al., 2010) had no substantial effect on the Pliocene West African monsoon. Likely, Pliocene climate conditions (limited Northern Hemisphere Glaciations, NHG) dampened the influence of the AMOC on West African hydrology. As indicated by the ODP Site 659 pollen records, the increase of aridity was related to trade wind strengthening following the intensification of NHG, starting ~2.7 Ma ago (Vallé et al., 2014).

V

Tracking the meridional hydrologic gradient across West Africa by plant-wax-specific hydrogen and carbon isotopes in marine surface sediments

Rony R. Kuechler[a], Eva M. Niedermeyer[a,b], Britta Beckmann[a], Lydie M. Dupont[a], Matthias Prange[a], Gerold Wefer[a] and Enno Schefuß[a]

[a]MARUM – Center for Marine Environmental Sciences, University of Bremen, 28359 Bremen, Germany

[b]Current address: Senckenberg Biodiversity and Climate Research Centre (BiK-F), 60325 Frankfurt am Main, Germany

Keywords: West Africa; hydrology; vegetation; marine surface sediments; plant leaf waxes; hydrogen isotopes; carbon isotopes

In preparation for *Geochimica et Cosmochimica Acta*

5.1 Abstract

Understanding the hydrologic cycle is of vital importance for the interpretation of past and the prediction of future climate changes. A promising method to assess past precipitation changes is based on the stable hydrogen isotopic composition of plant-wax-derived long-chain *n*-alkanes (δD_{wax}), which depends on that of precipitation (δD_p), but is also exposed to other influences. In order to strengthen our understanding of its environmental significance and thus, its application in a paleoclimatic context, this study investigates the link between δD_{wax} in marine surface sediments and δD_p across a large hydrologic gradient. We analyzed 57 samples off the West African coast spanning a transect between 31-9°N. Complementary stable carbon isotopes of the same compounds ($\delta^{13}C_{wax}$) agree well with previously published results, indicating a maximum in C_4 plant contribution at the latitude of the Sahel, while C_3 plants dominate off Morocco and Guinea corresponding to the vegetation cover. Notably, independent of the large latitudinal shifts in climate and vegetation, the apparent fractionation (ε) of the *n*-C_{31} alkane stays relatively constant (around −126‰) along the transect and revealed the best correlation with annual δD_p compared to that of the *n*-C_{29} and *n*-C_{33} alkanes. In contrast, the latter two compounds correlate significantly with $\delta^{13}C_{wax}$ and mean air temperatures, indicating a strong influence of vegetation changes and, likely, related differences in water use efficiency on the corresponding δD_{wax} signatures. These differences are most apparent in the northern half of the transect, between Morocco and the Sahel, while for the southern half, δD_{wax} and ε values yield minor deviations among homologs despite of mixed C_3/C_4 contributions. For West Africa we thus conclude that

the *n*-C_{31} alkane appears most suitable to derive paleohydrologic reconstructions from marine sediments. Furthermore, the distinct latitudinal patterns in δD_{wax} and $\delta^{13}C_{wax}$ suggest that changes in the isotopic offsets between homologs might serve as indicators of latitudinal shifts in climate and vegetation.

5.2 Introduction

Plant waxes cover the leaves of almost all land plants and serve as protection against external stress (Hall and Jones, 1961; Eglinton and Hamilton, 1963; Shepherd and Griffith, 2006; Samuels et al., 2008). A major constituent of these wax coatings are long-chain *n*-alkanes with an odd-over-even carbon number (C_{25}-C_{35}) predominance (Chibnall et al., 1934; Eglinton and Hamilton, 1967), numerically expressed as the carbon preference index (CPI) with commonly higher values (>3) for plant-wax-derived *n*-alkanes (Bray and Evans, 1961; Eglinton and Hamilton, 1963; Mazurek and Simoneit, 1984; Collister et al., 1994). Following their original function, plant-wax-derived compounds remain intact after removal, transport by winds/rivers and final burial (Eglinton and Eglinton, 2008). Their resistance to degradation and diagenetic effects (e.g., Sessions et al., 2004; Schimmelmann et al., 2006) is an important prerequisite for their increasing application in paleoclimate studies. An essential component of climate change is precipitation variability, for which the stable hydrogen isotopic composition of plant waxes (δD_{wax}) offers a valuable tool (e.g., Schefuß et al., 2005; Pagani et al., 2006; Huang et al., 2007; Niedermeyer et al., 2010; Tierney et al., 2011; Collins et al., 2013).

The relationship between δD_{wax} and climatic factors has been investigated by several approaches ranging from living plants (Sternberg, 1988; Sessions et al., 1999; Chikaraishi and Naraoka, 2003; Sachse et al., 2006, 2009; Smith and Freeman, 2006; Liu and Yang, 2008; Pedentchouk et al., 2008; Feakins and Sessions, 2010a,b), lake surface sediments (Huang et al., 2004; Sachse et al., 2004; Hou et al., 2008; Aichner et al., 2010; Polissar and Freeman, 2010; Garcin et al., 2012; Shanahan et al., 2013), marine surface sediments (Leider et al., 2013) to aerosols (Gao et al., 2014). The stable hydrogen isotopic composition of precipitation (δD_p) exerts the primary control on δD_{wax} signatures, though additional factors potentially have an influence on the apparent fractionation (ε) between δD_{wax} and δD_p (Sachse et al., 2012), which is defined as

$$\varepsilon = 1000*[(\delta D_{wax}+1000)/(\delta D_p+1000)-1].$$

Many studies have identified distinct ε variations for different plant types (Chikaraishi and Naraoka, 2003; Sachse et al., 2006, 2009, 2012; Smith and Freeman, 2006; Hou et al., 2007; Liu and Yang, 2008; Feakins and Sessions, 2010a,b; Gao et al., 2011; McInerney et al., 2011;

Tipple et al., 2013): Taken together, these studies indicate that grasses using the C_4 photosynthetic pathway have a more negative ε (mean of −136‰ for the *n*-C_{31} alkane) relative to C_3 trees (−110‰), while having a more positive ε compared to C_3 grasses (−151‰; Sachse et al., 2012). Considering plant life-forms, the least negative ε was observed for shrubs, especially long-lived ones and shrub-like trees, and a tendency to increasing fractionation by trees, forbs and grasses (Sachse et al., 2012). In addition to biosynthetic fractionation, climatic factors, such as relative humidity, have the potential to alter the isotopic signal by evaporative D-enrichment of soil-water (Smith and Freeman, 2006; McInerney et al., 2011) and leaf-water (Kahmen et al., 2013a,b). This is also related to differences in rooting depth, which result in the uptake of different source waters with varying degrees of evaporative D-enrichment (Sachse et al., 2012), including seasonal variations in the depth of water uptake (e.g., Asbjornsen et al., 2008). For instance, woody shrubs and trees are able to increase the depth of water uptake depending on water availability, whereas herbaceous plants are mainly limited to the upper 20 cm of the soil (Asbjornsen et al., 2008). According to Sachse et al. (2012), a larger ε in grasses (monocots) is mainly related to physiological/biosynthetic variations, while those in other classes (dicots such as trees, shrubs, herbs) are linked to a higher degree to climatic parameters affecting soil/leaf water D-enrichment. For instance, the temperature effect observed for isotopic fractionation is related to its influence on respiration and photosynthesis, potentially affecting the isotopic composition of intracellular water (Sachse et al., 2012). In more detail, isotopic variations between leaf water and its xylem water are driven by relative humidity, temperature and water vapor δD (Kahmen et al., 2008), while the latter is affected by the former two parameters (Sachse et al., 2010). It was found that climate-dependent isotopic modifications leading to leaf-water D-enrichment are strongest in arid regions (Kahmen et al., 2013a,b).

In addition to ε variations, clear differences in the timing of wax formation exist between monocots and dicots, thus integrating different δD_p ranges (Sachse et al., 2012). In contrast to deciduous leaf waxes, which are synthesized rather early during the growing season (Tipple et al., 2013), continuous wax formation in grasses provides a high potential for integrating environmental conditions of the entire growth phase (Smith and Freeman, 2006; Gao et al., 2012). However, such differences should be limited in regions with a generally short growing season, e.g., the West African Sahel. This means that the δD_{wax} signature incorporates a combination of biosynthetic fractionation, source-water δD and the local environmental conditions.

With regard to regional differences, recent observations are necessary to calibrate proxies for reliable inferences of past environmental changes on a regional scale. The mapping of marine surface sediment properties and its comparison with modern environmental conditions form a necessary baseline for further down-core interpretations. In this study, we focus on West Africa (**Fig. 5.1**), a region of extreme environmental differences (see next section) and hence, a suitable study area for the assessment of the hydrologic information provided by

marine δD_{wax} records. So far, coretop mapping of the stable carbon isotopic composition of plant waxes ($\delta^{13}C_{wax}$) has been accomplished in this area and revealed a clear link to latitudinal vegetation zones in West Africa (Huang et al., 2000). This finding is also in line with pollen data from marine surface sediments (Dupont and Agwu, 1991) and the $\delta^{13}C_{wax}$ signature of aerosols (Simoneit, 1997; Schefuß et al., 2003a). Thus, in order to assign the marine sedimentary hydrologic signal (δD_{wax}) to continental sources, we compare our $\delta^{13}C_{wax}$ data with previous results and the West African environmental setting. For the latter, we calculated annual means of climatic parameters within the inferred catchments, including precipitation amount and corresponding δD_p signature, as well as mean air temperature and water vapor pressure. This calibration study aims for establishing a δD_{wax}–δD_p relationship, in order to improve our understanding of the environmental information captured in the δD_{wax} signal in this particular region, which will ultimately support its application in the paleoclimatic context.

5.3 Study Area

Precipitation variability in West Africa follows a distinct pattern: North of the Sahara, the wet season occurs during winter, which also accounts for most of the major rainfall events in the central Sahara (Nicholson, 2000). South of the Sahara, the latitudinal/seasonal migration of the tropical rain belt exerts the dominant influence on West African climate, with highest precipitation amounts at the equator decreasing towards higher latitudes (Nicholson, 2009). This causes the high seasonality in the Sahel, limiting the rainy season to boreal summer (July to September) when the tropical rain belt migrates northward reaching its northernmost position at ~20°N in August (Nicholson, 2009). The Sahel is thus most susceptible to climate changes and frequently affected by periods of severe drought (e.g., Heinrigs and Perret, 2009). Moisture sources of tropical precipitation in West Africa are the Gulf of Guinea and local water recycling through continental evapotranspiration (Gong and Eltahir, 1996; Nicholson, 2009). The

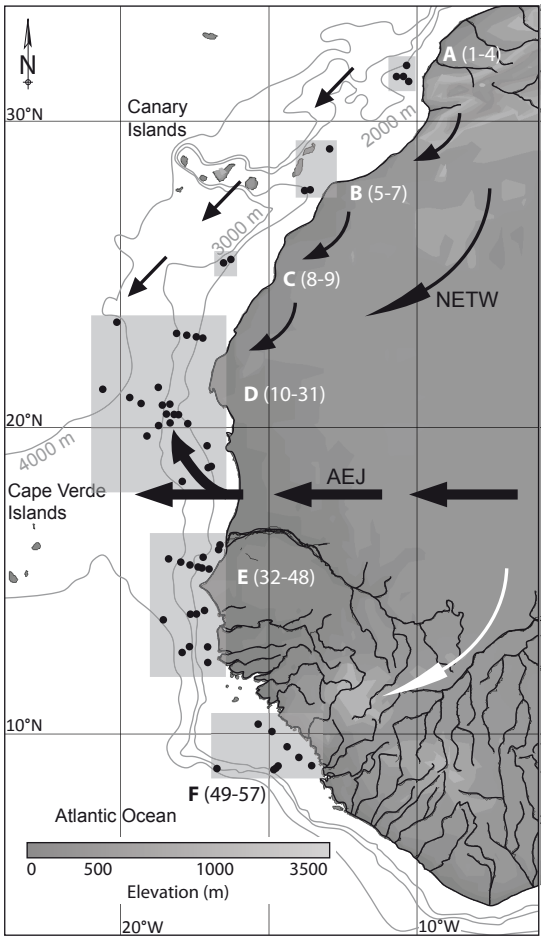

Fig. 5.1: Locations of marine surface sediment samples (black dots) used in this study. Samples were locally grouped (grey areas A-F) to facilitate the comparison with environmental factors. Topographic features of West Africa including major river and wind systems, as well as bathymetry of the adjacent NE Atlantic are indicated. The thickness of the arrows marks the different altitudes of the African Easterly Jet (AEJ; > 3000 m) and the North-East Trade Winds (NETW; < 1000 m).

dominant control on tropical δD_p is the amount effect leading to a negative correlation between precipitation amounts and δD_p values, while other effects related to temperature, altitude and distance to the moisture source exert further influences on δD_p (Dansgaard, 1964; Rozanski et al., 1993; Worden et al., 2007; Risi et al., 2008a,b).

This precipitation regime is reflected in the distribution and composition of the vegetation (White, 1983): North of the Sahara, vegetation can be generally divided into forests and steppes. Forests contain, among others, *Quercus* (oak tree), *Pinus* (pine tree) and *Cedrus* (Cedar); steppes contain, for instance, *Stipa* (a C_3 grass), *Ephedra* and *Artemisia* (shrubs). Species of *Artemisia* are also abundant at higher altitudes. The steppe (semi-desert grassland and shrubland) forms the transition to the Sahara desert in the south. The sparse desert vegetation consists of mostly C_4 plants (e.g., *Amaranthaceae*) and rarely CAM (Crassulacean Acid Metabolism) plants. The Sahel constitutes the southern transition zone to the desert, and can be divided into a northern part consisting of semi-desert grass-/shrubland and a southern part comprising *Acacia* wooded grassland and deciduous bushland. In contrast to biomes north of the Sahara (C_3 plants), sub-Saharan tropical grass species are almost exclusively of C_4-type, which are well adapted to warm and arid conditions (e.g., Ehleringer et al., 1997). Towards the equator, C_3 plant contributions increase in the Sudanian and Guinean vegetation belts and maximize in the tropical rainforest close to the Gulf of Guinea. Along the coast, mangroves occur in the vicinity of rivers.

Transport of terrigenous material in West Africa is mainly related to the atmospheric circulation: Low-altitude North-East Trade Winds (NETW) dominate during boreal winter carrying dust southwestwards, whereas at higher altitudes, the African Easterly Jet (AEJ) is strongest during boreal summer, carrying dust from the southern Sahara and Sahel westward (e.g., Pye, 1987; Chiapello et al., 1995, 1997; Prospero, 1996). These two wind systems are responsible for the majority of plant waxes deposited in the adjacent ocean (e.g., Simoneit et al., 1977; Gagosian et al., 1981; Huang et al., 2000; Schefuß et al., 2003a). In coastal areas, fluvial transport is locally important, such as off Morocco (Holz et al., 2004), Senegal and the Gulf of Guinea (Huang et al., 2000).

However, several lines of evidence indicate that dust deposition in the NE Atlantic offshore West Africa is rather dominated by the NETW, compared to the AEJ's long distance transport (Chiapello et al., 1995, 1997; Ratmeyer et al., 1999a,b; Stuut et al., 2005). A common feature is the NE-SW-trend in the distribution of Sr-Nd-isotopes in marine surface sediments (Grousset et al., 1998) and atmospheric dust samples (Skonieczny et al., 2011), as well as in grain size (Stuut et al., 2005) and clay mineral (Lange, 1982) assemblages. Similar Sr-Nd-isotopes in dust and marine sediments even suggest that the terrigenous fraction is predominantly derived from major dust storms (Skonieczny et al., 2011). During such events, the wind trajectories and associated dust sources may shift significantly, thus documenting its potential to integrate the signals from large catchment areas (Skonieczny et al., 2011). The Sahel is a major dust source for the supply of most terrigenous material to the NE Atlantic,

Table 1: Compilation of coretop data used in this study. Locations are indicated in **Fig. 5.1**.

Area	Loc.	Station (GeoB)	Lat. (°N)	Lon. (°E)	Depth (mbsl)	Distance to coast (km)	n-C_{27-35} (µg/g)	CPI_{25-33}	ACL_{25-35}	$\delta^{13}C$ (‰ VPDB)								δD (‰ VSMOW)							
										n-C_{29}	SD	n-C_{31}	SD	n-C_{33}	SD	WMA	SD	n-C_{29}	SD	n-C_{31}	SD	n-C_{33}	SD	WMA	SD
A	1	8603-2	31.183	-10.453	500	60	0.35	5.1	30.4	-31.5	0.3	-31.3	0.1	-31.1	0.1	-31.3	0.2	-136	3	-148	2	-132	2	-140	2
A	2	8606-2	31.003	-10.742	1227	90	0.52	4.9	30.0	-31.5	0.2	-31.2	0.1	-30.7	0.0	-31.2	0.1	-132	4	-148	4	-130	0	-139	3
A	3	8604-3	30.957	-10.522	885	70	0.58	4.3	30.1	-31.7	0.1	-31.1	0.2	-31.0	0.1	-31.3	0.1	-129	2	-147	3	-126	1	-136	2
A	4	8601-1	30.848	-10.268	924	40	0.67	4.6	29.9	-31.5	0.2	-31.5	0.1	-31.9	0.1	-31.6	0.1	-130	2	-145	3	-128	1	-136	2
B	5	8608-4	28.800	-12.983	975	110	0.48	4.7	30.4	-28.8	0.0	-28.8	0.1	-27.9	0.0	-28.6	0.1	-134	3	-141	1	-132	0	-137	1
B	6	8613-7	27.535	-13.737	1078	50	0.50	3.2	29.8	-29.0	0.3	-28.7	0.1	-28.5	0.5	-28.8	0.2	-125	0	-137	1			-132	1
B	7	8614-2	27.535	-13.850	1440	60	0.25	2.1	28.6	-28.3	0.8	-28.8	0.3	-29.9	0.3	-28.7	0.6								
C	8	8619-2	25.448	-16.345	1338	170	0.09	3.1	28.9	-28.2	0.3	-26.9	0.0	-27.7	0.4	-27.6	0.2	-118	5	-135	1			-126	3
C	9	8620-2	25.360	-16.538	1864	170	0.19	3.8	29.9	-27.9	0.2	-27.1	0.1	-27.2	0.3	-27.4	0.1	-127	2	-139	0	-128	3	-133	1
D	10	8622-6	23.510	-20.205	3956	400	0.08	3.1	28.7	-27.4	0.3	-26.3	0.2	-26.5	0.4	-26.8	0.3	-118	0	-135	2			-126	1
D	11	8627-2	23.200	-18.170	2668	200	0.25	4.8	29.7	-26.8	0.1	-25.8	0.2	-25.2	0.2	-26.1	0.2	-135	2	-144	1	-134	3	-139	2
D	12	8626-2	23.142	-17.840	2255	170	0.08	3.0	28.8	-27.0	0.6	-26.4	0.0	-26.2	1.1	-26.7	0.4								
D	13	8625-1	23.078	-17.503	1294	130	0.33	3.7	30.1	-27.0	0.2	-26.0	0.3	-26.3	0.4	-26.4	0.3	-128	2	-144	3	-137	3	-137	3
D	14	8624-1	23.040	-17.293	864	110	0.13	1.9	28.9	-27.6	0.1	-26.2	0.4	-25.0	0.4	-26.6	0.3								
D	15	13611-3	21.333	-18.842	3073	195	0.37	6.0	29.8	-26.8	0.1	-25.6	0.3	-25.4	0.1	-26.0	0.2	-136	1	-141	1	-125	3	-137	1
D	16	13616-6	21.270	-20.812	4167	400	0.21	6.5	29.6	-26.8	0.6	-25.6	0.7	-24.9	0.5	-26.0	0.6								
D	17	13615-4	21.000	-19.833	3702	300	0.17	5.6	29.6	-26.9	0.2	-25.7	0.2	-25.2	0.3	-26.1	0.2								
D	18	7919-2	20.942	-19.387	3429	250	0.45	4.4	30.9	-26.5	0.0	-25.7	0.5	-24.8	0.4	-25.9	0.3	-139	3	-142	1	-130	2	-139	2
D	19	8630-8	20.818	-17.972	1327	100	0.09	2.1	29.0	-27.5	0.4	-26.1	1.0	-25.1	0.5	-26.6	0.7								
D	20	13612-3	20.752	-18.699	2691	170	0.51	4.8	30.0	-27.3	0.0	-25.6	0.1	-25.5	0.8	-26.2	0.2	-133	1	-135	2			-134	2
D	21	7920-3	20.750	-18.583	2278	150	0.78	2.7	30.7	-26.7	0.1	-25.8	0.1	-26.2	0.1	-26.2	0.1	-128	3	-135	0	-124	2	-130	2
D	22	7923-1	20.740	-18.178	1516	110	0.40	3.5	30.5	-27.3	0.2	-26.4	0.3	-25.6	0.1	-26.5	0.2	-134	4	-138	1	-134	3	-136	2
D	23	7922-3	20.667	-18.262	1289	130	0.41	2.7	32.6	-26.2	0.5	-25.0	0.2	-25.7	0.8	-25.5	0.4	-134	1	-144	2	-140	5	-140	3
D	24	8631-8	20.467	-17.817	500	100	0.13	3.0	29.8	-26.4	0.2	-24.7	0.1	-23.6	0.4	-25.0	0.2	-129	2	-143	2	-148	3	-140	2
D	25	7926-3	20.213	-18.452	2500	170	0.84	4.0	30.3	-26.5	0.2	-25.4	0.0	-24.9	0.2	-25.7	0.1	-140	5	-145	0	-135	0	-141	2
D	26	13610-2	20.083	-18.834	2891	200	0.47	5.8	30.1	-27.4	0.1	-25.6	0.0	-25.8	0.7	-26.3	0.1	-137	0	-142	1	-130	1	-138	1
D	27	7927-1	19.937	-19.152	3128	270	0.84	4.7	31.6	-26.5	0.3	-25.0	0.0	-24.9	0.5	-25.5	0.2	-139	1	-141	2	-139	2	-140	2
D	28	13609-4	19.406	-17.139	918	70	0.27	6.1	30.1	-26.8	0.1	-24.5	0.1	-24.2	0.2	-25.2	0.1	-130	1	-142	2	-142	4	-138	2
D	29	7928-3	19.100	-17.047	1348	70	0.79	3.6	32.1	-26.4	0.1	-24.5	0.0	-24.9	0.2	-25.2	0.1	-140	2	-141	1	-129	4	-138	2
D	30	7932-2	19.002	-17.283	1964	90	0.47	4.5	31.4	-25.9	0.5	-24.6	0.1	-24.0	0.4	-24.9	0.3	-141	2	-143	1	-143	4	-142	2
D	31	7936-2	18.592	-18.037	2663	190	0.93	4.7	30.3	-26.4	0.1	-25.4	0.0	-24.8	0.1	-25.6	0.1	-145	1	-146	0	-143	1	-145	1
E	32	9503-3	16.066	-16.650	49	15	0.30	5.0	30.4	-27.1	0.3	-25.7	0.1	-23.4	0.4	-25.6	0.3	-146	0	-150	1	-146	2	-148	1
E	33	13606-2	15.960	-16.764	81	25	0.60	5.5	30.3	-28.3	0.2	-26.0	0.1	-24.4	0.0	-26.4	0.1	-145	0	-154	2	-149	2	-150	1
E	34	13604-2	15.669	-17.275	1051	60	0.78	4.6	30.4	-27.2	0.4	-26.0	0.0	-24.4	0.2	-26.0	0.2	-145	0	-150	2	-144	2	-147	1
E	35	9506-3	15.608	-18.350	2964	140	1.45	5.5	30.0	-26.7	0.0	-25.3	0.1	-24.4	0.1	-25.7	0.1	-142	0	-148	0	-148	1	-146	0
E	36	9508-4	15.500	-17.947	2385	100	1.57	5.8	30.1	-27.0	0.3	-25.4	0.0	-24.5	0.6	-25.8	0.2								
E	37	9510-3	15.417	-17.653	1567	80	1.24	4.8	30.2	-26.9	0.1	-25.7	0.2	-24.7	0.1	-25.9	0.1	-147	2	-148	3	-143	1	-147	2
E	38	9512-4	15.337	-17.367	787	50	0.90	4.7	30.3	-26.9	0.2	-25.7	0.0	-24.0	0.0	-25.7	0.1	-147	1	-154	5	-152	4	-151	4
E	39	9513-5	15.318	-17.295	498	40	0.48	4.5	30.5	-27.3	0.2	-25.6	0.1	-24.2	0.2	-25.7	0.1	-142	2	-154	1	-153	2	-150	2
E	40	9515-2	15.273	-17.045	102	15	0.77	5.3	30.6	-27.4	0.5	-25.9	0.0	-24.1	0.1	-25.9	0.2	-149	5	-153	5	-160	2	-153	4
E	41	9547-2	13.952	-17.172	38	45	0.05	3.1	30.5	-29.4	0.6	-26.8	0.2	-26.0	0.4	-27.4	0.4	-148	2	-144	2	-148	2	-146	2
E	42	9522-2	13.855	-17.454	222	80	0.16	4.0	30.3	-28.3	0.2	-26.7	0.1	-25.3	0.6	-26.9	0.3	-149	0	-150	2	-144	2	-148	1
E	43	9520-4	13.830	-17.591	1102	90	0.73	5.0	30.3	-27.5	0.0	-26.4	0.1	-24.8	0.2	-26.4	0.1	-148	3	-150	2	-150	5	-149	3
E	44	9516-4	13.674	-18.419	3443	180	2.02	6.2	30.2	-27.0	0.0	-25.6	0.0	-24.3	0.1	-25.8	0.0	-146	3	-153	1	-156	1	-151	1
E	45	9545-1	12.848	-17.076	18	35	0.01	2.4	28.9	-29.8	0.8	-28.2	0.3	-27.5	0.1	-28.8	0.5	-157	2						
E	46	9524-3	12.846	-17.627	75	100	0.05	4.4	30.5	-29.1	0.5	-27.9	0.2	-27.6	0.4	-28.3	0.3	-143	3	-148	2	-158	2	-148	2
E	47	13601-3	12.434	-18.005	1200	130	1.48	4.2	30.3	-27.9	0.1	-26.3	0.1	-24.8	0.2	-26.6	0.1	-147	1	-148	0	-144	0	-147	0
E	48	9544-1	12.375	-17.068	21	35	0.04	3.9	29.8	-30.4	1.0	-29.3	1.0	-27.6	0.0	-29.4	0.8								

Table 1: *continued*

Area	Loc.	Station (GeoB)	Lat. (°N)	Lon. (°E)	Depth (mbsl)	Distance to coast (km)	n-C_{27-35} (µg/g)	CPI_{25-33}	ACL_{25-35}	$\delta^{13}C$ (‰ VPDB)								δD (‰ VSMOW)							
										n-C_{29}	SD	n-C_{31}	SD	n-C_{33}	SD	WMA	SD	n-C_{29}	SD	n-C_{31}	SD	n-C_{33}	SD	WMA	SD
F	49	9543-1	10.397	-15.525	27	80	0.02	1.6	29.6	-30.7	0.3	-28.4	0.1	-27.1	0.3	-29.2	0.2								
F	50	9542-1	10.142	-15.030	25	60	0.01	2.5	30.0	-30.9	0.9	-29.0	0.1	-28.4	0.2	-29.7	0.5								
F	51	9541-1	9.658	-14.573	33	60	0.02	3.4	30.3	-30.0	0.3	-28.8	0.0	-27.2	0.5	-28.9	0.3	-138	4	-146	3			-142	3
F	52	9540-1	9.294	-14.164	31	60	0.03	2.0	30.4	-30.7	0.4	-28.8	0.0	-27.5	0.3	-29.1	0.2								
F	53	9539-1	9.019	-13.733	22	50	0.07	3.0	29.9	-30.2	0.9	-29.0	0.1	-27.1	0.3	-29.1	0.4	-136	3	-143	1	-157	2	-143	2
F	54	9532-1	8.948	-14.889	301	150	0.53	4.3	29.7	-31.6	0.1	-31.0	0.1	-28.1	0.4	-30.9	0.1	-139	1	-141	3	-144	3	-141	2
F	55	9531-2	8.941	-16.904	2288	300	1.99	4.6	30.1	-28.3	0.2	-26.7	0.0	-25.0	0.3	-27.1	0.2	-146	0	-150	1	-146	0	-148	0
F	56	9533-3	8.926	-14.911	384	150	0.78	4.5	29.6	-31.6	0.0	-31.1	0.0	-28.3	0.5	-30.9	0.1	-144	0	-144	1	-146	4	-144	1
F	57	9534-4	8.901	-14.936	493	160	0.95	2.4	29.6	-31.2	0.1	-30.6	0.0	-28.4	0.3	-30.6	0.1	-139	5	-140	0			-139	3

mbsl, meters below sea level; CPI, carbon preverence index; ACL, average chain length; SD, standard deviation, WMA, weighted mean average of the n-C_{29}, n-C_{31} and n-C_{33} alkanes.
Note: Sample locations 18, 23, 27, 29, 30 are taken from Kuechler et al. (2013).

being mainly active during December and January (Chiapello et al., 1995, 1997). Likewise, this means that plant-wax export is mostly restricted to the winter season. Though the timing of wax formation differs greatly among plants (see above), we may assume that a catchment-integrated signal recorded by sedimentary plant waxes generally reflects the environmental conditions during the growing season (Sachse et al., 2012) or integrate an average annual signal, considering the higher production and regeneration of waxes under stress (e.g., Shepherd and Griffith, 2006; Gao et al., 2012).

The main ocean surface currents in the study area are the Canary Current, Guinea Current, North Equatorial Current and North Equatorial Counter Current (e.g., Sarnthein et al., 1982; not shown). As part of the subtropical North Atlantic Gyre, the wind-driven Canary Current flows southward along the West African continental margin and merges with the North Equatorial Current. Coastal upwelling is a prominent feature in this area, induced by NETW intensity (e.g., Mittelstaedt, 1991). The North Equatorial Counter Current flows eastward south of 10°N. Despite of the potential displacement of pollen and dust by ocean currents, the latitudinal distribution of vegetation is well reflected in the pollen assemblages (Hooghiemstra and Agwu, 1986; Dupont and Agwu, 1991; Hooghiemstra et al., 2006) and plant-wax $\delta^{13}C$ (Huang et al., 2000) of marine surface sediments and can thus be ruled out as a major effect. This is further supported by time-series data of sediment traps in this area, indicating a significant correlation between organic carbon and lithogenic particle fluxes, as well as a rapid and almost undisturbed sedimentation of particulate matter (Ratmeyer et al., 1999a).

5.4 Materials and methods

5.4.1 Sample specifications

This study uses 57 marine surface sediment samples (0-1 cm), spanning a N-S-transect from 31°N (Morocco) to 9°N (Guinea) along the West African continental margin from various water depths (18-4167 m) and distances (15-400 km) to the coast (**Table 1**; **Fig. 5.1**). Samples were retrieved during cruises M53/1 (2002), M58/2 (2003), M65/1 (2005) and MSM11/2 (2009) of the German research vessels Meteor (M) and Maria S. Merian (MSM), and recovered by multicorer to preserve the original sediment surface.

5.4.2 Lipid extraction and analyses

Samples were dried, ground and an internal standard (IS; squalane) was added before extraction. Lipid extraction was performed with a DIONEX Accelerated Solvent Extractor (ASE 200) using a mixture of dichloromethane:methanol (DCM:MeOH, 9:1) under controlled pressure (1,000 psi) and temperature (100°C). The resultant total lipid extracts were concentrated via rotary evaporation and subsequently saponified with 6% KOH in MeOH at 85°C for 2 h. Neutral compounds were then isolated with hexane and separated by column chromatography with silica gel (60 mesh). Further column chromatography with $AgNO_3$-coated silica gel was used to purify the saturated hydrocarbons by removing unsaturated compounds. Identification and quantification of *n*-alkanes was carried out by gas chromatography/flame ionization detection (GC-FID) using a reference mixture with known *n*-alkane concentrations as external standard. The mean precision for *n*-alkane quantification is 0.02 µg g^{-1}, based on the mean accuracy (3%) of the external standard.
The carbon preference index (CPI) of long-chain *n*-alkanes is based on

$$CPI = 0.5*[(X_i + X_{i+2} + ... + X_n)/(X_{i-1} + X_{i+1} + ... + X_{n-1})] + 0.5*[(X_i + X_{i+2} + ... + X_n)/(X_{i+1} + X_{i+3} ... + X_{n+1})]$$

with i = 25 and n = 33, indicating the carbon number of *n*-alkanes (Kolattukudy, 1976).
The average chain-length (ACL) is based on

$$ACL = \sum(i*X)/\sum X_i$$

with X for abundance and i for the range of carbon numbers between 25 and 35 of *n*-alkanes (Poynter et al., 1989).

5.4.3 Plant-wax-specific stable hydrogen and carbon isotopes

Compound-specific δD analyses were conducted with a Thermo Trace GC coupled to a Thermo Fisher Scientific MAT 253 irm-MS via a pyrolysis furnace operated at 1,420°C. All

measurements are calibrated against H_2 reference gas with known isotopic composition and the H^{3+} factor was monitored daily (value of 6.1; 6.8 for coretops from Kuechler et al., 2013). δD values are reported in permil [‰] relative to the Vienna Standard Mean Ocean Water (VSMOW) standard. An external standard mixture with known δD values of 15 *n*-alkanes was analyzed repeatedly with the samples, and yielded a precision (1σ) and accuracy of 3‰ and 1‰, respectively (n=57). In addition, squalane (IS) yielded a precision (1σ) of 3‰ (n=99). The mean standard deviation (1σ) of replicates for the *n*-C_{29}, *n*-C_{31} and *n*-C_{33} alkane is 2‰.

$\delta^{13}C$ values of *n*-alkanes were measured using a Thermo Trace GC coupled to a Finnigan MAT 252 irm-MS via a modified Finnigan GC/C III combustion interface operated at 1,000°C. $\delta^{13}C$ values were calibrated against an external reference gas (CO_2) with known isotopic composition, and are reported in permil [‰] relative to the Vienna PeeDee Belemnite (VPDB) standard. The external *n*-alkane standard yielded a precision and accuracy of 0.2‰ and -0.1‰, respectively (n=43). Duplicate measurements yielded a standard deviation (1σ) for the *n*-C_{29}, *n*-C_{31} and *n*-C_{33} alkane of 0.2-0.3‰ and for squalane (IS) of 0.1‰ (n=105).

In order to facilitate the comparison with the conditions on land, the coretops were regionally grouped and the plant-wax data fused into concentration-weighted areal means (**Table 2**).

5.4.4 Climatic parameters

Continental source areas of marine sedimentary plant waxes were selected according to the latitudinal extent of regionally grouped coretops and span a distance of approximately 200 km inland from the coast. Annual values (averaged over 1961-1990) for precipitation amount, mean air temperature (MAT) and water vapor pressure were taken from the CRU TS 3.22 dataset (Harris et al., 2014; New et al., 1999). Catchment mean δD values for annual precipitation (δD_p) were retrieved from the δD_p dataset of Bowen and Revenaugh (2003). These estimates are also precipitation amount-weighted (Bowen and Revenaugh, 2003) by

Table 2: Weighted areal mean values for plant-wax-specific data.

Area	*n*-C_{27-35}	SE	CPI_{25-33}	SE	ACL_{25-35}	SE	$\delta^{13}C$ (‰ VPDB)								δD (‰ VSMOW)							
	(µg/g)						*n*-C_{29}	SE	*n*-C_{31}	SE	*n*-C_{33}	SE	WMA	SE	*n*-C_{29}	SE	*n*-C_{31}	SE	*n*-C_{33}	SE	WMA	SE
A	0.53	0.07	4.7	0.2	30.1	0.1	-31.5	0.2	-31.3	0.2	-31.2	0.3	-31.3	0.3	-131	3	-147	3	-128	2	-138	4
B	0.41	0.08	3.5	0.8	29.8	0.5	-28.8	0.5	-28.8	0.2	-28.4	0.7	-28.7	0.6	-129	5	-139	2	-132	0	-134	3
C	0.14	0.05	3.6	0.3	29.6	0.5	-28.0	0.3	-27.0	0.1	-27.3	0.4	-27.5	0.4	-124	6	-138	2	-128	3	-130	6
D	0.42	0.06	4.2	0.3	30.7	0.2	-26.6	0.3	-25.4	0.4	-25.1	0.5	-25.9	0.7	-137	3	-138	2	-136	3	-138	4
E	0.74	0.15	5.2	0.2	30.3	0.1	-27.3	0.5	-25.9	0.4	-24.4	0.4	-26.6	0.6	-146	2	-146	3	-151	3	-149	4
F	0.49	0.22	4	0.4	29.9	0.1	-30.5	0.6	-29.4	0.5	-27.0	0.5	-29.5	0.7	-143	3	-145	2	-146	4	-143	4

CPI, carbon preference index; ACL, average chain-length; SE, standard error; WMA, weighted mean average of the *n*-C_{29} , *n*-C_{31} and *n*-C_{33} alkanes.

Table 3: Compilation of climatic parameters (annual catchment means), including precipitation amount and corresponding δD values (δD_p), mean air temperatures (MAT) and water vapor pressure.

N-S extent	W-E extent	Precipitation (mm/a)[a]	δD_p (‰ VSMOW)[b]	MAT (°C)[a]	VP (hPa)[a]
30-32°N	West coast-8°W	277	-27	16.9	12.9
27-29°N	West coast-9°W	79	-15	21.2	14.8
25-26°N	West coast-13°W	30	-10	22.6	15.6
18-24°N	West coast-15°W	44	-11	24.4	15.5
12-16°N	West coast-15°W	801	-21	26.9	20.8
8.5-11°N	West coast-12°W	2287	-25	26.1	24.2

δD_p, δD of precipitation; MAT, mean air temperature; VP, water vapor pressure.
[a] Obtained from the CRU TS3.22 dataset (Harris et al., 2014; New et al., 1999).
[b] Obtained from the water isotopes dataset (Bowen and Revenaugh, 2003).

using the method described in Bowen and Wilkinson (2002). It is possible that gridded δD_p values do not correspond to the real isotopic signature of precipitation due to the following reasons: (1) The uneven distribution and low number of GNIP-stations (GNIP = Global Network of Isotopes in Precipitation), particularly in West Africa (IAEA/WMO, 2014), results in the interpolation of δD_p values over huge areas. (2) Temporally uneven sampling at different stations may create artifacts. Due to the lack of alternative data, this approach constitutes the best estimate available for our study. A compilation of these parameters is given in **Table 3**.

5.5 Results and discussion

5.5.1 Sedimentary concentrations and distributions of long-chain n-alkanes

Sedimentary *n*-alkanes are dominated by long-chain *n*-C_{27-35} homologs, with concentrations ranging from 0.01 to 2.02 µg g^{-1} dry weight. The most abundant compounds are the *n*-C_{29}, *n*-C_{31} and *n*-C_{33} alkanes, reflected in ACL values between 28.6 and 32.6 (mean 30.1; **Table 1**). CPI values range between 1.6 and 6.5 (mean of 4.1), reflecting the general odd-over-even carbon number predominance of higher plants (Eglinton and Hamilton, 1967). However, evaluating plant contributions with the CPI as a strict threshold value seems ambiguous, since modern plants cover a huge range of CPI values (Bush and McInerney, 2013). Considering our study area, previous dust analyses exhibit the lowest CPI values adjacent to arid regions, related to low plant-wax concentrations and potential contributions from other sources such as fossil fuel or marine lipids (Eglinton et al., 2002; Schefuß et al., 2003a). Remarkably, these studies found no influence on major (odd-numbered) homologs and associated isotopic signatures by these potential admixtures. In our study, low CPI values are also linked to lower plant-wax concentrations and vice versa, reflected in a significant correlation between both data sets (r = 0.84; p = 0.04; **Table 4**). Thus, CPI values of samples with low plant-wax

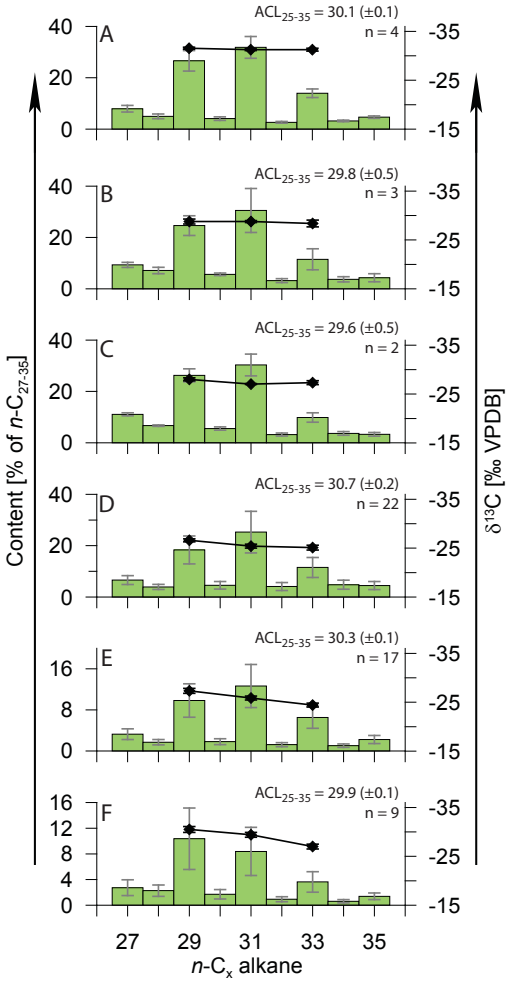

Fig. 5.2: Areal means of *n*-alkane distribution (% of *n*-C_{27-35} alkane content) and corresponding $\delta^{13}C$ values for major long-chain homologs. Error bars display the standard errors. In addition, the average chain-length (ACL) and their standard errors (in brackets) are indicated, as well as number of samples (n).

concentrations might be compromised. However, considering the robust link between $\delta^{13}C_{wax}$ and vegetation (Simoneit, 1997; Huang et al., 2000; Eglinton et al., 2002; Schefuß et al., 2003a), we are confident that δD_{wax} values are not compromised by other sources and reflect the hydrologic signal of the contemporary vegetation.

The *n*-C_{31} alkane is the dominant homolog throughout the transect, except for the southernmost area (F) with plant-wax distributions peaking at the *n*-C_{29} alkane (**Fig. 5.2**). This is in agreement with the general observation that (1) plants from the northern and southern transition zones to the Sahara, including grasses (*Poaceae*), shrubs and herbs (e.g., *Artemisia*), favor the production of *n*-alkanes with longer chain-length (Rommerskirchen et al., 2006a,b; Vogts et al., 2009; Garcin et al., 2014), and (2) that most of these plants are angiosperms (like *Poaceae*, *Artemisia*, *Quercus* and *Acacia*), which produce considerably higher amounts of *n*-alkanes within their wax coatings than gymnosperms (like *Pinus* and *Ephedra*; Diefendorf et al., 2011; Bush and McInerney, 2013), thus dominating the distribution patterns of areas A-E. According to their protective function, plant-wax production increases when relative humidity decreases, comparable to an accelerated regeneration of abraded waxes induced by environmental stress (Shepherd & Griffith, 2006; Pedentchouk et al., 2008; Sachse et al., 2009). Such conditions prevail in (semi-)arid regions of the steppe in the north (with C_3 grasses) or the Sahel in the south (with C_4 grasses). Additional potential source areas are high-altitude regions (e.g., the Atlas Mountains), where plants experience a combination of dehydration and low temperatures (Shepherd & Griffith, 2006). For the southernmost area (F), abundant and diverse "non-grassy" vegetation of the tropical rain forests may account for the dominant occurrence of the *n*-C_{29} alkane (Vogts et al., 2009).

5.5.2 Sedimentary $\delta^{13}C_{wax}$ and continental vegetation

The $\delta^{13}C_{wax}$ signature is mainly defined by two principal pathways of photosynthesis, with C_3 plants being more depleted, on average, than C_4 plants (e.g., Collister et al., 1994). Overall, $\delta^{13}C_{wax}$ values in C_3 plants cover a range from −32‰ to −39‰ and in C_4 plants between −18‰ and −25‰ (Rieley et al., 1991, 1993; Collister et al., 1994; Rommerskirchen et al., 2006a,b; Vogts et al., 2009). However, the large $\delta^{13}C_{wax}$ variability observed for modern plants accounts for a huge uncertainty in C_3/C_4 estimates (Castañeda et al., 2009; Diefendorf et al., 2010). For instance, calculating C_3/C_4 plant contributions from $\delta^{13}C_{wax}$ values in area A off Morocco (with only C_3 plants) yields unrealistic estimates of 24%, 29% and 41% C_4 plants for the *n*-C_{29}, *n*-C_{31} and *n*-C_{33} alkanes, respectively. Therefore, we limit our interpretations to qualitative estimates by comparing $\delta^{13}C_{wax}$ values to previously published pollen (Dupont and Agwu, 1991), plant-wax (Simoneit, 1997; Huang et al., 2000; Schefuß et al., 2003a) and climatic (Harris et al., 2014; New et al., 1999) data.The $\delta^{13}C_{wax}$ records obtained from the *n*-C_{29}, *n*-C_{31} and *n*-C_{33} alkanes are significantly correlated with each other (**Table 4**). The largest range of $\delta^{13}C_{wax}$ values for single samples is found for the *n*-C_{33} alkane ($\delta^{13}C_{33}$ between −31.9‰ and −23.4‰; **Table 1**). Areal means show slightly smaller ranges,

e.g., for $\delta^{13}C_{33}$ between −31.2‰ and −24.4‰, due to averaging (**Table 2**). In general, most depleted values occur off Morocco and the coast of Guinea, while the most enriched values were detected at the latitude of the Sahel (**Fig. 5.3**), in line with previous works including aerosols (Simoneit, 1997; Schefuß et al., 2003a), marine sedimentary $\delta^{13}C_{wax}$ (Huang et al., 2000) and pollen assemblages (Hooghiemstra and Agwu, 1986; Dupont and Agwu, 1991). Our results agree well with the previous $\delta^{13}C_{wax}$ mapping in this area (Huang et al., 2000) with only minor differences in the range of ±0.5‰ for the *n*-C_{29} alkane (**Fig. 5.3**). Typical pollen source indicators for the Mediterranean catchment comprise among others *Quercus* (oak tree), *Pinus* (pine tree), *Artemisia* (shrub, herb) and *Ephedra* (shrub) species. Pollen from the latter three taxa is used as so-called NETW indicators (**Fig. 5.3**), since NETW are its dominant transport agents (Hooghiemstra et al., 1987). *Poaceae* (grasses) show maximum pollen percentages at the latitude of the Sahel, in accord with highest grass coverage (in this case of the C_4-type) on the continent (Dupont and Agwu, 1991). For the tropics, we chose *Elaeis guineensis* (oil palm) pollen as a representative for rain forest vegetation (Dupont and Agwu, 1991). All these proxies reflect a consistent picture of the modern vegetation cover in West Africa, with major occurrences of C_3 plants in the northern and southern parts of the transect and a maximum of C_4 plants off the Sahel. Towards the southern end of the transect (areas D-F), the increasing offsets between the single long-chain *n*-alkanes is reflecting a

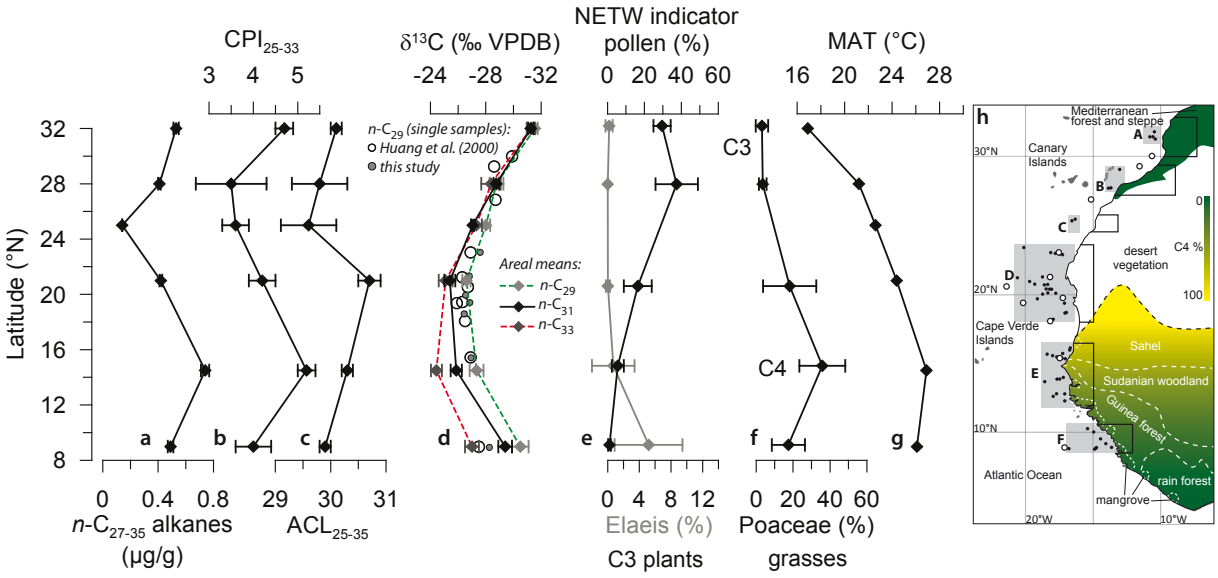

Fig. 5.3: West African vegetation. Concentration-weighted areal means of the (a) *n*-C_{27-35} alkane concentrations, (b) carbon preference index (CPI), (c) average chain-length (ACL), (d) $\delta^{13}C$ values for the *n*-C_{29}, *n*-C_{31} and *n*-C_{33} alkanes (in ‰ VPDB). Black circles denote $\delta^{13}C$ values of *n*-C_{29} alkanes of single coretops within the transect reported by Huang et al. (2000). From our data set, the closest sample was chosen for comparison (grey dots) and reveals a good reproducibility with a maximum difference of 0.7‰ between our and previously published results. (e) Areal means for NETW indicator pollen and *Elaeis* (oil palms), representative for C_3 plants in the northern and southern biomes, respectively, as well as (f) *Poaceae* (grasses), tracking the C_4 grass maximum off the Sahel (Dupont and Agwu, 1991). (g) Annual mean air temperature (MAT) based on the CRU TS3.22 dataset (Harris et al., 2014; New et al., 1999). (h) Vegetation zones and C_4 percentages simplified after White (1983). Grey boxes (A-F) indicate groups of coretops. Black boxes indicate assumed catchments for which climatic parameters were calculated.

mixed C_3/C_4 vegetation with higher contributions of C_4 plants in longer-chained *n*-alkanes (Rommerskirchen et al., 2006a,b).

In more detail, the single coretops in areas E and F harbor more information than the weighted areal means reveal. A clear N-S and E-W trend is apparent in area E: From N to S, $\delta^{13}C_{wax}$ values increase in the range of 3‰ within 4° of latitude reflecting the vegetation transition (from C_4 to C_3 plants) on land. Furthermore, $\delta^{13}C_{wax}$ values increase towards more distal locations by ~1‰. Such a gradient is even more pronounced in area F (2-4‰) and can be attributed to elevated inputs of coastal C_3 plants such as mangroves to sites proximal to the coast, in addition to C_4 material delivered by strong NETW during winter further offshore (Harmattan; area F), in accordance with previous results (Dupont and Agwu, 1991; Huang et al., 2000). In other words, the NETW influence in the northern half is related to the input of C_3 plant material from Mediterranean sources to the adjacent Atlantic ocean, while for the southern half, it is coupled to C_4 plant material from the Sahelian region.

The adaptation of plants to environmental conditions is reflected in a significant correlation between $\delta^{13}C_{wax}$ (for the *n*-C_{33} alkane: $r = 0.92$; $p < 0.01$) and annual MAT (**Table 5**). However, $\delta^{13}C_{wax}$ values reveal no clear relationship with water vapor pressure. These contrasting observations are likely the result of contributions from different vegetation sources to the *n*-alkane record. Based on the $\delta^{13}C_{wax}$ offsets between individual homologs, the *n*-C_{33} alkane is rather abundant in drought-exposed plants such as grasses and shrubs (Rommerskirchen et al., 2006a), explaining the damped sensitivity to water vapor pressure, while being more sensitive to MAT changes with higher temperatures favoring C_4 plants (e.g.,

Table 4: Correlations (r- and p-values) for plant-wax-specific data.

	n-C_x	r	p
δD	29/31	0.56	0.25
	31/33	0.47	0.34
	29/33	**0.94**	< 0.01
$\delta^{13}C$	29/31	**0.98**	< 0.01
	31/33	**0.91**	0.01
	29/33	**0.83**	0.04
δD vs. $\delta^{13}C$	29	-0.12	0.83
	31	0.5	0.31
	33	-0.68	0.14
	WMA	-0.12	0.83
δD vs. *n*-alkanes	29	**-0.82**	< 0.05
	31	-0.76	0.08
	33	-0.72	0.11
	WMA	**-0.92**	< 0.01
δD vs. CPI	29	-0.65	0.16
	31	-0.75	0.09
	33	-0.52	0.28
	WMA	**-0.81**	0.05
δD vs. ACL	29	-0.54	0.26
	31	-0.09	0.87
	33	-0.3	0.56
	WMA	-0.5	0.32
CPI vs. ACL		0.58	0.22
CPI vs. *n*-alkanes		**0.84**	0.04
ACL vs. *n*-alkanes		0.52	0.29

CPI, carbon preference index; ACL, average chain-length; *n*-C_x, *n*-alkanes with x carbon atoms; WMA, weighted mean average of the *n*-C_{29} , *n*-C_{31} and *n*-C_{33} alkanes. Bold values are within the 95% confidence interval ($p \leq 0.05$).

Table 5: Correlations (r- and p-values) for plant-wax-specific isotopes and environmental conditions for selected areas.

	n-C_x	r	p
δD_{wax} vs. δD_p	29	0.47	0.34
	31	**0.95**	< 0.01
	33	0.36	0.48
	WMA	0.59	0.21
δD_{wax} vs. Rainfall	29	-0.67	0.14
	31	-0.55	0.26
	33	-0.7	0.12
	WMA	-0.59	0.22
δD_{wax} vs. MAT	29	-0.7	0.12
	31	0.05	0.92
	33	**-0.83**	0.04
	WMA	-0.56	0.25
δD_{wax} vs. VP	29	-0.78	0.07
	31	-0.37	0.46
	33	**-0.88**	0.02
	WMA	-0.68	0.14
$\delta^{13}C$ vs. Rainfall	29	-0.4	0.43
	31	-0.25	0.64
	33	0.16	0.76
	WMA	-0.26	0.62
$\delta^{13}C$ vs. MAT	29	0.57	0.24
	31	0.69	0.13
	33	**0.92**	< 0.01
	WMA	0.68	0.14
$\delta^{13}C$ vs. VP	29	0.002	0.99
	31	0.16	0.76
	33	0.54	0.27
	WMA	0.15	0.78

n-C_x, *n*-alkanes with x carbon atoms; MAT, mean air temperature; VP, water vapor pressure; WMA, weighted mean average of the *n*-C_{29} , *n*-C_{31} and *n*-C_{33} alkanes. Bold values are within the 95% confidence interval ($p \leq 0.05$).

Ehleringer et al., 1997). Complementary to the finding of increasing C_4 contributions with increasing chain-length, the correlation between $\delta^{13}C_{wax}$ and MAT yields increasing significance with increasing chain-length.

Taken together, latitudinal changes in $\delta^{13}C_{wax}$ can be summarized as follows: The northern part (areas A-D) reflects the southward decrease in C_3 plant material carried by the NETW, in combination with increasing input of dust-hosted plant waxes from C_4-dominated areas in the Sahel, while the southern part (area D-F) reflects the southwards increasing C_3 vegetation cover in the tropics.

5.5.3 Sedimentary δD_{wax} and continental hydrology

δD_{wax} values of single coretop samples range between −160‰ and −118‰ (**Table 1**) and the concentration-weighted areal means range between −151‰ and −124‰ (**Table 2**). The general pattern of δD_{31} values along the transect follows that of humid and arid regions (**Fig. 5.4**), comparable to the $\delta^{13}C_{wax}$ signal (**Fig. 5.3**). When comparing δD_{wax} with δD_p, δD_{C31} appears to be the least biased indicator for annual δD_p changes ($r = 0.95$; $p < 0.01$; **Table 5**). In contrast, the other two dominant homologs (*n*-C_{29} and *n*-C_{33}) clearly deviate from δD_{31} variations in the northern half (A-C) of the transect (up to 19‰). This is reflected in statistically insignificant correlations between the homologs, except for δD_{29} and δD_{33} ($r = 0.94$; $p < 0.01$; **Table 4**). These results differ from studies carried out in mid/high latitude and high-elevation areas showing an overall good correlation of δD_{wax} values between individual homologs (e.g., Sachse et al., 2004; Bi et al., 2005; Smith and Freeman, 2006; Hou et al., 2007; Rao et al., 2009; Polissar and Freeman, 2010; Shanahan et al., 2013). Recently, Wang et al. (2013) suggested δD of the n-C_{29} alkane as the most reliable indicator for precipitation variability in environments with mixed C_3/C_4 plant contributions, while the *n*-C_{31} and *n*-C_{33} homologs were suggested to be more sensitive to vegetation changes (C_3 vs. C_4). Differences in δD_{wax} have also been observed along a transect of lacustrine surface sediments in Cameroon (Garcin et al., 2012). In this case, the δD_{29} was correlated with the δD of river water and groundwater, while δD_{31} was linked to lake water δD including its evaporative enrichment. Based on this, the two homologs were assigned to different environments, with *n*-C_{29} being derived from the surrounding catchment and *n*-C_{31} from lakeshore vegetation. Differences between those studies and our data are likely related to varying catchment sizes ranging from individual plants, soils, lake sediments to marine sediments either dominated by fluvial or eolian sedimentation processes. While lake sediments incorporate a considerable amount of plant material from the direct vicinity of the lake, marine sediments are expected to integrate large source areas because of mixing of terrigenous (organic) material from different regions and atmospheric transport over large distances (Simoneit, 1977, 1997; Simoneit et al., 1988, 1997; Schefuß et al., 2003a). In this way, various plant types from diverse ecosystems likely contributed to the marine sedimentary *n*-alkane records presented in this study. Apparently, different large-scale features are recorded by different *n*-alkanes. Similarly as

with $\delta^{13}C_{33}$, δD_{33} values show a strong correlation with MAT ($r = -0.83$; $p = 0.04$). For δD_{29}, the correlation with MAT is not significant ($r = -0.7$; $p = 0.12$), while δD_{29} and δD_{33} are consistently correlated with each other (see above). A comparable, but positive correlation to MAT was also observed along a transect of European lake sediments (in this case for the *n*-C_{29} and *n*-C_{31} alkanes), which was attributed to the increasing temperature effect on δD_p towards higher latitudes (Sachse et al., 2004). Considering lipid biosynthesis, Zhou et al. (2011) describe a negligible effect of temperature on the isotopic fractionation in C_3 and C_4 plants, while temperature does affect C_3/C_4 distribution (Ehleringer et al., 1997). Thus, the δD_{wax}-MAT relationship observed in our study most likely indicates the environmental adaptation by plants (C_3 vs. C_4) to contrasting growing seasons north (winter) and south (summer) of the Sahara, with increasing ε and thus more depleted δD_{wax} values towards the C_4 maximum in the Sahel. We still note that a direct comparison of δD_{wax} and $\delta^{13}C_{wax}$ hardly reveals any significant relationship between changes in vegetation and hydrology (**Table 4**). In contrast to $\delta^{13}C_{wax}$, water vapor pressure reveals a statistically significant influence on δD_{33} ($r = -0.88$; $p = 0.02$) and a weak one on δD_{29} ($r = -0.78$; $p = 0.07$). This is comparable to the δD_{wax}-MAT relationship, most likely due to the strong impact of MAT on the water vapor pressure. However, considering plant-dependent differences in isotopic fractionation between C_3 and C_4 plants, the correlation to MAT in conjuction with the $\delta^{13}C_{wax}$-MAT relationship suggests that, instead of δD_p, vegetation changes are the primary influence on δD_{29} and δD_{33} variations, as opposed to δD_{31} changes, which are tightly linked to δD_p variations (**Fig. 5.4**).

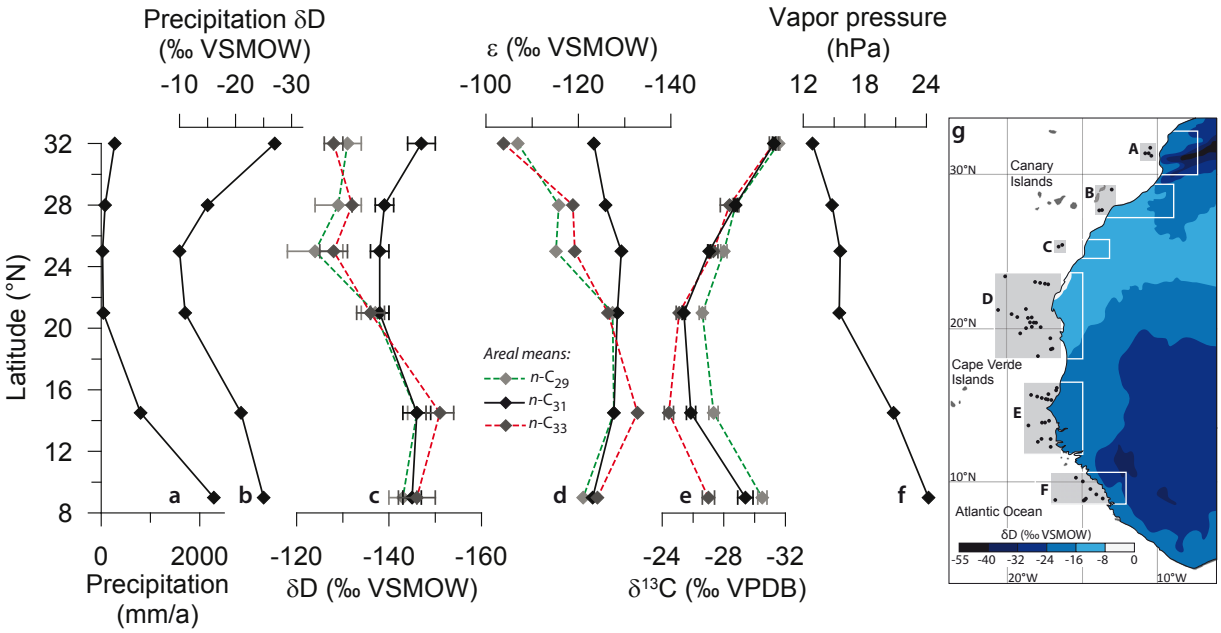

Fig. 5.4: West African hydrology. (a) Annual precipitation amounts and (b) corresponding δD values (Bowen and Revenaugh, 2003). (c) Concentration-weighted areal mean δD values for the *n*-C_{29}, *n*-C_{31} and *n*-C_{33} alkane. (d) Apparent fractionation ε between plant-wax and annual precipitation δD values. All δD values are given in ‰ (VSMOW). (e) $\delta^{13}C$ values for the *n*-C_{29}, *n*-C_{31} and *n*-C_{33} alkane (in ‰ VPDB). (f) Water vapor pressure based on the CRU TS3.22 dataset (Harris et al., 2014; New et al., 1999). (g) Annual precipitation δD values in West Africa (Bowen and Revenaugh, 2003). Grey boxes (A-F) indicate groups of coretops. White boxes indicate assumed catchments for which climatic parameters were calculated. Note the parallel changes in ε and $\delta^{13}C_{wax}$, most pronounced for the *n*-C_{29} and *n*-C_{33} alkanes (see also **Fig. 5.3** and **Table 7**).

5.5.4 Apparent fractionation ε between δD_{wax} and δD_p

Calculated ε values for long-chain *n*-alkanes reveal clear differences (**Table 6**), similar to the δD_{wax} signatures. Based on the present state of knowledge of the isotope fractionation end-members in conjunction with the vegetation signal ($\delta^{13}C_{wax}$, pollen) in our study area, the offsets in ε can be interpreted as follows:

Except for the southernmost area (F), the *n*-C_{31} alkane is the dominant homolog and is thus regarded as most representative for the total catchment vegetation, since it is the major constituent in plants adapted to aridity (Vogts et al., 2009; Rommerskirchen et al., 2006a,b), which comprise most of the vegetation along the transect. Interestingly, it displays the most constant ε (ε_{31} within a range of 6‰; **Table 6**) with a mean of −126‰ for the entire transect. As mentioned in the introduction, clear differences in ε have been observed for different plant types (Sachse et al., 2012). Accordingly, it could be expected that under more humid conditions the average ε of the catchment vegetation decreases simultaneously with a decrease in the relative proportions of grasses (both C_3 and C_4) vs. trees, with the former having the most negative ε. However, this is not the case for the *n*-C_{31} alkane. The homogeneity of ε_{31} detected in this study could potentially be the result of compensating effects of concomitant changes in climate-induced D-enrichment (more intense under dry conditions) and increased biosynthetic fractionation when more grasses and fewer trees are part of the vegetation under (semi-)arid conditions. Small latitudinal ε_{31} changes remain and can be assigned to changes in vegetation ($r = -0.89$; $p = 0.02$), though this effect appears negligible.

In contrast, the *n*-C_{29} and *n*-C_{33} alkanes reveal large gradients in ε (ε_{29}, ε_{33}) with differences of up to 30‰ (**Table 6**). This is comparable in magnitude to the δD_{wax} and ε offsets in the northern half (A-C) of the transect. Since the long-chain *n*-alkanes *n*-C_{31} and *n*-C_{33} are prominent compounds in aridity-adapted plants like grasses and shrubs (Rommerskirchen et al., 2006a,b; Vogts et al., 2009), the observed deviations between the two homologs are rather unexpected and point to different plant contributions to the individual *n*-alkane records.

The significant anti-correlation between ε_{33} and $\delta^{13}C_{33}$ ($r = -0.96$; $p < 0.01$; **Table 7**) suggests a considerable influence of vegetation type with different photosynthetic pathways and associated plant life forms on hydrogen isotope fractionation. For the northern half, however, relatively high ε_{33} values (up to −104‰) are in contrast to the average ε of C_3 grasses (−151‰ for the *n*-C_{31} alkane; Sachse et al., 2012). Explaining this discrepancy by soil-water D-enrichment alone seems insufficient, as *n*-C_{31} ε values are considerably lower (ca. −130‰). While the latter can be explained by mixed contributions from C_3 grasses and C_3 trees, the ε_{33} indicates a clearly different plant-wax source apart from grasses. According to marine sedimentary pollen assemblages off Morocco (Agwu and Dupont, 1991), prominent candidates are shrubs and herbs (e.g., *Artemisia*) from the transitional steppe, which are expected to have relatively high proportions of very long-chain *n*-alkanes (Vogts et al., 2009) and are also known to have the most positive ε (Sachse et al., 2012). The latter is not

explicitly related to biosynthetic fractionation and could also result from evaporative D-enrichment of soil water, since shrubs/herbs are common in arid environments. Less depleted ε were also observed for montane gymnosperm trees (Polissar and Freeman, 2010), which have a plant-wax *n*-alkane distribution dominated by the *n*-C_{33} alkane (Rommerskirchen et al., 2006a). Still, compared to angiosperms, gymnosperms generally produce low amounts of *n*-alkanes (Diefendorf et al., 2011; Bush and McInerney, 2013) and are unlikely to contribute significantly to the *n*-C_{33} record. Hence, for the northern half of the transect, we tentatively attribute its main origin to drought-adapted/-exposed shrubs/herbs and shrub-like trees. South of the Sahara, C_4 grasses are likely the dominant source, indicated by enriched $\delta^{13}C_{33}$ and highest percentages of *Poaceae* pollen (Agwu and Dupont, 1991), except for the southernmost part (area F) close to the rain forest with increased C_3 plant contributions (**Fig. 5.3**).

The *n*-C_{29} alkane exhibits similar ε values as the *n*-C_{33} alkane in the northern half (area A-C) of the transect, while in the southern half (D-F), it is more depleted, but closely related to the *n*-C_{31} and *n*-C_{33} alkanes (**Fig. 5.4**). Overall, changes in ε_{29} are primarily due to physiological/biosynthetic differences: For the northern half, ε_{29} shows a very good fit to the globally averaged value (−113‰) for C_3 trees (Sachse et al., 2012), while for the southern half, more depleted values are most likely the result of mixed C_3/C_4 plant contributions. Our observations from the mixed C_3/C_4 vegetation are in contrast to those from SE Africa (Wang et al., 2013), since all three major long-chain *n*-alkanes show almost identical δD_{wax} and thus ε, consistent with studies from other regions (e.g., Sachse et al., 2004; Bi et al., 2005; Smith and Freeman, 2006; Hou et al., 2007; Rao et al., 2009; Polissar and Freeman, 2010; Shanahan et al., 2013).

If the *n*-C_{31} alkane can be interpreted as a mix of C_3 trees/shrubs and C_3 grasses, at least the *n*-C_{29} alkane should also have mixed contributions, since this compound is also produced by grasses. Comparable to the southern part, indicating the presence of C_4 grasses by enriched $\delta^{13}C_{29}$, grasses likely contributed to the *n*-C_{29} alkane in the north as well. In contrast to $\delta^{13}C_{wax}$, pollen can distinguish among different C_3 plants, but *Poaceae* (grasses) show low percentages for the northern half of the transect (**Fig. 5.3**). This is somewhat in contrast to the

Table 6: Apparent fractionation (ε) between plant-wax and annual precipitation δD values (‰ VSMOW) for major long-chain *n*-alkanes.

	Annual ε			
Area	*n*-C_{29}	*n*-C_{31}	*n*-C_{33}	WMA
A	-107	-123	-104	-114
B	-116	-126	-119	-121
C	-115	-129	-119	-121
D	-127	-128	-126	-128
E	-128	-128	-133	-131
F	-121	-123	-124	-121
Mean	**-119**	**-126**	**-121**	**-123**

WMA, weighted mean average of the *n*-C_{29} , *n*-C_{31} and *n*-C_{33} alkanes.

Table 7: Correlations (r- and p-values) for apparent hydrogen isotopic fractionations (ε) of the dominant long-chain *n*-alkanes and corresponding plant-wax $\delta^{13}C$, as well as environmental conditions for selected areas.

ε	$\delta^{13}C$		MAT[a]		VP[a]		Precipitation[a]	
n-C_x	r	p	r	p	r	p	r	p
n-C_{29}	-0.75	0.08	**-0.91**	0.01	-0.57	0.23	-0.24	0.65
n-C_{31}	**-0.89**	0.02	-0.38	0.46	0.16	0.76	0.56	0.25
n-C_{33}	**-0.96**	< 0.01	**-0.96**	< 0.01	-0.67	0.14	-0.3	0.56
WMA[e]	**-0.9**	0.01	**-0.83**	0.04	-0.41	0.42	-0.02	0.97

MAT, mean air temperature; VP, water vapor pressure; *n*-C_x, *n*-alkanes with x carbon atoms; WMA, weighted mean average of the *n*-C_{29} , *n*-C_{31} and *n*-C_{33} alkanes. Bold values are within the 95% confidence interval ($p \leq 0.05$).

[a] Obtained from the CRU TS3.22 dataset (Harris et al., 2014; New et al., 1999).

more depleted ε_{31}, which can be only explained by contributions from C_3 grasses with a sufficiently low ε. Such observations emphasize the need to establish a mechanistic link between pollen and plant-wax production and transport. However, less negative ε_{29} relative to the *n*-C_{31} alkane indicates another source in addition to grasses, while these, together with shrubs, generally produce lower amounts of *n*-C_{29} alkanes compared to trees (Rommerskirchen et al., 2006a,b; Vogts et al., 2009; Garcin et al., 2014). Nevertheless, accounting for any mix of trees, shrubs and grasses to the *n*-C_{29} record would result in more negative ε_{29} compared to the observed value, which perfectly matches the average ε of C_3 trees (see above). Furthermore, the offset between *n*-C_{31} and *n*-C_{33} also clearly indicates different sources for these waxes (grasses vs. shrubs) and the potential for D-enrichment. So far, our interpretations remain tentative, since modern δD_{wax} data from Africa are not yet available. However, these findings are analogous to a $\delta^{13}C_{wax}$ comparison between plant *n*-alkanes and sedimentary *n*-alkanes in Cameroon, which suggests that different plants may contribute preferentially to different sedimentary *n*-alkanes (Garcin et al., 2014).

In summary, relatively constant ε_{31} values (within a range of 6‰) identify this compound as most reliable indicator for precipitation changes in West Africa despite the large climatic gradient and shifts in vegetation. In contrast, the *n*-C_{29} and *n*-C_{33} alkanes are strongly affected by vegetation changes (photosynthetic pathway and plant life form) and possibly climatic influences favoring soil-/leaf-water D-enrichment. Interestingly, these effects are most pronounced north of the Sahara, while the mixed C_3/C_4 vegetation in the south yields an almost consistent hydrologic signal for all three major homologs. The isotopic offsets in the north are seen as the result of chain-length-selective contributions from plants with different life forms and/or from contrasting environments. In this way, major contributions to the *n*-C_{29} alkane are likely derived from trees/forests, while the *n*-C_{33} alkane is rather indicative for shrubs and herbs under harsh climate conditions of the steppe and Atlas Mountains. The almost invariable ε_{31} across the whole transect is interpreted as a composite signal apparently compensating for nearly all influences but δD_p on the final δD_{31} signature. For the southern half, slightly more negative ε values for all three major homologs in area D and E relative to area F (< 10‰) are attributed to maxima in C_4 grasses. Nevertheless, these differences are small and constitute only a small fraction of the observed variability along the whole transect (e.g., 29‰ for *n*-C_{33} from area A to E).

5.5.5 Comparison with previous δD_{wax} calibrations and their implications for paleoclimate studies

Our results reveal more enriched δD_{31} values (>10‰) compared to a previous δD_{wax} calibration from this area (Collins et al., 2013), which is probably due to different sample materials (coretops vs. late Holocene, 0-3 ka). In addition, relatively constant ε_{31} values in our study suggest that a correction of δD_{wax} values for changes in vegetation (Collins et al., 2013) is not necessarily needed to assess δD_p, at least in West Africa. Likewise, the δD_{wax} calibration

derived from African lake sediments (Garcin et al., 2012) cannot be generally translated to marine settings, as already emphasized in a subsequent study (Garcin et al., 2014). Clear differences exist between these two approaches in terms of catchment size, thus potentially reflecting different environmental signals (see section 5.5.3). Most important are the deviations in ε: For the marine setting (this study), mean ε values south of the Sahara (area D-F) are similar among homologs, while for the lake sediments, they are considerably different (>20‰ offset between the *n*-C_{29} and *n*-C_{31} alkane), as well as more depleted compared to our study (>40‰ for *n*-C_{31}; Garcin et al., 2012). Furthermore, our calculated ε values are less negative by more than 10‰ relative to a transect of European lake sediments (−130‰ for *n*-C_{29} and −141‰ for *n*-C_{31}; Sachse et al., 2004), though such a difference is already close to the uncertainties within the available δD_p data (see Bowen and Revenaugh, 2003). Our results agree better with a δD_{wax} transect from Italy (−125‰ for *n*-C_{29} and −118‰ for *n*-C_{31}; Leider et al., 2013) with differences of less than 10‰. Comparable to our study, minor ε variations for contrasting environments have also been detected in aerosols from North America, with ε values for the *n*-C_{30} fatty acid of −125‰ and −133‰ for arid and humid regions, respectively (Gao et al., 2014), leading to a similar conclusion of a compensation effect, i.e., a more negative ε of aridity-adapted grasses is balanced by increased D-enrichment due to evapotranspiration. Since the majority of marine sedimentary plant waxes in our study area is related to dust transport, such a comparison to modern aerosols with good agreement proves the high potential for eolian mixing and thus the spatial integration of large catchments.

In general, marine sedimentary δD_{wax} values record hydrologic changes across West Africa, but also reveal distinct variations between homologs from contrasting biomes north and south of the Sahara. Obviously, regional differences complicate straightforward interpretations owing to the combined effects of several factors including photosynthetic pathway, plant life form and climate (see section 5.5.4). In support of previous studies, this emphasizes the importance to account for vegetation composition in the catchment by a combination of $\delta^{13}C_{wax}$ and pollen assemblages to derive better estimates of precipitation variability from individual homologs (e.g., Sachse et al., 2012). This also includes the consideration of geographic features like mountain ranges, which may further complicate interpretations, owing to additional effects on δD_p. Certainly, using WMA instead of isotope values derived from single compounds seems applicable to records lacking additional environmental information. Nevertheless, the relatively constant ε_{31} values across the large climatic gradient in West Africa suggest that this plant-wax compound provides a composite, catchment-integrated signal for reliable estimates of precipitation changes in the geological past. This supports previous δD_{wax} studies in this area, which focused on the *n*-C_{31} alkane to derive paleohydrologic inferences (Niedermeyer et al., 2010; Collins et al., 2013; Kuechler et al., 2013). In contrast, latitudinal changes in ε_{29} and ε_{33} are primarily related to shifts in photosynthetic pathway (from C_3 to C_4) and plant life form (shrubs to grasses), with likely but not quantifiable influences of evapotranspiration.

Finally, the isotopic offsets between homologs presented in this study may provide an additional indicator of latitudinal shifts in climate and vegetation. Differences in $\delta^{13}C_{wax}$ increase southward due to the shift from C_3 to mixed C_3/C_4 plants, while those in δD_{wax} increase northward due to varying contributions from different C_3 species and/or environments to each homolog. For instance, considering a southward shift of the tropical rainbelt and associated vegetation during the geological past, the isotopic variations between homologs are expected to decrease in $\delta^{13}C_{wax}$ and increase in δD_{wax} at a given core location close to the monsoon front. Such a relationship is likely a regional feature of the West African setting and has to be tested in the future for its reliability.

5.6 Conclusions

This study presents compound-specific isotope data of long-chain *n*-alkanes from a transect of 57 marine surface sediment samples along the West African coast between 31 and 9°N, in order to investigate the link between marine sedimentary δD_{wax} and the δD of precipitation (δD_p). Additional $\delta^{13}C_{wax}$ measurements agree well with previous results, indicating a maximum in C_4 plant contribution at the latitude of the Sahel, while C_3 plants dominate the plant-wax input off Morocco and Guinea corresponding to the vegetation cover on land. Independent of marked latitudinal climate and vegetation shifts, ε_{31} values stay relatively constant (−126‰) along the transect and reveal the best correlation with annual δD_p. In contrast, ε_{29} and ε_{33} values correlate significantly with $\delta^{13}C_{wax}$ and MAT, suggesting a strong impact of climate-induced changes in vegetation and related differences in evapotranspiration on the δD_{wax} of both homologs. These differences are most apparent in the north (area A-C), while in the south (D-F), δD_{wax} and ε values are comparable among all major *n*-alkanes. Our interpretations of the isotopic offsets in the north remain tentative, since modern δD_{wax} data from North Africa are not yet available. We interpret these offsets as characteristic features of the Mediterranean vegetation (C_3 grasses, shrubs and trees) and/or contributions from different environments (forests, steppe, Atlas Mountains) with varying degrees of evapotranspiration and associated D-enrichment of soil- and leaf-water. In this way, the *n*-C_{29} alkane seems to be mainly derived from trees/forests, while the *n*-C_{33} alkane likely has major contributions from shrubs/herbs of the steppe and Atlas Mountains. For the West African transect, the *n*-C_{31} alkane appears most suitable to derive paleohydrologic implications from marine sedimentary archives. In addition, the distinct variations in δD_{wax} and $\delta^{13}C_{wax}$ along the transect suggest that changes in the isotopic offsets between homologs might provide further indications of latitudinal shifts in climate and vegetation.

5.7 Acknowledgements

This study was financially supported by the Deutsche Forschungsgemeinschaft (DFG) through the priority programme 527 “IODP/ODP“ (Sche903/11) with additional support by the Research Center/Excellence Cluster “The Ocean in the Earth System“ at MARUM — Center for Marine Environmental Sciences, University of Bremen. RRK acknowledges additional support by GLOMAR — Bremen International Graduate School for Marine Sciences.

VI

Synthesis and outlook

The main findings of the herein presented work are highlighted in brief summaries followed by further discussion and notes, arising from each subproject, on the potentials for future research related to the fields of δD_{wax} proxy calibration and forcing of orbital-scale monsoon variability.

6.1 West African monsoon during the Last Glacial cycle and its link to insolation, sea surface temperatures and trade wind strength

The first main part (Chapter III) revealed a significant anti-correlation between δD_{wax} and $\delta^{13}C_{wax}$ at ODP Site 659 off West Africa throughout the Last Glacial cycle (last 130 ka). Complementary to published pollen data, this plant-wax signal is seen as the sensitive responses of the Sahelian vegetation cover to precipitation changes, as well as varying contributions from the Mediterranean biomes north of the Sahara (C_3 domain) by NETW. During arid phases, the Sahel experiences crucial water stress, resulting in a pronounced contraction of the vegetation cover and thus, a reduction of C_4 plant waxes exported from this area. Equally important, the increase in NETW strength during dry periods provided more C_3-plant-wax material derived from the North African C_3 plant domain. During humid periods, the C_4-dominated Sahelian environments migrated northward into the Sahara and weaker NETW supplied less C_3 plant waxes from the north. Arid-humid cycles deduced from plant-wax δD are in line with simultaneous changes in weathering intensity deduced from major element variations. In general, climate shifts are either linked to large fluctuations in Northern Hemisphere summer insolation or, like during MIS 2 and 3 with low insolation variability, to alkenone-based SST estimates.

6.2 The climatic impact of the latitudinal insolation gradient

The second main part (Chapter IV) extends the orbital-scale approach to the Pliocene and provides a revised picture of tropical monsoon variability on geological timescales, leading to the dynamic concept termed hybrid insolation forcing. Depending on the relative magnitudes of the precession and obliquity amplitudes, the West African monsoon responds preferentially to either local summer insolation (during strong precession cycles) or summer LIG (during weak precession cycles). This mechanism is already evident since the early Pliocene (5 Ma

ago) and clearly amplified during the Last Glacial cycle, most likely due to ice-albedo feedbacks that strengthen high-latitude cooling and thus, the LIG-induced temperature contrast between high and low latitudes. In a broader context, these findings should have basic implications for paleoclimate/-environmental records linked to the West African monsoon, such as Mediterranean sapropel formation and hominin evolution and migration.

6.3 δD_{wax} calibration and an additional indicator for environmental shifts

This study presented the link between marine sedimentary δD_{wax} and continental precipitation (δD_p) across a large hydrologic gradient in West Africa (31-9°N). Additional $\delta^{13}C_{wax}$ analyses agree well with previously published results, indicating a C_4 maximum at the latitude of the Sahel, while C_3 plants dominate off Morocco and Guinea corresponding to the vegetation cover. Notably, independent of the large latitudinal shifts in climate and vegetation, the apparent fractionation (ε) of the *n*-C_{31} alkane stays relatively constant (−126‰) along the transect and revealed the best correlation with annual δD_p compared to that of the *n*-C_{29} and *n*-C_{33} alkanes. In contrast, the latter two compounds correlate significantly with $\delta^{13}C_{wax}$ and mean air temperatures, indicating a strong influence of vegetation changes and, likely, related differences in water use efficiency on the corresponding δD_{wax} signatures. These differences are most apparent in the northern half of the transect, between Morocco and the Sahel, whereas in the southern half, δD_{wax} and ε values yield minor deviations among homologs despite of mixed C_3/C_4 contributions. For the West African setting, it is concluded that the *n*-C_{31} alkane appears most suitable to derive paleohydrologic reconstructions from marine sediments.

The distinct isotopic offsets between homologs presented in Chapter V may provide an additional indicator of latitudinal shifts in climate and vegetation. As such, differences in $\delta^{13}C_{wax}$ increase southward due to the shift from C_3 to mixed C_3/C_4 plants, while those in δD_{wax} increase northward due to varying contributions from different C_3 species and/or environments to each homolog. When considering a southward (northward) shift of the tropical rainbelt and associated vegetation during the geological past, the detected isotopic variations between homologs are expected to decrease (increase) in $\delta^{13}C_{wax}$ and increase (decrease) in δD_{wax} at a given position in the vicinity of the present-day monsoon front. Such a relationship is likely a regional feature of the West African setting and has to be tested in the future for its reliability.

6.4 Improving the δD_{wax} calibration

The δD_{wax} calibration in West Africa can be further strengthened through the analysis of dust/aerosol samples, in order to characterize the modern isotopic signals of eolian transported plant waxes offshore West Africa. Recently, such an approach has been undertaken in North America and demonstrated an almost constant relationship between δD_{wax} and δD_p (precipitation), despite of differences in humidity and plant communities (Gao et al., 2014). Since this is comparable to the findings presented in Chapter V, and most of the terrigenous fraction offshore West Africa is regarded as aeolian dust, the analysis of aerosols (e.g., from cruise POS425; Fischer et al., 2012; **Fig. 6.1**) will hopefully corroborate the conclusions drawn in this thesis. So far, the mapping of the $\delta^{13}C_{wax}$ signature in West African aerosols has been shown to be tightly linked to the contemporary vegetation (Schefuß et al., 2003a), which is in good agreement with coretop studies (Huang et al., 2000; this study). Preliminary lipid analysis of POS425 dust samples, collected during January 2012, yielded sufficient material for δD_{wax} measurements. Since the sample set comprises a major dust storm, sampled in high temporal resolution (2 h intervals), the comparison of such events with the "background signal" of the atmospheric dust load before and after the storm will allow further evaluation of the importance of such dust outbraks for plan-wax deposition in the subtropical Northeast Atlantic.

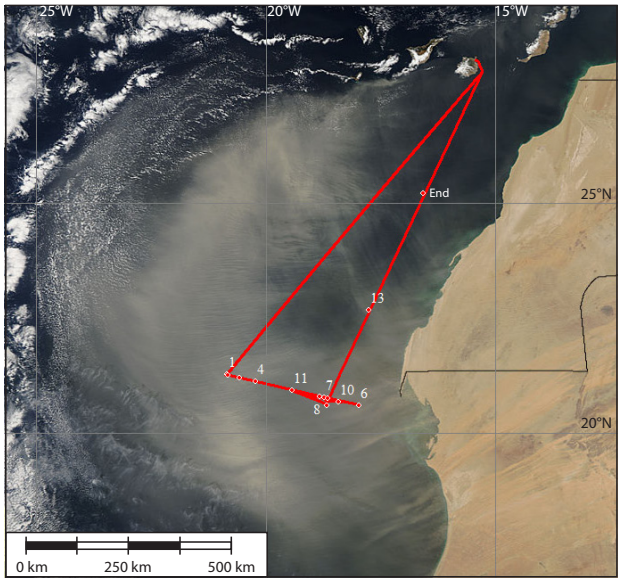

Fig. 6.1: Satellite image of a dust storm over West Africa on January 19th, 2012, with cruise track of RV Poseidon Cruise POS425 (red line) and poistions of dust samples (adapted from Fischer et al., 2012). Image source: http://lance-modis.eosdis.nasa.gov/cgi-bin/imagery/single.cgi?image=WestAfrica.A2012019.1430.2km.jpg.

6.5 Implications for the assessment of the internal monsoon variability and the linkages of low and high latitude climate

The persistent shifts in orbital periodicities (between precession and obliquity) is clearly evident within the δD_{wax} and dust records of West African arid-humid cycles, which is explained by the dominant influence of either (precession-driven) local summer insolation or the (obliquity-driven) summer LIG, depending on the strength in amplitudes of the respective forcings relative to each other (Chapter IV).

Last Glacial cycle

A comparison of climate records from West, Central and Southwestern Africa from the Last Glacial cycle further supports an influence of LIG variations (**Fig. 6.2**). With regard to phase relationships and their influence on interglacial/glacial strength (according to Jouzel et al., 2007), the exceptionally high humidity levels during the AHP seem to be the result of the in-phase relationship of a summer insolation maximum and summer LIG minimum. In contrast, the LGM occurred during a period when the insolation minimum just followed after the absolute obliquity minimum (and thus LIG maximum), providing the basis for minimal moisture generation (low insolation) and maximum moisture export from low to high latitudes

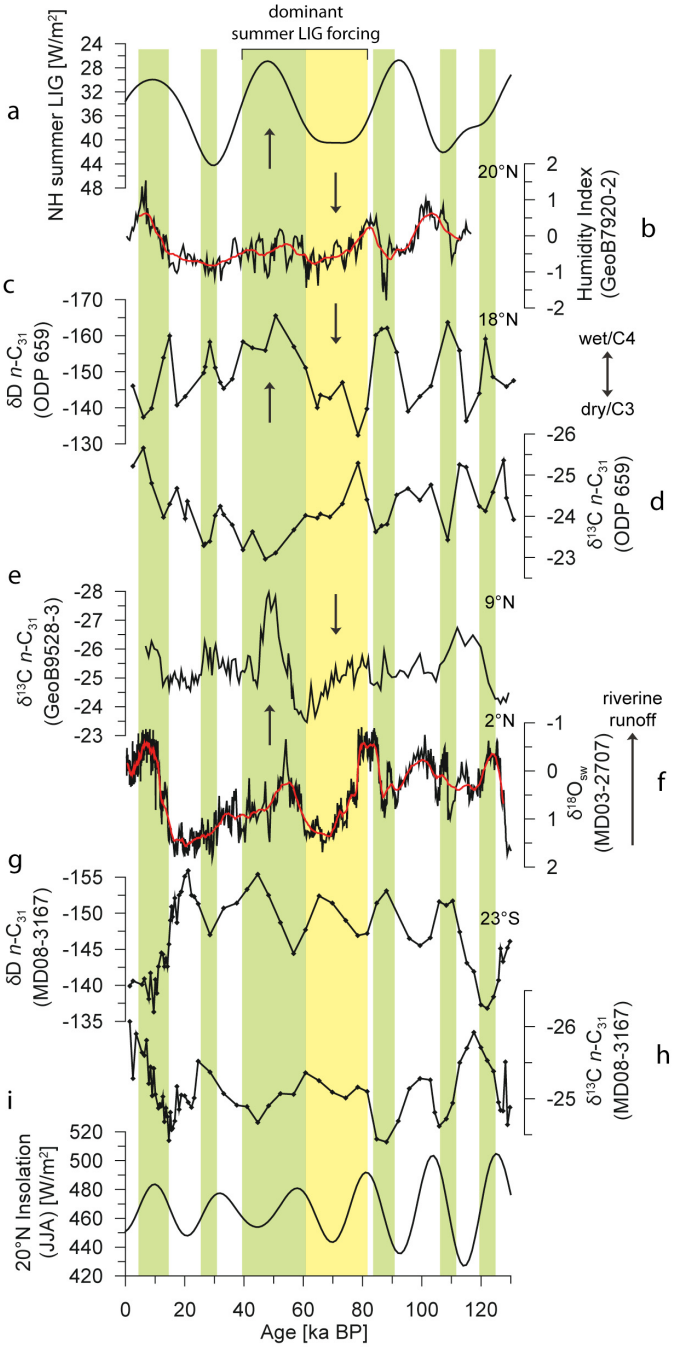

Fig. 6.2: Comparison of climate records from West, Central and Southwest Africa for the Last Glacial cycle. (a) Latitudinal insolation gradient (LIG) between 30-60°N during Northern Hemisphere (NH) summer (JJA; after Davis and Brewer, 2009). (b) Grain-size-based humidity index from GeoB7920-2 (Tjallingii et al., 2008). (c) δD and (d) $\delta^{13}C$ records of the *n*-C_{31} alkane from ODP Site 659 (this study). (e) $\delta^{13}C$ records of the *n*-C_{31} alkane from GeoB9528-3 (Castañeda et al., 2009). (f) $\delta^{18}O_{sw}$ record from MD03-2707, indicating riverine runoff (Weldeab et al., 2007). (g) δD and (h) $\delta^{13}C$ records of the *n*-C_{31} alkane from MD08-3167 (Collins et al., 2014). (i) Summer (JJA) insolation at 20°N. Orbital parameters are calculated after Laskar (1990). Vertical bars highlight humid (green) and arid (yellow) phases. Arrows mark synchronous major climate shifts during the dominant summer LIG interval. Note that the Southern Hemisphere records are in general agreement with austral summer insolation (thus in anti-phase with 20°N insolation).

(strong LIG), thus amplifying West African aridity and high-latitude ice sheet growth. Furthermore, severe dry conditions have been reported for MIS 4 (e.g., Weldeab et al., 2007; Tjallingii et al., 2008; Castañeda et al., 2009; this study), which is also marked by the combination of summer LIG maximum and insolation minimum.

While model and proxy data were able to explain the millennial-scale droughts in West Africa (linked to Heinrich events), they were inconsistent in terms of the millennial-scale humid events detected in GeoB7920-2 during MIS 3 (Tjallingii et al., 2008). Instead, the authors found good agreement with humid events detected in the western Mediterranean and assume a similar explanation, related to increased winter precipitation due to a southward shift of the mid-latitude wind systems. However, with regard to the long-term development during MIS 2-4, which seems to be mainly dominated by summer LIG variations, as postulated by the hybrid insolation forcing, the millennial-scale humid events reported by Tjallingii et al. (2008) appear as the general climate mode during this period, with millennial-scale dry spells superimposed on the orbitally forced variability. In this way, the dry spells during the summer LIG minimum around 40-60 ka (generally humid) are more pronounced than during the preceding summer LIG maximum at 60-80 ka (generally arid). Furthermore, the $\delta^{13}C_{wax}$ record from GeoB9528-3 at around 9°N (Castañeda et al., 2009) clearly supports the summer LIG forcing during MIS 3 and 4, since local summer insolation cannot account for the observed changes, as is the case for the ODP 659 records. Notably, even the $\delta^{13}C_{wax}$ record from southwestern Africa (Collins et al., 2014) rather shows a link to obliquity than to precession between 30-80 ka, in-phase with the $\delta^{13}C_{wax}$ record from the northern subtropics (ODP 659).

Interestingly, plant-wax-isotopic records from southwestern Africa revealed a generally similar pattern as was found in northwestern Africa (this study), i.e., the anti-correlation between δD_{wax} and $\delta^{13}C_{wax}$ (Collins et al., 2014). For the southern part, this was explained by stronger seasonality (more enriched $\delta^{13}C_{wax}$ and thus more C_4 plants) during insolation maxima, which also resulted in increased summer precipitation (more depleted δD_{wax}). In contrast, it is suggested in this thesis (Chapter III) that increased NETW during arid phases (more enriched δD_{wax}) provided more plant waxes from the C_3 vegetation north of the Sahara. Since the environmental context in southern Africa is comparable to the north, i.e., C_3 vegetation in the winter rainfall zone and strong trade winds during the winter season, the observed anti-correlation in the south might also result from the activity of the trade winds. However, the synchronous changes in the northern and southern parts of Africa during MIS 5 remain a challenge for assigning the responsible forcing mechanism(s), since both records have been linked to local summer insolation, which is in anti-phase between hemispheres (due to precession). It is argued in Chapter III that the slight offsets between the ODP 659 δD_{wax} record and insolation might result from uncertainties in the age model. Alternatively, according to Huybers and Denton (2008), an almost interhemispheric response to precession (and obliquity) could arise from local summer insolation intensity in the north and local

summer duration in the south. However, forcing by southern summer duration is questionable, since it is not fully confirmed by modern observations (Laepple et al., 2011). Instead, these authors suggest that a higher sensitivity to winter conditions in the south would also result in an in-phase relationship with boreal summer insolation. Recently, climate models for the AHP, which was also hemispherically symmetric, indicate a strong impact of changes in AMOC strength on the hydrology of Africa in both hemispheres (Otto-Bliesner et al., 2014). These results show that AMOC reduction, induced by deglacial meltwater input, initially caused dry conditions in both hemispheres, while its subsequent reestablishment triggered wetter conditions. However, the mechanisms were found to be different, with northern Africa responding to summer insolation and elevated greenhouse gases and southern Africa being primarily affected by greenhouse gases (Otto-Bliesner et al., 2014), which could also explain the interhemispheric symmetry of hydrologic changes in Africa since the LGM (Collins et al., 2011).

One fundamental question arising from the consistent relationship between δD_{wax} and $\delta^{13}C_{wax}$ during the Last Glacial cycle is: When and why exactly did the anti-correlation emerge? It is clear that this must have happened during the past 3 Ma, at least at ODP Site 659, since the Pliocene records (3-5 Ma) are lacking this pattern. In turn, this suggests a link to the glacial-interglacial cycles of the Northern Hemisphere, potentially associated with stronger LIG forcing due to an increase in obliquity fluctuations (see below) combined with ice-albedo feedbacks, enhancing the atmospheric circulation and thus NETW strength. Indeed, pollen assemblages from ODP 659 show that trade wind strength has intensified since 2.5 Ma, synchronous with the intensification of NHG (Vallé et al., 2014). Thus, it would be interesting to "trace back" the observed anti-correlation through the preceding glacial-interglacial cycles to its origin, and to find out whether the different proxy indications for the onset of strong NETW are consistent with each other.

Northern Hemisphere Glaciations

The interplay between high and low latitudes, based on meridional heat and moisture transport and associated feedbacks, was already demonstrated in the Introduction, including latitudinal gradients (Raymo and Nisancioglu, 2003; Davis and Brewer, 2009), as well as the strength (Jouzel et al., 2007) and duration (Tzedakis et al., 2012) of interglacials related to the phase relationship between precession and obliquity. Furthermore, it was noted that obliquity cycles have also been found in other monsoon systems, such as the Indian and East Asian monsoons (Clemens and Prell, 2007). With regard to the hybrid monsoonal forcing concept, these observations could suggest that (summer) LIG forcing is a global climate feature.

Considering the northern high latitudes, it has been suggested that increased moisture was already provided since 4.6 Ma by increased thermohaline circulation (AMOC) due to the shoaling of the CAS, and that the progressive increase in obliquity amplitudes between 3.1 and 2.5 Ma was the final step towards the build-up of large ice sheets, given the increasingly

colder summer conditions at high latitudes due to obliquity (Haug and Tiedemann, 1998). In light of the identified LIG forcing in this thesis, the increase in obliquity amplitudes necessarily implies an increase in summer LIG variability, with a strengthened LIG during obliquity minima enhancing poleward atmospheric moisture transport and thus, contributing to ice sheet growth as well. Thus, it appears most reasonable that the intensification of NHG resulted from the combined effects of various processes, already mentioned in the beginning of this thesis, including the mechanisms implemented in the Panama hypothesis (Driscoll and Haug, 1998), increased poleward freshwater fluxes and thermal isolation of Greenland (Sarnthein et al., 2009), decline in pCO_2 (e.g., see review by De Schepper et al., 2014) and the gradient hypothesis (Raymo and Nisancioglu, 2003), which is well supported by the herein presented proxy data from the subtropics.

In terms of the eccentricity signal in climate records, it has been suggested that they originate form a preferential response of the climate system to the warmer phases of the eccentricity-modulated precession cycles (Clemens and Tiedemann, 1997), as inferred from the benthic $\delta^{18}O$ record from ODP Site 659 (see also section 1.2.1). However, the Pliocene δD_{wax} and dust records from this site seem to be rather more sensitive to the colder phases of the precession cycle, since the most severe dry periods are linked to extreme insolation minima, thus creating the long-term variability of the records (see running mean of δD_{wax} in **Fig. 4.2**). The contrast in sensitivity between the $\delta^{18}O$ and δD_{wax} records seems inherent to the different systems: The benthic $\delta^{18}O$ signal registers changes in NADW formation related to NHG and thus, is likely more prone to the melting of ice sheets during warm phases, which is considered as a faster process than its build-up, potentially explaining the higher sensitivity of $\delta^{18}O$ to warmer phases of the eccentricity-modulated precession cycles. In turn, the δD_{wax} and dust variations mostly reflect changes of the Sahara-Sahel-transition, which is highly susceptible to varying precipitation amounts, presumably leading to a faster vegetation dieback and aridification under dry conditions than a greening of the Sahara during humid phases, which might explain the higher sensitivity of δD_{wax} to colder/drier phases of the eccentricity-modulated precession cycles.

Furthermore, it has been questioned that increased glacial dust fluxes are generally indicative for changes in source area aridity, since changes in wind path and strength could have a stronger impact on the amount and composition of dust (Sarnthein et al., 1982; Ratmeyer et al., 1999b). Analogous to dust, the anti-correlation between the δD_{wax} and $\delta^{13}C_{wax}$ records during the Last Glacial cycle indicates contributions from different plant-wax sources north and south of the Sahara. However, since the majority of these waxes is attributed to sources in the Sahel, also the δD_{wax} signal is regarded to reflect the hydrologic conditions of this region. In combination with the finding that δD_{wax} and dust variations are consistently correlated with each other, this suggests that also the dust signal provides a sufficient indication of source area aridity.

Conceptual model for the fusion of forcings of the West African monsoon on seasonal and orbital timescales

Evidence for LIG forcing of the West African monsoon provides the basis for further considerations of its climatic significance in this context related to the internal monsoon variability. Since it was demonstrated that *summer* LIG variations can exert a considerable influence on the northward distribution of monsoonal rainfall, the potential impact of the LIG during *winter* should also be considered. The seasonal cycle of LIG forcing strongly determines the temperature distribution (see Davis and Brewer, 2009, 2011): During summer, the LIG is weak and so is the temperature gradient, resulting from high-latitude warming under polar day conditions. This leads to a poleward shift of the main climate belts, including the tropical monsoons and mid-latitude westerlies. But during winter, the LIG strengthens due to polar night conditions at high latitudes, shifting these climate belts back towards the equator.

On orbital timescales, this means, if summer LIG controls the northernmost extent of the monsoon (most evident during eccentricity minima), than winter LIG should determine its southernmost position (likely most evident during eccentricity maxima). A stronger LIG, for both summer and winter, shifts the monsoon front towards the equator. Considering the distinct orbital signatures of the different seasonal LIG forcings (obliquity during summer and precession during winter), their phase relationships may provide deeper insights into tropical climate variability. The annual migration of the tropical rain belt from its northernmost position during summer to its southernmost position during winter defines the area of a single summer rainfall maximum. Furthermore, the area of a double rainfall maximum is defined by the winter positions of the rain belt in each hemisphere (e.g., Gasse et al., 2008). In terms of the internal monsoon variability (**Fig. 6.3**), accounting for different (seasonal) gradient forcings provides a means of estimating the potential (relative) extent of the areas with single and double annual rainfall maximum. Since the northernmost position of the monsoon front varies mostly with obliquity and its southernmost position with precession, the area in-between (i.e., the area with single rainfall maximum during summer) is determined by summer and winter LIG changes. In turn, the area of double rainfall maximum lies between the winter positions of the monsoon front of both hemispheres. Such an interpretation is in line with a synthesis of African pollen records, revealing different forcing mechanisms at different latitudes (as mentioned in the Introduction), with precession-driven tropical rain forests and obliquity-dominated subtropical vegetation with further influences of glacial boundary conditions (100 ka cycles; Dupont, 2011). Thus, the concept of a hybrid insolation forcing inferred from the ODP 659 records could also mean that the vegetation in the Sahel, or the subtropics in general, is more prone to changes at its northernmost extent during low eccentricity intervals (thus dominated by obliquity-driven summer LIG), while being more sensitive to changes at its southern boundary during high eccentricity intervals and thus precession (winter LIG).

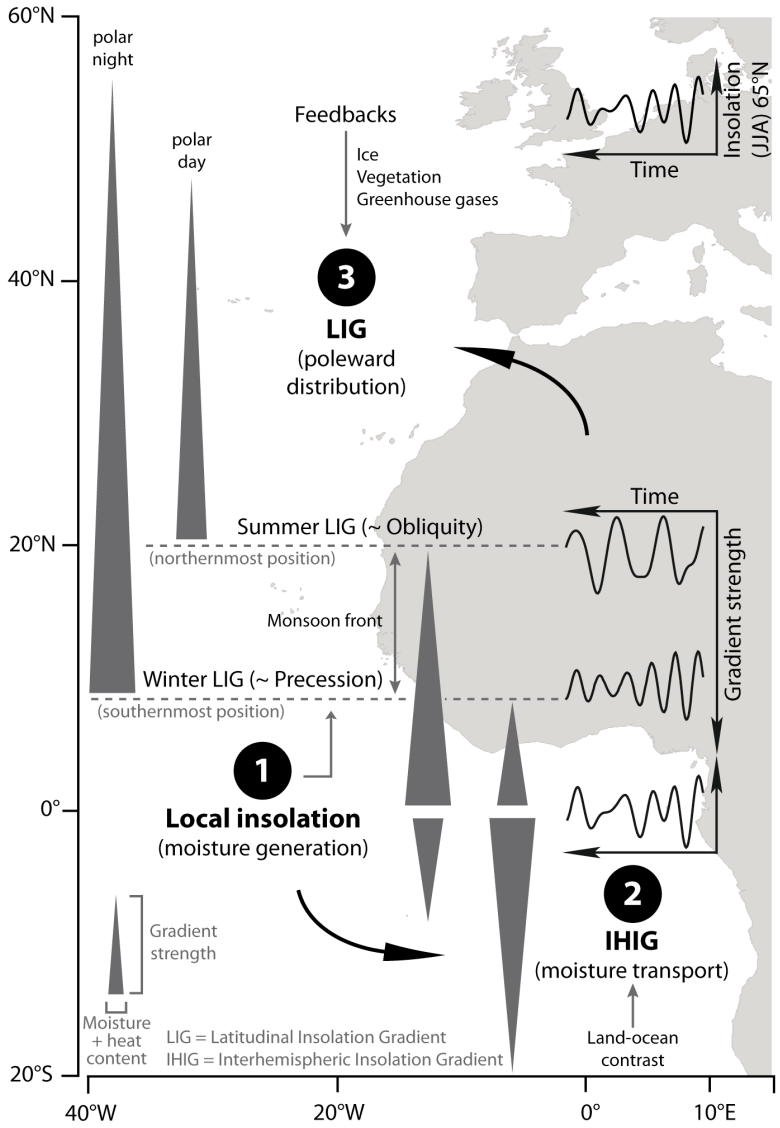

Fig. 6.3: Conceptual model for the fusion of forcings of the West African monsoon on seasonal and orbital timescales. Gradients are displayed as elongated triangles indicating relative gradient strength by length and relative moisture content by base width, shown in the lower left corner. Orbital parameters after Laskar (1990). Graphs to the right are examples for the Last Glacial cycle. (1) Local insolation is the primary driver of atmospheric moisture generation (via evapotranspiration from ocean/land) and is dominated by precession. (2) The interhemispheric insolation gradient (IHIG) controls the transport of moisture to the continent via temperature/pressure gradients (Nicholson, 2009; Bosmans et al., 2014), which are amplified by the land-ocean contrast, particularly in West Africa. Its variability on orbital timescales equals the high-latitude insolation, with a stronger influence of obliquity compared to low latitudes. (3) The latitudinal insolation gradient (LIG) between low and high latitudes influences the northward distribution of monsoonal rainfall (Davis and Brewer, 2009) and the low-to-high latitude export of energy and moisture (Raymo and Nisancioglu, 2003). A weak (strong) LIG leads to reduced (intensified) energy export from low to high latitudes and shifts the monsoon front to the north (south). Cooling at high latitudes increases the LIG effect on the latitudinal temperature gradient via ice-albedo feedbacks (and likely greenhouse gases and vegetation). In turn, an amplified temperature increase at high latitudes during warm phases, relative to the tropics, decreases the LIG-induced temperature gradient. In the same way, more vegetation at low latitudes during warm (and humid) phases dampens the insolation-induced heating via albedo feedbacks (Gasse, 2000) and thus, also reduces the temperature gradient between high and low latitudes. Today, these three insolation parameters (local insolation, IHIG, and LIG), together with feedback mechanisms, shape the temperature/pressure distribution and thus the atmospheric circulation. During summer (winter), this results in enhanced (eased) moisture generation via (1) stronger (weaker) local insolation, transport to the continent via (2) higher (lower) IHIG, and poleward distribution of monsoonal rainfall via (3) lower (higher) LIG. On orbital timescales, the phase relationships between these parameters might provide a means of estimating the relative extent of subtropical (single summer rainfall maximum) and tropical (double rainfall maximum) climate and vegetation zones (see discussion in text).

Recently, climate models confirmed a significant impact of obliquity-induced changes in LIG, but also in the interhemispheric insolation gradient (IHIG), on large-scale features of the atmospheric and ocean circulation (Mantsis et al., 2014). It was shown that low obliquity leads to (1) a weakening of the cross-equatorial Hadley circulation and thus, a reduction in meridional heat transport from the summer to the winter hemisphere, as well as (2) an increase in mid-latitude summer eddy activity, leading to an enhanced atmospheric heat transport between low and high latitudes, which also displaces the ITCZ towards the equator (Mantsis et al., 2014). While this model is in strong support for summer LIG forcing, which is indeed dominated by obliquity, the impact of obliquity on the IHIG seems far too weak, considering the orbital-scale IHIG variability, which equals high-latitude insolation (both dominated by precession; **Fig. 6.3**; see also **Fig. 1.9**). Still, the relative contributions of obliquity to summer insolation are higher at high latitudes (similar to IHIG) than at low latitudes (in contrast to IHIG), likely explaining the results of the climate model in terms of the Hadley circulation, while also equatorial climate records appear more sensitive to IHIG than local summer insolation, though differences are small. Indeed, a recent (and still ongoing) discussion rather focuses on the IHIG to explain oblilquity cycles in low-latitude climate records (Bosmans et al., 2015). However, since this is based on climate models, it is important to emphasize that subtropical proxy records are rather affected by obliquity, while tropical proxy records have a stronger precession signal (Dupont, 2011; **Fig. 6.2**). The former is most likely the result of summer LIG forcing related to its distinct orbital signature, while the latter could either result from local insolation, IHIG, winter LIG or a combination of these parameters, since all have nearly identical orbital signatures. Since all have been shown to contribute to climate variability, the combination of these likely amplifies the precession signal in the tropics. Finally, it has to be emphasized again that the clear indication for *summer* LIG forcing makes a complementary influence of *winter* LIG highly plausible, and in combination, they may provide a means of estimating the extent of the tropical and subtropical climate zones in West Africa (**Fig. 6.3**), which can be tested, for instance, with pollen and plant-wax-isotopic records.

References

A

Aichner, B., Herzschuh, U., Wilkes, H., Vieth, A., Böhner, J., 2010. δD values of *n*-alkanes in Tibetan lake sediments and aquatic macrophytes - A surface sediment study and application to a 16 ka record from Lake Koucha. *Org. Geochem.* **41**, 779−790.

Asbjornsen H., Shepherd G., Helmers M. and Mora G. (2008) Seasonal patterns in depth of water uptake under contrasting annual and perennial systems in the Corn Belt Region of the Midwestern U.S. *Plant and Soil* **308**, 69−92.

B

Bailey, I., Hole, G.M., Foster, G.L., Wilson, P.A., Storey, C.D., Trueman, C.N. Raymo, M.E., 2013. An alternative suggestion for the Pliocene onset of major northern hemisphere glaciation based the geochemical provenance of North Atlantic Ocean ice-rafted debris. *Quat. Sci. Rev.* **75**, 181–194.

Balter, M., 2011. Was North Africa the launch pad for modern human migrations?. *Science* **331**, 20–23.

Bard, E., 1988. Correction of AMS ^{14}C ages measured on planktonic foraminifera: paleoceanographic implications. *Paleoceanography* **3**, 635–645.

Bard, E., Frank, M., 2006. Climate change and solar variability: What‘s new under the sun?. *Earth Planet. Sci. Lett.* **248**, 1–14.

Bartoli, G., Sarnthein, M., Weinelt, M., Erlenkeuser, H., Garbe-Schönberg, D., Lea, D.W., 2005. Final closure of Panama and the onset of northern hemisphere glaciation. *Earth Planet. Sci. Lett.* **237**, 33–44.

Bartoli, G., Hönisch, B., Zeebe, R.E., 2011. Atmospheric CO_2 decline during the Pliocene intensification of Northern Hemisphere glaciation. *Paleoceanography* **26**, PA4213.

Berger, A.L., 1978. Long-term variations of daily insolation and Quaternary climatic changes. *J. Atmos. Sci.* **35**, 2362–2367.

Berger, A., Loutre, M.F., 1991. Insolation values for the climate of the last 10 million years. *Quat. Sci. Rev.* **10**, 297–317.

Berger, W.H., Wefer, G., 1996. Expeditions into the past: paleoceanographic studies in the South Atlantic. In: *The South Atlantic: Present and Past Circulation* (eds. Wefer, G., Berger, W.H., Siedler, G., Webb, D.J.). Springer-Verlag, Berlin, 363–410.

Berger, W.H., Burke, S., Vincent, E., 1987. Glacial- Holocene transition: Climate fluctuations and sporadic shutdown of NADW production. In: *Abrupt climatic change* (eds. W. H. Berger, L. D. Labeyrie, D. Reidel Publ. Company, Dordrecht, 279–297.

Berke, M.A., Johnson, T.C., Werne, J.P., Grice, K., Schouten, S., Sinninge Damsté, J., 2012. Molecular records of climate variability and vegetation response since the Late Pleistocene in the Lake Victoria basin, East Africa. *Quat. Sci. Rev.* **55**, 59–74.

Bi, X., Sheng, G., Liu, X., Li, C., Fu, J., 2005. Molecular and carbon and hydrogen isotopic composition of *n*-alkanes in plant leaf waxes. *Org. Geochem.* **36**, 1405–1417.

Billups, K., Ravelo, A.C., Zachos, J.C., Norris, R.D., 1999. Link between oceanic heat transport, thermohaline circulation, and the Intertropical Convergence Zone in the early Pliocene Atlantic. *Geology* **27**(4), 319–322.

Bond, G., Heinrich, H., Broecker, W., Labeyrie, L., McManus, J., Andrews, J., Huon, S., Jantschik, R., Clasen, S., Simet, C., Tedesco, K., Klas, M., Bonani, G., Ivy, S., 1992. Evidence for massive discharges of icebergs into the north Atlantic ocean during the last glacial period. *Nature* **360**, 245–249.

Bond, G., Broecker, W., Johnsen, S., McManus, J., Labeyrie, L., Jouzel, J., Bonani, G., 1993. Correlations between climate records from North Atlantic sediments and Greenland ice. *Nature* **365**, 143–147.

Bosmans, J.H.C., Drijfhout, S.S., Tuenter, E., Hilgen, F.J., Lourens, L., 2014. Response of the North African summer monsoon to precession and obliquity forcing in the EC-Earth GCM. *Clim. Dyn.* **44**(1-2), 279−297.

Bosmans, J.H.C., Hilgen, F.J., Tuenter, E., Lourens, L., 2015. Obliquity forcing of low-latitude climate. *Clim. Past Discuss.* **11**, 221−241.

Bouimetarhan, I., Prange, M., Schefuß, E., Dupont, L., Lippold, J., Mulitza, S., and Zonneveld, K., 2012. Sahel megadrought during Heinrich Stadial 1: evidence for a three-phase evolution of the low- and mid-level West African wind system. *Quat. Sci. Rev.* **58**, 66−76.

Bowen, G.J., Wilkinson, B., 2002. Spatial distribution of $\delta^{18}O$ in meteoric precipitation. *Geology* **30**(4), 315−318.

Bowen, G. J., Revenaugh, J., 2003. Interpolating the isotopic composition of modern meteoric precipitation. *Water Resources Research* **39**, 1299.

Braconnot, P., Joussaume, S., Marti, O., de Noblet, N., 1999. Synergistic Feedbacks from Ocean and Vegetation on the African Monsoon Response to Mid-Holocene Insolation, *Geophys. Res. Lett.* **26**, 2481–2484.

Braconnot, P., Joussaume, S., de Noblet, N., Ramstein, G., 2000. Mid-Holocene and Last Glacial Maximum African monsoon changes as simulated within the Paleoclimate Modelling Intercomparison Project. *Global Planet. Change* **26**, 51–66.

Braconnot, P., Otto-Bliesner, B., Harrison, S., Joussaume, S., Peterschmitt, J.-Y., Abe-Ouchi, A., Crucifx, M., Driesschaert, E., Fichefet, T., Hewitt, C.D., Kitoh, A., Laîné, A., Loutre, M.-F., Marti, O., Merkel, U., Ramstein, G., Valdes, P., Weber, S.L., Yu, Y., Zhao, Y., 2007a. Results of PMIP2 coupled simulations of the Mid-Holocene and Last Glacial Maximum – Part 1: experiments and large-scale features. *Clim. Past* **3**, 261–277.

Braconnot, P., Otto-Bliesner, B., Harrison, S., Joussaume, S., Peterschmitt, J.-Y., Abe-Ouchi, A., Crucifx, M., Driesschaert, E., Fichefet, T., Hewitt, C.D., Kitoh, A., Laîné, A., Loutre, M.-F., Marti, O., Merkel, U., Ramstein, G., Valdes, P., Weber, S.L., Yu, Y., Zhao, Y., 2007b. Results of PMIP2 coupled simulations of the Mid-Holocene and Last Glacial Maximum – Part 2: feedbacks with emphasis on the location of the ITCZ and mid- and high latitudes heat budget. *Clim. Past* **3**, 279–296.

Bray, E.E., Evans, E.D., 1961. Distribution of normal paraffins as a clue to recognition of source beds. *Geochim. Cosmochim. Acta* **22**, 2–15.

Brierley, C.M., Fedorov, A.V., 2010. Relative importance of meridional and zonal sea surface temperature gradients for the onset of the ice ages and Pliocene-Pleistocene climate evolution. *Paleoceanography* **25**, PA2214.

Brierley, C.M., Fedorov, A.V., Liu, Z., Herbert, T.H., Lawrence, K.T., LaRiviere, J.P., 2009. Greatly expanded tropical warm pool and weakened Hadley circulation in the Early Pliocene. *Science* **323**, 1714–1718.

Brohan, P., Kenndey, J.J., Harris, I., Tett, S.F.B., Jones, P.D., 2006. Uncertainty estimates in regional and global observed temperature changes: A new data set from 1850. *J. Geophys. Res.* **111**, D12106.

Bush, R.T., McInerney, F.A., 2013. Leaf wax *n*-alkane distributions in and across modern plants: Implications for paleoecology and chemotaxonomy. *Geochim. Cosmochim. Acta* **117**, 161–179.

C

Cane, M.A., Molnar, P., 2001. Closing of the Indonesian seaway as a precursor to east African aridification around 3-4 million years ago. *Nature* **411**, 157–162.

Castañeda, I.S., Mulitza, S., Schefuß, E., Lopes dos Santos, R.A., Sinninghe Damsté, J.S., Schouten, S., 2009. Wet phases in the Sahara/Sahel region and human migration patterns in North Africa. *Proc. Natl. Acad. Sci. USA* **106**(48), 20159–20163.

Cerling, T.E., Wynn, J.G., Andanje, S.A., Bird, M.I., Kimutai Korir, D., Levin, N.E., Mace, W., Macharia, A.N., Quade, J., Remien, C.H., 2011. Woody cover and hominin environments in the past 6 million years. *Nature* **476**, 51–56.

Chiapello, I., Bergametti, G., Gomes, L., Chatenet, B., Dulac, F., Pimenta, J., Santos Suares, E., 1995. An additional low layer transport of Sahelian and Saharan dust over the North-Eastern Tropical Atlantic. *Geophys. Res. Lett.* **22**(23), 3191–3194.

Chiapello, I., Bergametti, G., Chatenet, B., Bousquet, P., Dulac, F., Santos Suares, E., 1997. Origins of African dust transported over the northeastern Atlantic. *J. Geophys. Res.* **102** (D12), 13701–13709.

Chibnall, A.C., Piper, S.H., Pollard, A., Williams, E.F., Sahai, P.N., 1934. The constitution of the primary alcohols, fatty acids and paraffins present in plant and insect waxes. *Biochem. J.* **28**, 2189–2208.

Chikaraishi, Y., Naraoka, H., 2003. Compound specific δD and $\delta^{13}C$ analyses of *n*-alkanes extracted from terrestrial and aquatic plants. *Phytochemistry* **63**, 361−371.

Claussen, M., Kubatzki, C., Brovkin, V., Ganopolski, A., Hoelzmann, P., Pachur, H.-J., 1999. Simulation of an abrupt change in Saharan vegetation in the mid-Holocene. *Geophys. Res. Lett.* **26**, 2037–2040.

Clemens, S.C., 1998. Dust response to seasonal atmospheric forcing: Proxy evaluation and calibration. *Paleoceanography* **13**(5), 471–490.

Clemens, S., 1999. An astronomical tuning strategy for Pliocene sections: implications for global-scale correlation and phase relationships: *Phil. Trans. Royal Soc. London A* **357** (1757), 1949–1973.

Clemens, S., Prell, W.P., 2007. The timing of orbital-scale Indian monsoon changes. *Quat. Sci. Rev.* **26**, 275–278.

Clemens, S., Tiedemann, R., 1997. Eccentricity forcing of Pliocene-Early Pleistocene climate revealed in a marine oxygen-isotope record. *Nature* **385**, 801–804.

Colleoni, F., Masina, S., Negri, A., Marzocchi, A., 2012. Plio-Pleistocene high-low latitude climate interplay: A Mediterranean point of view. *Earth Planet. Sci. Lett.* **319–320**, 35–44.

Collins, J.A., Schefuß, E., Heslop, D., Mulitza, S., Prange, M., Zabel., M., Tjallingii, R., Dokken, T.M., Huang, E., Mackensen, A., Schulz, M., Tian, J., Zarriess, M., Wefer, G., 2011. Interhemispheric symmetry of the tropical African rainbelt over the past 23,000 years. *Nat. Geosci.* **4**, 42–45.

Collins, J.A., Schefuß, E., Heslop, D., Mulitza, S., Prange, M., Werner, M., Tharammal, T., Paul, A., Wefer, G., 2013. Estimating the hydrogen isotopic composition of past precipitation using leaf-waxes from western Africa. *Quat. Sci. Rev.* **65**, 88–101.

Collins, J. A., Schefuß, E., Govin, A., Mulitza, S., Tiedemann, R., 2014. Insolation and glacial-interglacial control on southwestern African hydroclimate over the past 140000 years. *Earth Planet. Sci. Lett.* **398**, 1−10.

Collister, J.W., Rieley, G., Stern, B., Eglinton, G., Fry, B., 1994. Compound-specific $\delta^{13}C$ analyses of leaf lipids from plants with differing carbon dioxide metabolism. *Org. Geochem.* **21**, 619–627.

Conte, M.H., Sicre, M.-A., Rühlemann, C., Weber, J.C., Schulte, S., Schulz-Bull, D., Blanz, T., 2006. Global temperature calibration of the alkenone unsaturation index (Uk37) in surface waters and comparison with surface sediments. *Geochem. Geophys. Geosyst.* **7**(2), Q02005.

Crowley, T.J., Kim, K.Y., 1996. Comparison of proxy records of climate change and solar forcing. *Geophys. Res. Lett.* **23**(4), 359–362.

D

Dansgaard, W., 1964. Stable isotopes in precipitation. *Tellus* **116**, 436−468.

Davis, B.A.S., Brewer, S., 2009. Orbital forcing and role of the latitudinal insolation/ temperature gradient. *Clim. Dyn.* **32**, 143–165.

Davis, B.A.S., Brewer, S., 2011. A unified approach to orbital, solar, and lunar forcing based on the Earth‘s latitudinal insolation/temperature gradient. *Quat. Sci. Rev.* **30**, 1861–1874.

deMenocal, P.B., 1995. Plio-Pleistocene African climate. *Science* **270**, 53–59.

deMenocal, P.B., 2001. Cultural response to climate change during the Late Holocene. *Science* **292**, 667–673.

deMenocal, P., 2004. African climate change and faunal evolution during the Pliocene-Pleistocene. *Earth Planet. Sci. Lett.* **220**, 3–24.

deMenocal, P.B., Rind, D., 1993. Sensitivity of Asian and African climate to variations in seasonal insolation, glacial ice cover, sea surface temperature, and Asian orography. *J. Geophys. Res.* **98**(D4), 7265–7287.

deMenocal, P., Ortiz, J., Guilderson, T., Adkins, J., Sarnthein, M., Baker, L., Yarusinsky, M., 2000. Abrupt onset and termination of the African Humid Period: rapid climate responses to gradual insolation forcing. *Quat. Sci. Rev.* **19**, 347–361.

De Schepper, S., Gibbard, P.L., Salzmann, U. Ehlers, J., 2014. A global synthesis of the marine and terrestrial evidence for glaciation during the Pliocene Epoch. *Earth-Sci. Rev.* **135**, 83–102.

Diefendorf, A.F., Mueller, K.E., Wing, S.L., Koch, P.L., Freeman, K.H., 2010. Global patterns in leaf ^{13}C discrimination and implications for studies of past and future climate. *Proc. Natl. Acad. Sci. USA* **107**(13), 5738–5743.

Diefendorf, A.F., Freeman, K.H., Wing, S.L., Graham, H.V., 2011. Production of *n*-alkyl lipids in living plants and implications for the geologic past. *Geochim. Cosmochim. Acta* **75**, 7472–7485.

Dolan, A.M., Haywood, A.M., Hill, D.J., Dowsett, H.J., Hunter, S.J., Lunt, D.J., Pickering, S.J., 2011. Sensitivity of Pliocene ice sheets to orbital forcing. *Palaeogeogr. Palaeoclimatol. Palaeoecol.* **309**, 98–110.

Douglas, P.M.J., Pagani, M., Brenner, M., Hodell, D.A., Curtis, J.H., 2012. Aridity and vegetation composition are important determinants of leaf-wax δD values in southeastern Mexico and Central America. *Geochim. Cosmochim. Acta* **97**, 24–45.

Dowsett, H.J., 2007. The PRISM palaeoclimate reconstruction and Pliocene sea-surface temperature. In: *Deep-time perspectives on climate change: marrying the signal from computer models and biological proxies* (eds. Williams, M., Haywood, A.M., Gregory, J., and Schmidt, D.N.), London, UK, Micropalaeontological Society (Special Publication), Geological Society of London, 459–480.

Dowsett, H.J., Robinson, M.M., Haywood, A.M., Hill, D.J., Dolan, A.M., Stoll, D.K., Chan, W.-L., Abe-Ouchi, A., Chandler, M.A., Rosenbloom, N.A., Otto-Bliesner, B.L., Bragg, F., Lunt, D.J., Foley, K.M., Riesselman, C.R., 2011. Assessing confidence in Pliocene sea surface temperatures to evaluate predictive models. *Nature Climate Change* **2**, 365–371.

Dowsett, H.J., Foley, K.M., Stoll, D.K., Chandler, M.A., Sohl, L., Bentsen, M., Otto-Bliesner, B.L., Bragg, F., Chan, W.-L., Contoux, C., Dolan, A.M., Haywood, A.M., Jonas, J.A., Jost,

A., Kamae, Y., Lohmann, G., Lunt, D.J., Nisancioglu, K.H., Abe-Ouchi, A., Ramstein, G., Riesselman, C.R., Robinson, M.M., Rosenbloom, N.A., Salzmann, U., Stepanek, C., Strother, S.L., Ueda, H., Yan, Q., Zhang, Z., 2013. Sea surface temperature of the mid-Piacenzian Ocean: A data-model comparison. *Nature, Scientific Reports* **3**, 1–8.

Driscoll, N.W., Haug, G.H., 1998. A short circuit in thermohaline circulation: A cause for Northern Hemisphere Glaciation?. *Science* **282**, 436–438.

Dupont, L.M., 1993. Vegetation zones in NW Africa during the Bruhnes chrone reconstructed from marine palynological data. *Quat. Sci. Rev.* **12**, 189–202.

Dupont, L., 2011. Orbital scale vegetation change in Africa. *Quat. Sci. Rev.* **30**, 3589–3602.

Dupont, L., Hooghiemstra, H., 1989. The Saharan-Sahelian boundary during the Brunhes chron. *Acta Botantica Neerlandica* **38**, 405–415.

Dupont, L.M., Agwu, C.O.C., 1991. Environmental control of pollen grain distribution patterns in the Gulf of Guinea and offshore NW-Africa. *Geol. Rundsch.* **80**(3), 567–589.

Dupont, L.M., Beug, H.-J., Stalling, H., Tiedemann, R., 1989. 6. First palynological results from Site 658 at 21°N off Northwest Africa: pollen as climate indicators. In: *Proc. Ocean Drill. Program Sci. Results* **108** (eds. Ruddiman, W.F., Sarnthein, M., et al.), Ocean Drilling Program, College Station, TX, 93–111.

Dupont, L.M., Donner, B., Vidal, L., Pérez, E.M., Wefer, G., 2005. Linking deset evolution and coastal upwelling: Pliocene climate change in Namibia. *Geology* **33**(6), 461–464.

Dupont, L., Rommerskirchen, F., Mollenhauer, G., Schefuß, E., 2013. Miocene to Pliocene changes in South African hydrology and vegetation in relation to the expansion of C_4 plants. *Earth Planet. Sci. Lett.* **375**, 408–417.

E

Edwards, E.J., Osborne, C.P., Strömberg, C.A.E., Smith S.A., Bond W.J., Christin P.- A., Cousins A.B., Duvall M.R., Fox D.L., Freckleton R.P., Ghannoum O., Hartwell J., Huang Y., Janis C.M., Keeley J.E., Kellogg E. a, Knapp, A.K., Leakey, A.D.B., Nelson, D.M., Saarela, J.M., Sage, R.F., Sala, O.E., Salamin, N., Still, C.J., Tipple, B., 2010. The Origins of C_4 Grasslands: Integrating Evolutionary and Ecosystem Science. *Science* **328**, 587–91.

Eglinton, G., Hamilton, R.J., 1963. The distribution of *n*-alkanes. In: *Chemical Plant Taxonomy* (ed. Swain, T.), Academic press, New York, pp. 187–217.

Eglinton, G., Hamilton, R.J., 1967. Leaf epicuticular waxes. *Science* **156**, 1322–1335.

Eglinton, T.I., Eglinton, G., 2008. Molecular proxies in paleoclimatology. *Earth Planet. Sci. Lett.* **275**, 1–16.

Eglinton, T.I., Eglinton, G., Dupont, L., Sholkovitz, E.R., Montluçon, D., Reddy, C.M., 2002. Composition, age, and provenance of organic matter in NW African dust over the Atlantic Ocean. *Geochem. Geophys. Geosyst.* **3**(8), doi: 10.1029/2001GC000269.

Ehleringer, J.R., Cerling, T.E., Helliker, B.R., 1997. C_4 photosynthesis, atmospheric CO_2, and climate. *Oecologia* **112**, 285–299.

Emeis, K.-C., Sakamoto, T., Wehausen, R., Brumsack, H.-J., 2000, The sapropel record of the eastern Mediterranean Sea - results of Ocean Drilling Program Leg 160. *Palaeogeogr. Palaeoclimatol. Palaeoecol.* **158**, 371–395.

Estep, M.F., Hoering, T.C., 1980. Biogeochemistry of the stable hydrogen isotopes. *Geochim. Cosmochim. Acta* **44**, 1197–1206.

Etourneau, J., Ehlert, C., Frank, M., Martinez, P., Schneider, R., 2012. Contribution of changes in opal productivity and nutrient distribution in the coastal upwelling system to Late Pliocene/Early Pleistocene climate cooling. *Clim. Past* **8**, 1435–1445.

F

Faugères, J.C., Legigan, P., Maillet, N., Latouche, C., 1989. 18. Pelagic, turbiditic, and contouritic sequential deposits on the Cape Verde Plateau (Leg 108, Site 659, Northwest Africa): Sediment record during Neogene time. In: *Proc. Ocean Drill. Program Sci. Results* **108** (eds. Ruddiman, W.F., Sarnthein, M., et al.), Ocean Drilling Program, College Station, TX, 311–327.

Feakins, S.J., deMenocal, P.B., 2010. Chapter 4: Global and African regional climate during the Cenozoic. In: *Cenozoic mammals of Africa* (eds. Werdelin, L., Sanders, W.J.). Berkeley, California, pp. 45–55.

Feakins, S.J., Sessions, A.L., 2010a. Controls on the D/H ratios of plant leaf waxes in an arid ecosystem. *Geochim.Cosmochim. Acta* **74**, 2128−2141.

Feakins, S.J., Sessions, A.L., 2010b. Crassulacean acid metabolism influences D/H ratio of leaf wax in succulent plants. *Org. Geochem.* **41**, 1269−1276.

Feakins, S.J., Levin, N.E., Liddy, H.M., Sieracki, A., Eglinton, T.I., Bonnefille, R., 2013. Northeast African vegetation change over 12 m.y.. *Geology* **41**, 295–298.

Fedorov, A.V., Brierley, C.M., Emanuel, K., 2010. Tropical cyclones and permanent El Nino in the early Pliocene epoch. *Nature* **463**, 1066–1069.

Fischer, G., Basse, A., Baumann, K.-H., Klann, M., Klawonn, I., Küchler, R., Nowald, N., Ruhland, G., 2012. Report and preliminary results of RV POSEIDON Cruise P425. Las Palmas – Las Palmas, 16.01.2012 – 30.01.2012. *Berichte, Fachbereich Geowissenschaften, Universität Bremen* **287**, 1–32.

Freeman, K.H., Hayes, J.M., Trendel, J.M., Albrecht, P., 1989. Evidence from GC-MS carbon-isotopic measurements for multiple origins of sedimentary hydrocarbons. *Nature* **353**, 254–256.

G

Gac, J.Y., Kane, A., 1986. Le fleuve Sénégal: I. Bilan hydrologique et flux continentaux de matières particulaires à l'embouchure. *Sci. Geol. Bull.* **39**, 99–130.

Gagosian, R.B., Peltzer, E.T., Zafiriou, O.C., 1981. Atmospheric transport of continentally derived lipids to the tropical North Pacific. *Nature* **291**, 312−314.

Gao, L., Hou, J., Toney, J., MacDonald, D., Huang, Y., 2011. Mathematical modeling of the aquatic macrophyte inputs of mid-chain *n*-alkyl lipids to lake sediments: Implications for

interpreting compound specific hydrogen isotopic records. *Geochim.Cosmochim. Acta* **75**, 3781−3791.

Gao, L., Burnier, A., Huang, Y., 2012. Quantifying instantaneous regeneration rates of plant leaf waxes using stable hydrogen isotope labeling. *Rapid Commun. Mass Spectrom.* **26**, 115–122.

Gao, L., Zheng, M., Fraser, M., Huang, Y., 2014. Comparable hydrogen isotopic fractionation of plant leaf wax n-alkanoic acids in arid and humid subtropical ecosystems. *Geochem. Geophys. Geosyst.* **15**(2), 361−373.

Garcin, Y., Schwab, V. F., Gleixner, G., Kahmen, A., Todou, G., Séné, O., Onana, J.-M., Achoungdong, G. and Sachse, D. (2012) Hydrogen isotope ratios of lacustrine sedimentary *n*-alkanes as proxies of tropical African hydrology: Insights from a calibration transect across Cameroon. *Geochim. Cosmochim. Acta* **79**, 106−126.

Garcin, Y., Schefuß, E., Schwab, V.F., Garreta, V., Gleixner, G., Vincens, A., Toudou, G., Séné, O., Onana, J.-M., Achoundong, G., Sachse, D., 2014. Reconstructing C_3 and C_4 vegetation cover using *n*-alkane carbon isotope ratios in recent lake sediments from Cameroon, Western Central Africa. *Geochim. Cosmochim. Acta* **142**, 482−500.

Gasse, F., 2000. Hydrological changes in the African tropics since the Last Glacial Maximum. *Quat. Sci. Rev.* **19**, 189–211.

Gasse, F., 2006. Cliamte and hydrological changes in tropical Africa during the past million years. *Comptes Redus Palevol* **5**, 35–43.

Gasse, F., Chalié, F., Vincens, A., Williams, M.A.J., Williamson, D., 2008. Climatic patterns in equatorial and southern Africa from 30,000 to 10,000 years ago reconstructed from terrestrial and near-shore proxy data. *Quat. Sci. Rev.* **27**, 2316–2340.

Giannini, A., Saravanan, R., Chang, P., 2003. Oceanic forcing of Sahel rainfall in interannual to interdecadal time scales. *Science* **302**, 1027–1030.

Giannini, A., Biasutti, M., Held, I.M., Sobel, A.H., 2008a. A global perspective on African climate. *Clim. Change* **90**, 359–383.

Giannini, A., Biasutti, M., Verstraete, M.M., 2008b. A climate model-based review of drought in the Sahel: Desertification, the re-greening and climate change. *Glob. Planet. Change* **64** (3-4), 119–128.

Gong, C., Eltahir, E., 1996. Sources of moisture for rainfall in west Africa. *Water Resources Research* **32**(10), 3115–3121.

Goudie, A.S., Middleton, N.J., 2001. Saharan dust storms: nature and consequences. *Earth-Sci. Rev.* **56**, 179–204.

Govin, A., Holzwarth, U., Heslop, D., Ford-Keeling, L., Zabel, M., Mulitza, S., Collins, J.A., Chiessi, C.M., 2012. Distribution of major elements in Atlantic surface sediments (36°N-49°S): imprint of terrigenous input and continental weathering. *Geochem. Geophys. Geosyst.* **13**, 1–23.

Grousset, F.E., Parra, M., Bory, A., Martinez, P., Bertrand, P., Shimmield, G., Ellam, R.M., 1998. Saharan wind regimes traced by the Sr-Nd isotopic composition of subtropical Atlantic sediments: Last Glacial Maximum vs today. *Quat. Sci. Rev.* **17**, 395−409.

H

Hall, D.M., Jones, R.L., 1961. Physiological significance of suface wax on leaves. *Nature* **191**, 95−96.

Hammer, Ø., Harper, D. A. T., Ryan, P. D., 2001. PAST: paleontological statistical software package for education and data analysis. *Palaeontologia Electronica* **4**(1), 1–9.

Handiani, D., Paul, A., Prange, M., Merkel, U., Dupont, L., Zang, X., 2013. Tropical vegetation response to Heinrich Event 1 as simulated with the UVic ESCM and CCSM3. *Clim. Past* **9**, 1683–1696.

Harris, I., Jones, P.D., Osborn, T.J., Lister, D.H., 2014. Updated high-resolution grids of monthly climatic observations - the CRU TS3.10 Dataset. *Int. J. Climatol.* **34**, 623−642.

Haug, G.H., Tiedemann, R., 1998. Effect of the formation of the Isthmus of Panama on Atlantic thermohaline circulation. *Nature* **393**, 673–676.

Haug, G.H., Sigman, D.M., Tiedemann, R., Pedersen, T., Sarnthein, M., 1999. Onset of permanent stratification in the subarctic Pacific Ocean. *Nature* **401**, 779–782.

Haug, G.H., Tiedemann, R., Zahn, R., Ravelo, A.C., 2001. Role of Panama uplift on oceanic freshwater balance. *Geology* **29**(3), 207–210.

Hayes, J.M., Freeman, K.H., Popp, B.N., Hoham, C.H., 1990. Compound specific isotope analyses, a novel tool for reconstruction of ancient biogeochemical processes. *Org. Geochem.* **16**, 1115–1128.

Hays, J.D., Imbrie, J., Shackleton, N.J., 1976. Variations in the Earth‘s orbit: Pacemaker of the Ice Ages. *Science* **194**(4720), 1121–1132.

Haywood, A.M., Valdes, P.J., 2006. Vegetation cover in a warmer world simulated using a dynamic global vegetation model for the Mid-Pliocene. *Palaeogeogr. Palaeoclimatol. Palaeoecol.* **237**, 412–427.

Haywood, A.M., Valdes, P.J., Sellwood, B.W., 2002. Magnitude of Middle Pliocene climate variability: a palaeoclimate modelling study. *Palaeogeogr. Palaeoclimatol. Palaeoecol.* **188**, 1–24.

Haywood, A.M., Dowsett, H.J., Valdes, P.J., Lunt, D.J., Francis, J.E., Sellwood, B.W., 2009. Introduction. Pliocene climate, processes and problems. *Royal Society of London Philosophical Transactions, ser. A* **367**, 3–17.

Haywood, A.M., Dolan, A.M., Pickering, S.J., Dowsett, H.J., McClymont, E.L., Prescott, C.L., Salzmann, U., Hill, D.J., Hunter, S.J., Lunt, D.J., Pope, J.O., Valdes, P.J., 2013a. On the identification of a Pliocene time slice for data-model comparison. *Royal Society of London Philosophical Transactions, ser. A* **371**, 20120515.

Haywood, A.M., Hill, D.J., Dolan, A.M., Otto-Bliesner, B.L., Bragg, F., Chan, W.-L., Chandler, M.A., Contoux, C., Dowsett, H.J., Jost, A., Kamae, Y., Lohmann, G., Lunt, D.J.,

Abe-Ouchi, A., Pickering, S.J., Ramstein, G., Rosenbloom, N.A., Salzmann, U., Sohl, L., Stepanek, C., Ueda, H., Yan, Q., Zhang, Z., 2013b. Large-scale features of Pliocene climate: results from the Pliocene Model Intercomparison Project. *Clim. Past* **9**, 191–209.

Held, I.M., Soden, B.J., 2000. Water vapor feedback and global warming. *Annu. Rev. Energy Environ.* **25**, 441–475.

Heinrigs, P., Perret, C., 2009. Chapter 15. Vulnerability in the Sahelian zone. In: *West African Studies – Regional Atlas on West Africa* (ed. Bossard, L.). OECD Publishing, Paris, 269–284.

Hilgen, F.J., 1991. Extension of the astronomically calibrated (polarity) time scale to the Miocene/Pliocene boundary. *Earth Planet. Sci. Lett.* **107**, 349–368.

Holz, C., Stuut, J.-B.W., Henrich, R., 2004. Terrigenous sedimentation processes along the continental margin off NW Africa: implications from grain-size analysis of seabed sediments. *Sedimentology* **51**, 1145–1154.

Hooghiemstra, H., Agwu, C.O.C., 1986. Distribution of palynomorphs in marine sediments: a record for seasonal wind patterns over NW Africa and adjacent Atlantic. *Geol. Rundsch.* **75**, 81–95.

Hooghiemstra, H., Bechler, A., Beug H.-J., 1987. Isopollen maps for 18,000 years B.P. of the Atlantic offshore of Northwest Africa: evidence for paleowind circulation. *Paleoceanography* **2**, 651−582.

Hooghiemstra, H., Lézine, A.-M., Leroy, S.A.G., Dupont, L., Marret, F., 2006. Late Quaternary palynology in marine sediments: A synthesis of the understanding of pollen distribution patterns in the African setting. *Quaternary International* **148**, 29–44.

Hou, J., D'Andrea, W.J., MacDonald, D., Huang, Y., 2007. Hydrogen isotopic variability in leaf waxes among terrestrial and aquatic plants around Blood Pond, Massachusetts (USA). *Org. Geochem.* **38**, 977–984.

Hou, J., D'Andrea, W., Huang, Y., 2008. Can sedimentary leaf waxes record D/H ratios of continental precipitation? *Geochim. Cosmochim. Acta* **72**, 3503–3517.

Hötzel, S., Dupont, L., Schefuß, E., Rommerskirchen, F., Wefer, G., 2013. The role of fire in Miocene to Pliocene C4 grassland and ecosystem evolution. *Nat. geosci.* **6**, 1027–1030.

Huang, Y., Dupont, L., Sarnthein, M., Hayes, J.M., Eglinton, G., 2000. Mapping of C_4 plant input from North West Africa into North East Atlantic sediments. *Geochim. Cosmochim. Acta* **64**, 3505–3513.

Huang, Y., Clemens, S.C., Liu, W., Wang, Y., Prell, W.L., 2007. Large-scale hydrological change drove the late Miocene C4 plant expansion in the Himalayan foreland and Arabian Peninsula. *Geology* **35**, 531–534.

Huybers, P., Denton, G., 2008. Antarctic temperature at orbital timescales controlled by local summer duration. *Nat. Geosci.* **1**, 787–792.

I

IAEA/WMO, 2014. Global Network of Isotopes in Precipitation. The GNIP Database. Accessible at: http://www.iaea.org/water.

Imbrie, J., Hays, J.D., Martinson, D.G., McIntyre, A., Mix, A.C., Morley, J.J., Pisias, N.G., Prell, W.L., Shackleton, N.J., 1984. The orbital theory of Pleistocene climate: support from a revised chronology of the marine del-18O record. In: *Milankovitch and Climate, Part 1* (Berger A, Imbrie J, Hays JD, Kukla G, Saltzman B eds.). Reidel Publishing Co., Dordrecht, 269–305.

Imbrie, J., Berger, A., Boyle, E.A., Clemens, S.C., Duffy, A., Howard, W.R., Kukla, G., Kutzbach, J., Martinson, D.G., McIntyre, A., Mix, A.C., Molfino, B., Morley, J.J., Peterson, L.C., Pisias, N.G., Prell, W.L., Raymo, M.E., Shackleton, N.J., Toggweiler, J.R., 1992. On the structure and origin of major glaciation cycles, part 1: Linear responses to Milankovitch forcing. *Paleoceanography* **7**, 701–738.

Imbrie, J., Berger, A., Boyle, E.A., Clemens, S.C., Duffy, A., Howard, W.R., Kukla, G., Kutzbach, J., Martinson, D.G., McIntyre, A., Mix, A.C., Molfino, B., Morley, J.J., Peterson, L.C., Pisias, N.G., Prell, W.L., Raymo, M.E., Shackleton, N.J., Toggweiler, J.R., 1993. On the structure and origin of major glaciation cycles, part 2: The 100,000-year cycle. *Paleoceanography* **8**, 699–735.

Indermühle, A., Stocker, T.F., Joos, F., Fischer, H., Smith, H.J., Wahlen, M., Deck, B., Mastroianni, D., Tschumi, J., Blunier, T., Meyer, R., Stauffer, B., 1999. Holocene carbon-cycle dynamics based on CO_2 trapped in ice at Taylor Dome, Antarctica. *Nature* **398**, 121–126.

IPCC, 2014. Summary for Policymakers. In: *Climate Change 2014: Synthesis Report* (eds. the Core Writing Team, Pachauri, R.K., Meyer, L.), Fifth Assessment Report of the Intergovernmental Panel on Climate Change.

J

Jansen, E., Fronval, T., Ranck, F., Channell, J.E.T., 2000. Pliocene-Pleistocene ice rafting history and cyclicity in the Nordic Seas during the last 3.5 Myr. *Paleoceanogr.* **15**, 709–721.

Jouzel, J., Masson-Delmotte, V., Cattani, O., Dreyfus, G., Falourd, S., Hoffmann, G., Minster, B., Nouet, J., Barnola, J.M., Chappellaz, J., Fischer, H., Gallet, J.C., Johnsen, S., Leuenberger, M., Loulergue, L., Luethi, D., Oerter, H., Parrenin, F., Raisbeck, G., Raynaud., D., Schilt, A., Schwander, J., Selmo, E., Souchez, R., Spahni, R., Stauffer, B., Steffensen, J.P., Stenni, B., Stocker, T.F., Tison, J.L., Werner, M., Wolff, E.W., 2007. Orbital and millennial Antarctic climate variability over the past 800,000 years. *Science* **317**, 793–796.

Jullien, E., Grousset, F., Malaize, B., Duprat, J., Sanchez-Goni, M.F., Eynaud, F., Charlier, K., Schneider, R., Bory, A., Bout, V., Flores, J.A., 2007. Low-latitude "dusty events" vs. high-latitude "icy Heinrich events". *Quaternary Research* **68**(3), 379–386.

K

Kahmen, A., Simonin, K., Tu, K.P., Merchant, A., Callister, A., Siegwolf, R., Dawson, T.E., Arnddt, S.K., 2008. Effects of environmental parameters, leaf physiological properties and leaf water relations on leaf water $\delta^{18}O$ enrichment in different Eucalyptus species. *Plant, Cell and Environment* **31**, 738–751.

Kahmen, A., Schefuß, E., Sachse, D., 2013a. Leaf water deuterium enrichment shapes leaf wax *n*-alkane δD values of angiosperm plants I: Experimental evidence and mechanistic insights. *Geochim. Cosmochim. Acta* **111**, 39–49.

Kahmen, A., Hoffmann, B., Schefuß, E., Arndt, S.K., Cernusak, L.A., West, J.B., Sachse, D., 2013b. Leaf water deuterium enrichment shapes leaf wax *n*-alkane δD values of angiosperm plants II: Observational evidence and global implications. *Geochim. Cosmochim. Acta* **111**, 50–63.

Kang, S.M., Lu, J., 2012. Expansion of the Hadley Cell under global warming: winter versus summer. *J. Climate* **25**, 8387-8393.

Karner, D.B., Muller, R.A., 2000. A causality problem for Milankovitch. *Science* **288**(5474), 2143–2144.

Khélifi, N., Sarnthein, M., Andersen, N., Blanz, T., Frank, M., Garbe-Schönberg, D., Haley, B.A., Stumpf, R., Weinelt, M., 2009. A major and long-term Pliocene intensification of the Mediterranean outflow, 3.5-3.3 Ma ago. *Geology* **37**(9), 811–814.

Klocker, A., Prange, M., Schulz, M., 2005. Testing the influence of the Central American Seaway on orbitally forced Northern Hemisphere glaciation. *Geophys. Res. Lett.* **32**, L03703.

Kohfeld, K.E., Harrison, S.P., 2001. DIRTMAP: the geological record of dust. *Earth-Sci. Rev.* **54**, 81–114.

Kolattukudy, P.E., 1976. The Chemistry and Biochemistry of Natural Waxes. Elsevier.

Kuechler, R.R., Schefuß, E., Beckmann, B., Dupont, L., Wefer, G., 2013. NW African hydrology and vegetation during the Last Glacial cycle reflected in plant-wax-specific hydrogen and carbon isotopes. *Quat. Sci. Rev.* **82**, 56–67.

Kukla, G., Berger, A., Lotti, R., Brown, J., 1981. Orbital signatures of interglacials. *Nature* **290**, 295–300.

Kuper, R., Kröpelin, S., 2006. Climate-controlled Holocene occupation in the Sahara: Motor of Africa's evolution. *Science* **313**, 803–807.

Kutzbach, J.E., 1981. Monsoon climate of the Early Holocene: climate experiment with the Earth's orbital parameters for 9000 years ago. *Science* **214**(4516), 59–61.

Kutzbach, J.E., Street-Perrott, F.A., 1985. Milankovitch forcing of fluctuations in the level of tropical lakes from 18 to 0 kyr BP. *Nature* **317**, 130–134.

L

Laepple, T., Werner, M., Lohmann, G., 2011. Synchronicity of Antarctic temperatures and local solar insolation on orbital timescales. *Nature* **471**, 91–94.

Lange, H., 1982. Distribution of chlorite and kaolinite in eastern Atlantic sediments off North Africa. *Sedimentology* **29**, 427–431.

Larrasoaña, J.C., Roberts, A.P., Rohling, E.J., 2013. Dynamics of green Sahara periods and their role in hominin evolution. *PLOS ONE* **8**(10), e76514.

Laskar, J., 1990. The chaotic motion of the solar system: a numerical estimate of the size of the chaotic zones. *Icarus* **88**, 266–291.

Laskar, J., Jouzel, F., Boudin, F., 1993. Orbital, precession, and insolation quantities for the Earth from –20 Myr to +10 Myr. *Astron. Astrophys.* **270**, 522–533.

Laskar, J., Robutel, P., Joutel, F., Gastineau, M., Correia, A.C.M., Levrard, B., 2004. A long term numerical solution for the insolation quantities of the Earth. *Astron. Astrophys.* **428**, 261–285.

Leider, A., Hinrichs, K.-U., Schefuß, E., Versteegh, G.J.M., 2013. Distribution and stable isotopes of plant wax derived *n*-alkanes in lacustrine, fluvial and marine surface sediments along an Eastern Italian transect and their potential to reconstruct the hydrological cycle. *Geochim. Cosmochim. Acta* **117**, 16−32.

Leroy, S., Dupont, L., 1994. Development of vegetation and continental aridity in northwestern Africa during the Late Pliocene: the pollen record of ODP Site 658. *Palaeogeogr. Palaeoclimatol. Palaeoecol.* **109**, 295–316.

Lichtfouse, E., Derenne, S., Mariotti, A., Largeau, C., 1994. Possible algal origin of long chain odd *n*-alkanes in immature sediments as revealed by distributions and carbon isotope ratios. *Org. Geochem.* **22**, 1023-1027.

Lindzen, R.S., 1990. Dynamics in Atmospheric Physics. Cambridge University Press, New York.

Lindzen, R.S., 1994. Climate dynamics and global change. *Ann. Rev. Fluid. Mech.* **26**, 353–378.

Lisiecki, L.E., Raymo, M.E., 2005. A Plio-Pleistocene stack of 57 globally distributed benthic $\delta^{18}O$ records. *Paleoceanography* **20**, PA1003.

Lisiecki, L.E., Raymo, M.E., 2009. Diachronous benthic $\delta^{18}O$ responses during late Pleistocene terminations. *Paleoceanography* **24**, PA3210.

Li, C., Sessions, A. L., Valentine, D. L., and Thiagarajan, N., 2011, D/H variations in terrestrial lipids from Santa Barbara Basin over the past 1400 years: A preliminary assessment of paleoclimatic relevance. *Org. Geochem.* **42**, 15–24.

Liu, W., Yang, H., 2008. Multiple controls for the variability of hydrogen isotopic compositions in higher plant *n*-alkanes from modern ecosystems. *Glob. Change Biol.* **14**, 2166−2177.

Liu, W., Yang, H., Li, L., 2006. Hydrogen isotopic compositions of *n*-alkanes from terrestrial plants correlate with their ecological life forms. *Oecologia* **150**, 330−338.

Lourens, L.J., Antonarakou, A., Hilgen, F.J., Van Hoof, A.A.M., Vergnaud-Grazzini, C., Zachariasse, W.J., 1996a. Evaluation of the Plio-Pleistocene astronomical timescale. *Paleoceanography* **11**(4), 391–413.

Lourens, L.J., Hilgen, F.J., Raffi, I., Vergnaud-Grazzini, C., 1996b. Early Pleistocene chronology of the Vrica section (Calabria, Italy). *Paleoceanography* **11**(6), 797–812.

Lunt, D.J., Foster, G.L., Haywood, A.M., Stone, E.J., 2008. Late Pliocene Greenland glaciation controlled by a decline in atmospheric CO_2 levels. *Nature* **454**, 1102–1105.

Lunt, D.J., Haywood, A.M., Schmidt, G.A., Salzmann, U.,Valdes, P., Dowsett, H.J., 2010. Earth system sensitivity inferred from Pliocene modelling and data. *Nat. Geosci.* **3**, 60–64.

M

Magill, C.R., Ashley, G.M., Freeman, K.H., 2013a. Ecosystem variability and early human habitats in eastern Africa. *Proc. Natl. Acad. Sci. USA* **110**(4), 1167–1174.

Magill, C.R., Ashley, G.M., Freeman, K.H., 2013b. Water, plants and early human habitats in eastern Africa. *Proc. Natl. Acad. Sci. USA* **110**(4), 1175–1180.

Mantsis, D.F., Lintner, B.R., Broccoli, A.J., Erb, M.P., 2014. The response of large-scale circulation to obliquity-induced changes in meridional heating gradients. *J. Climate* **27**, 5504–5516.

Marlow, J.R., Lange, C.B., Wefer, G., Rosell-Melé, A., 2000. Upwelling intensification as part of the Pliocene-Pleistocene climate transition. *Science* **290**, 2288–2291.

Marlowe, I.T., 1984. Lipids as palaeoclimatic indicators, 273 pp., Ph.D thesis, Univ. of Bristol, Bristol, UK.

Marlowe, I.T., Brassell, S.C., Eglinton, G., Green, J.C. 1990. Long-chain alkenones and alkyl alkenoates and the fossil coccolith record of marine sediments, Chem. Geol. 88, 349–375.

Matsuzaki, K.M.R., Eynaud, F., Malaizé, B., Grousset, F.E., Tisserand, A., Rossignol, L., Charlier, K., Jullien, E., 2011. Paleoceanography of the Mauretanian margin during the last two climatic cycles: From planktonic foraminifera to African climate dynamics. *Mar. Micropaleontol.* **79**, 67–79.

Mayaux, P., Bartholomé, E., Fritz, S., Belward, A., 2004. A new land-cover map of Africa for the year 2000. *J. Biogeogr.* **31**, 861–877.

Mazurek, M.A., Simoneit, B.R.T., 1984. Characterization of biogenic and petroleum-derived organic matter in aerosols over remote, rural and urban areas. In: *Identification and Analysis of Organic Pollutants in Air* (ed. Keith, L.H.), Ann Arbor Science, Butterworth Publishers, Ann Arbor, MI, London, pp. 353–370.

McDougall, I., Brown, F.H., Fleagle, J.G., 2005. Stratigraphic placement and age of modern humans from Kibish, Ethiopia. *Nature* **433**, 733–736.

McInerney, F.A., Helliker, B.R., Freeman, K.H., 2011. Hydrogen isotope ratios of leaf wax *n*-alkanes in grasses are insensitive to transpiration. *Geochim. Cosmochim. Acta* **75**, 541–554.

McManus, J.F., Francois, R., Gherardi, J.M., Keigwin, L.D., Brown-Leger, S., 2004. Collapse and rapid resumption of Atlantic meridional circulation linked to deglacial climate changes. *Nature* **428**, 834–837.

Meyer, I., Davies, G.R., Stuut, J.-B., 2011. Grain sizecontrol on Sr-Nd isotope provenance studies and impact on paleoclimate reconstructions: An example from deep-sea sediments offshore NW Africa. *Geochem. Geophys. Geosyst.* **12**(3), Q3005.

Milankovitch, M., 1930/1972. Mathematische Klimalehre und astronomische Theorie der Klimaschwankungen. Kraus Reprint, Nendeln/Liechtenstein.

Milankovitch, M., 1941. Kanon der Erdbestrahlung und seine Andwendung auf das Eiszeiten-problem. *Royal Serbian Academy, Special Publication* **132**, Belgrade.

Mittelstaedt, E., 1991. The ocean boundary along the northwest African coast: Circulation and oceanographic properties at the sea surface. *Prog. Oceanog.* **26**, 307–355.

Mix, A.C., Bard, E., Schneider, R., 2001. Environmental processes of the ice age: land, oceans, glaciers (EPILOG). *Quat. Sci. Rev.* **20**, 627–657.

Moulin, C., Chiapello, I., 2004. Evidence of the control of summer atmospheric transport of African dust over the Atlantic by Sahel sources from TOMS satellites (1979-2000). *Geophys. Res. Lett.* **31**, L02107.

Mudelsee, M., Raymo, M.E., 2005. Slow dynamics of the Northern Hemisphere glaciation. *Paleoceanography* **20**(4), PA4022.

Mulitza, S., Prange, M., Stuut, J.-B., Zabel, M., von Dobeneck, T., Itambi, A.C., Nizou, J., Schulz, M., Wefer, G., 2008. Sahel megadroughts triggered by glacial slowdowns of Atlantic meridional overturning. *Paleoceanography* **23**, PA4206.

Muller, R.A., MacDonald, G.J., 1995. Glacial cycles and orbital inclination. *Nature* **377**, 107-108.

Muller, R.A., MacDonald, G.J., 1997a. Symultaneous presence of orbital inclination and eccentricity proxy climate records from Ocean Drilling Program Site 806. *Geology* **25**(1), 3–6.

Muller, R.A., MacDonald, G.J., 1997b. Glacial cycles and astronomical forcing. *Science* **277**, 215–218.

Muller, R.A., MacDonald, G.J., 1997c. Spectrum of 100-kyr glacial cycle: Orbital inclination, not eccentricity. *Proc. Natl. Acad. Sci. USA* **94**, 8329–8334.

Muller, R.A., MacDonald, G.J., 2002. Ice Ages and Astronomical Causes. Springer-Verlag, New York.

Müller, P.J., Kirst, G., Ruhland, G., von Storch, I., Rosell-Melé, A., 1998. Calibration of the alkenone paleotemperature index $U^{k'}_{37}$ based on core-tops from the eastern South Atlantic and the global ocean (60°N-60°S). *Geochim. Cosmochim. Acta* **62**, 1757–1772.

N

Naafs, B.D.A., Stein, R., Hefter, J., Khélifi, N., De Schepper, S., Haug, G.H., 2010. Late Pliocene changes in the North Atlantic Current. *Earth Planet. Sci. Lett.* **298**, 434–442.

New, M., Hulme, M., Jones, P.D., 1999. Representing twentieth-century space-time climate variability. Part I: development of a 1961-90 mean monthly terrestrial climatology. *J. Climate* **12**, 829–856.

Nicholson, S.E., 1981. Rainfall and atmospheric circulation during drought periods and wetter years in Africa. *Mon. Weather Rev.* **109**, 137–154.

Nicholson, S.E., 1996. A review of climate dynamics and climate variability in eastern Africa. In: *The Limnology, Climatology and Paleoclimatology of the East African Lakes* (eds. Johnson, T.C., Odada, E.). Gordon & Breach, 25–56.

Nicholson, S.E., 2000. The nature of rainfall variability over Africa on time scales of decades to millenia. *Glob. Planet Change Lett.* **26**, 137–158.

Nicholson, S.E., 2009. A revised picture of the structure of the "monsoon" and land ITCZ over West Africa. *Clim. Dyn.* **32**, 1155–1171.

Nicholson, S.E., Grist, J.P., 2003. The seasonal evolution of the atmospheric circulation over West Africa and equatorial Africa. *J. Clim.* **16**(7), 1013-1030.

Nicolás, J., Chiari, M., Crespo, J., Garcia Orellana, I., Lucarelli, F., Nava, S., Pastor, C., Yubero, E., 2008. Quantification of Saharan and local dust impact in an arid Mediterranean area by the positive matrix factorization (PMF) technique. *Atmos. Environ.* **42**, 8872–8882.

Nie, J., 2011. Coupled 100-kyr cycles between 3 and 1 Ma in terrestrial and marine paleoclimatic records. *Geochem. Geophys. Geosys.* **12**(10), Q10Z32.

Niedermeyer, E.M., Prange, M., Mulitza, S., Mollenhauer, G., Schefuß, E., Schulz, M., 2009. Extratropical forcing of Sahel aridity during Heinrich stadials. *Geophys. Res. Lett.* **36**, L20707.

Niedermeyer, E.M., Schefuß, E., Sessions, A.L., Mulitza, S., Mollenhauer, G., Schulz, M., Wefer, G., 2010. Orbital- and millennial-scale changes in the hydrologic cycle and vegetation in the western African Sahel: insights from individual plant wax δD and $\delta^{13}C$. *Quat. Sci. Rev.* **29**(23-24), 2996–3005.

Niedermeyer, E.M., Sessions, A.L., Feakins, S.J., Mohtadi, M., 2014. Hydroclimate of the western Indo-Pacific Warm Pool during the past 24,000 years. *Proc. Natl. Acad. Sci. USA* **111**(26), 9402−9406.

O

Osborne, A.H., Vance, D., Rohling, E.J., Barton, N., Rogerson, M., Fello, N., 2008. A humid corridor across the Sahara for the migration of early modern humans out of Africa 120,000 years ago. *Proc. Natl. Acad. Sci. USA* **105**, 16444–16447.

Otto-Bliesner, B.L., Russell, J.M., Clark, P.U., Liu, Z., Overpeck, J.T., Konecky, B., deMenocal, P., Nicholson, S.E., He, F., Lu, Z., 2014. Coherent changes of southeastern equatorial and northern African rainfall during the last deglaciation. *Science* **346**(6214), 1223–1227.

P

Pagani, M., Pedentchouk, N., Huber, M., Sluijs, A., Schouten, S., Brinkhuis, H., Sinnighe Damsté, J.S., Dickens, G.R., and the Expedition 302 Scientists, 2006. Arctic hydrology during global warming at the Paleocene/Eocene thermal maximum. *Nature* **442**, 671−675.

Pagani, M., Liu, Z., LaRiviere, J., Ravelo, A.C., 2010. High Earth-system climate sensitivity determined from Pliocene carbon dioxide concentrations. *Nat. Geosci.* **3**, 27−30.

Pedentchouk, N., Summer, W., Tipple, B., Pagani, M., 2008. $\delta^{13}C$ and δD compositions of n-alkanes from modern angiosperms and conifers: An experimental set up in central Washington State, USA. *Org. Geochem.* **39**, 1066−1071.

Peixoto, J.P., Oort, A.H., 1992. Physics of Climate. American Institute of Physics, New York.

Philander, S.G., Fedorov, A.V., 2003. Role of tropics in changing the response to Milankovich forcing some three million years ago. *Paleoceanography* **18**(2), 1045.

Petit, J.R., Jouzel, J., Raynaud, D., Barkov, N.I., Barnola, J.-M., Basile, I., Bender, M., Chapellaz, J., Davis, M., Delaguye, G., Delmotte, M., Kotlyakov, V.M., Legrand, M., Lipenkov, V.Y., Lorius, C., Pépin, L., Ritz, C., Saltzman, E., Stievenard, M., 1999. Climate and atmospheric history of the past 420,000 years from the Vostok ice core, Antarctica. *Nature* **399**, 429–436.

Pinot, S., Ramstein, G., Harrison, S.P., Prentice, I.C., Guiot, J., Stute, M., Joussaume, S., 1999. Tropical paleoclimates at the Last Glacial Maximum: comparison of Paleoclimate Modeling Intercomparison Project (PMIP) simulations and paleodata, *Clim. Dyn.* **15**, 857–874.

Polissar, P.J., Freeman, K.H., 2010. Effects of aridity and vegetation on plant-wax δD in modern lake sediments. *Geochim. Cosmochim. Acta* **74**, 5785−5797.

Poynter, J.G., Farrimond, P., Robinson, N., Eglinton, G., 1989. Aeolian-derived higher plant lipids in marine sedimentary records: links with paleoclimate. In: *Paleoclimatology and Paleometeorology: Modern and Past Patterns of Atmospheric Transport* (eds. Leinen, M., Sarnthein, M.). Kluwer Academy, Norwell, MA, pp. 435−462.

Prahl, F.G., Wakeham, S.G., 1987. Calibration of unsaturation patterns in long-chain ketone compositions for palaeotemperature assessment. *Nature* **330**, 367–369.

Prange, M., Schulz, M., 2004. A coastal upwelling seesaw in the Atlantic Ocean as a result of the closure of the Central American Seaway. *Geophys. Res. Lett.* **31**, L17207.

Prospero, J.M., 1996. Saharan dust transport over the North Atlantic Ocean and Mediterranean: an overview. In: *The Impact of Desert Dust Across the Mediterranean* (eds. Guerzoni, S., Chester, R.), Kluwer Academic Publishers, Netherlands, pp. 133–151.

Prospero, J.M., Ginoux, P., Torres, O., Nicholson, S.E., Gill, T.E., 2002. Environmental characterization of global sources of atmospheric soil dust identified with the Nimbus 7 Total Ozon Mapping Spectrometer (TOMS) absorbing aerosol product. Rev. Geophys. 40 (1), 1002.

Pye, K., 1987. Aeolian Dust and Dust Deposits. 334 pp., Elsevier, New York.

R

Rao, Z., Zhu, Z., Jia, G., Henderson, A.C.G., Xue, Q., Wang, S., 2009. Compound-specific δD values of long chain *n*-alkanes derived from terrestrial higher plants are indicative of the δD of meteoric waters: Evidence from surface soils in eastern China. *Org. Geochem.* **40**, 922−930.

Ratmeyer, V., Fischer, G., Wefer, G., 1999a. Lithogenic particle fluxes and grain size distribution in the deep ocean off northwest Africa: Implications for seasonal changes of aeolian dust input and downward transport. *Deep-Sea Res. Pt. I* **46**, 1289−1337.

Ratmeyer, V., Balzer, W., Bergametti, G., Chiapello, I., Fischer, G., Wyputta, U., 1999b. Seasonal impact of mineral dust on deep-ocean particle flux in the eastern subtropical Atlantic Ocean. *Mar. Geol.* **159**, 241–252.

Raymo, M.E., 1998. Glacial puzzles. *Science* **281**, 1467–1468.

Raymo, M.E., Nisancioglu, K., 2003. The 41 kyr world: Milankovich's other unsolved mystery. *Paleoceanography* **18**(1), 1011.

Raymo, M.E., Huybers, P., 2008. Unlocking the mysteries of the ice ages. *Nature* **451**, 284–285.

Raymo, M.E., Ruddiman, W.F., Froelich, P.N., 1988. Influence of late Cenozoic mountain building on ocean geochemical cycles. *Geology* **16**(7), 649–653.

Raymo, M.E., Ruddiman, W.F., Backman, J., Clement, B.M., Martinson, D.G., 1989. Late Pliocene variation in northern Hemisphere ice sheets and North Atlantic deep water circulation, *Paleoceanography* **4**, 413–446.

Raymo, M.E., Ruddiman, W.F., Shackleton, N.J., Oppo, D.W., 1990. Evolution of Atlantic-Pacific $\delta^{13}C$ gradients over the last 2.5 m.y.. *Earth Planet. Sci. Lett.* **97**, 353–368.

Raymo, M.E., Grant, B., Horowitz, M., Rau, G.H., 1996. Mid-Pliocene warmth: stronger greenhouse and stronger conveyor. *Mar. Micropaleontol.* **27**, 313–326.

Raymo, M.E., Lisiecki, L.E., Nisancioglu, K.H., 2006. Plio-Pleistocene ice volume, Antarctic climate, and the global $\delta^{18}O$ record. *Science* **313**(5786), 492–495.

Ravelo, A.C., Andreasen, D.H., Lyle, M., Olivarez Lyle, A., Wara, M.W., 2004. Regional climate shifts caused by gradual global cooling in the Pliocene epoch. *Nature* **429**, 263–267.

Rieley, G., Collier, R.J., Jones, D.M., Eglinton, G., Eakin, P.A., Fallick, A.E., 1991. Sources of sedimentary lipids deduced from stable carbon isotopic analyses of individual compounds. *Nature* **352**, 425–427.

Rieley, G., Collister, J.W., Stern, B., Eglinton, G., 1993. Gas chromatography/isotope ratio mass spectrometry of leaf wax *n*-alkanes from plants of differing carbon dioxide metabolisms. *Rapid Commun. Mass Spectrom.* **7**, 488– 491.

Risi, C., Bony, S., Vimeux, F., 2008a. Influence of convective processes on the isotopic composition ($\delta^{18}O$ and δD) of precipitation and water vapor in the tropics: 2. Physical interpretation of the amount effect. *J. Geophys. Res.* **113**, D19306.

Risi, C., Bony, S., Vimeux, F., Descroix, L., Ibrahim, B., Lebreton, E., Mamadou, I., Sultan, B., 2008b. What controls the isotopic composition of the African monsoon precipitation? Insights from event-based precipitation collected during the 2006 AMMA field campaign. *Geophys Res. Let.* **35**, L24808.

Rommerskirchen, F., Plader, A., Eglinton, G., Chikaraishi, Y., Rullkötter, J., 2006a. Chemotaxonomic significance of distribution and stable carbon isotopic composition of long-chain alkanes and alkan-1-ols in C_4 grass waxes. *Org. Geochem.* **37**, 1303–1332.

Rommerskirchen, F., Eglinton, G., Dupont, L., Rullkötter, J., 2006b. Glacial/interglacial changes in southern Africa: compound-specific $\delta^{13}C$ land plant biomarker and pollen records from southeast Atlantic continental margin sediments. *Geochem. Geophys. Geosyst.* **7**, Q08010.

Rossignol-Strick, M., 1983. African monsoons, an immediate climate response to orbital insolation. *Nature* **304**, 46–49.

Rozanski, K., Araguás-Araguás, L., Gonfiantini, R., 1993. Isotopic patterns in modern global precipitation. In: *Climate Change in Continental Isotopic Records* (eds. Swart, P.K., Lohmann, K.C., McKenzie, J., Savin, S.), *Geophysical Monograph* **78**, American Geophysical Union, Washington, pp. 1–36.

Röhl, U., Abrahams, L.J., 2000. High-resolution, downhole and non-destructive core measurements from Sites 999 and 1001 in the Carribean Sea: application to the Late Paleocene Thermal Maximum. In: *Proc. Ocean Drill. Program Sci. Results* **165**, College Station, TX (Ocean Drilling Program), 191–203.

Ruddiman, W.F., 2006. What is the timing of orbital-scale monsoon changes?. *Quat. Sci. Rev.* **25**, 657–658.

Ruddiman, W.F., Sarnthein, M., Backman, J., Baldauf, J.G., Curry, W., Dupont, L.M., Janecek, T., Pokras, E.M., Raymo, M.E., Stabell, B., Stein, R., Tiedemann, R., 1989a. Late Miocene to Pleistocene evolution of climate in Africa and the low-latitude Atlantic: overview of Leg 108 results. In: *Proc. Ocean Drill. Program Sci. Results* **108** (eds. Ruddiman, W.F., Sarnthein, M., et al.), Ocean Drilling Program, College Station, TX, 463–484.

Ruddiman, W.F., Raymo, M.E., Martinson, D.G., Clement, B.M., Backman, J., 1989b. Pleistocene evolution: Northern hemisphere ice sheets and North Atlantic Ocean. *Paleoceanography* **4**, 413–446.

S

Sachse, D., Radke, J., Gleixner, G., 2004. Hydrogen isotope ratios of recent lacustrine sedimentary *n*-alkanes record modern climate variability. *Geochim. Cosmochim. Acta* **68**, 4877−4889.

Sachse, D., Radke, J., Gleixner, G., 2006. δD values of individual *n*-alkanes from terrestrial plants along a climatic gradient - Implications for the sedimentary biomarker record. *Org. Geochem.* **37**, 469−483.

Sachse, D., Kahmen, A., Gleixner, G., 2009. Significant seasonal variation in the hydrogen isotopic composition of leaf-wax lipids for two deciduous tree ecosystems (*Fagus sylvativa* and *Acer pseudoplatanus*). *Org. Geochem.* **40**, 732−742.

Sachse, D., Gleixner, G., Wilkes, H., Kahmen, A., 2010. Leaf wax *n*-alkane δD values of field-grown barley reflect leaf water δD values at the time of leaf formation. *Geochim. Cosmochim. Acta* **74**, 6741−6750.

Sachse, D., Billaut, I., Bowen, G.J., Chikaraishi, Y., Dawson, T.E., Feakins, S.J., Freeman, K.H., Magill, C.R., McInerney, F.A., van der Meer, M.T.J., Polissar, P., Robins, R.J., Sachs, J.P., Schmidt, H.-L., Sessions, A.L., White, J.W.C., West, J.B., Kahmen, A., 2012. Molecular Paleohydrology: Interpreting the hydrogen-isotopic composition of lipid biomarkers from photosynthesizing organisms. *Annu. Rev. Earth Planet. Sci.* **40**, 221–249.

Salzmann, U., Haywood, A.M., Lunt, D.J., Valdes, P.J., Hill, D.J., 2008. A new global biome reconstruction and data-model comparison for the Middle Pliocene. *Global Ecol. Biogeogr.* **17**, 432–447.

Salzmann, U., Williams, M., Haywood, A.M., Johnson, A.L.A., Kender, S., Zalasiewicz, J., 2011. Climate and environment of a Pliocene warm world. *Palaeogeogr. Palaeoclimatol. Palaeoecol.* **309**, 1–8.

Salzmann, U., Dolan, A.M., Haywood, A.M., Chan, W.-L., Voss, J., Hill, D.J., Abe-Ouchi, A., Otto-Bliesner, B.L., Bragg, F., Chandler, M.A., Contoux, C., Dowsett, H.J., Jost, A., Kamae, Y., Lohmann, G., Lunt, D.J., Pickering, S.J., Pound, M.J., Ramstein, G., Rosenbloom, N.A., Sohl, L., Stepanek, C., Ueda, H., Zhang, Z., 2013. Challenges in quantifying Pliocene terrestrial warming revealed by data-model discord. *Nature Climate Change* **3**, 969–974.

Samuels, L., Kunst, L., Jetter, R., 2008. Sealing plant surfaces: Cuticular wax formation by epidermal cells. *Annu. Rev. Plant. Biol.* **59**, 683–707.

Sarnthein, M., Tiedemann, R., 1989. 12. Toward a high-resolution stable isotope stratigraphy of the last 3.4 million years: Sites 658 and 659 off Northwest Africa. In: *Proc. Ocean Drill. Program Sci. Results* **108** (eds. Ruddiman, W.F., Sarnthein, M., et al.), Ocean Drilling Program, College Station, TX, 167–185.

Sarnthein, M., Tetzlaff, G., Koopmann, B., Wolter, K., Pflaumann, U., 1981. Glacial and interglacial wind regimes over the eastern subtropical Atlantic and North-West Africa. *Nature* **293**, 193–196.

Sarnthein, M., Thiede, J., Pflaumann, U., Erlenkeuser, H., Fütterer, D., Koopmann, B., Lange, H., Seibold, E., 1982. Atmospheric and oceanic circulation patterns off Northwest Africa during the past 25 million years. In *Geology of the Northwest African Continental Margin* (eds. U. Rad, K. Hinz, M. Sarnthein and E. Seibold). Springer-Verlag, Berlin, 545−604.

Sarnthein, M., Winn, K., Jung, S.J.A., Duplessy, J.-C., Labeyrie, L., Erlenkeuser, H., Ganssen, G. 1994. Changes in east Atlantic deep-water circulation over the last 30000 years: Eight time slice reconstructions. *Paleoceanography* **9**, 209–267.

Sarnthein, M., Stattegger, K., Dreger, D., Erlenkeuser, H., Grootes, P., Haupt, B., Jung, S., Kiefer, T., Kuhnt, W., Pfaumann, U., Schäfer-Neth, C., Schulz, H., Schulz, M., Seidov, D., Simstich, J., van Kreveld, S., Vogelsang, E., Völker, A., Weinelt, M., 2000. Fundamental modes and abrupt changes in North Atlantic circulation and climate over the last 60 ky - concepts, reconstruction and numerical modeling. In: *The Northern North Atlantic: A Changing Environment* (eds. Schäfer, P.. Ritzrau, W., Schlüter, M., Thiede, J.), Springer-Verlag, Berlin, pp. 365−410.

Sarnthein, M., Bartoli, G., Prange, M., Schmittner, A., Schneider, B., Weinelt, M., Andersen, N., Garbe-Schönberg, D., 2009. Mid-Pliocene shifts in ocean overturning circulation and the onset of Quaternary-style climates. *Clim. Past* **5**, 269–283.

Schefuß, E., Ratmeyer, V., Stuut, J.-B.W., Jansen, J.H.F., Sinnighe Damsté, J.S., 2003a. Carbon isotope analyses of *n*-alkanes in dust from the lower atmosphere over the central eastern Atlantic. *Geochim. Cosmochim. Acta* **67**, 1757–1767.

Schefuß, E., Schouten, S., Jansen, J.H.F., Sinninghe Damsté, J.S., 2003b. African vegetation controlled by tropical sea surface temperatures in the mid-Pleistocene. *Nature* **422**, 418–421.

Schefuß, E., Schouten, S., Schneider, R.R., 2005. Climatic controls on central African hydrology during the past 20,000 years. *Nature* **437**, 1003–1006.

Schefuß, E., Kuhlmann, H., Mollenhauer, G., Prange, M., Pätzold, J., 2011. Forcing of wet phases in southeast Africa over the past 17,000 years. *Nature* **480**, 509–512.

Scheuvens, D., Schütz, L., Kandler, K., Ebert, M., Weinbruch, S., 2013. Bulk composition of northern African dust and its source sediments - a compilation. *Earth-Sci. Rev.* **116**, 170–194.

Schimmelmann, A., Sessions, A.L., Mastalerz, M., 2006. Hydrogen isotopic (D/H) composition of organic matter during diagenesis and thermal maturation. *Annu. Rev. Earth Planet. Sci.* **34**, 501−533.

Schmitz W.J., 1995. On the interbasin-scale thermohaline circulation, *Rev. Geophys.* **33**, 151–173.

Schrag, D.P., Adkins, J.F., McIntyre, K., Alexander, J.L., Hodell, D.A., Charles, C.D., McManus, J.F., 2002. The oxygen isotopic composition of seawater during the Last Glacial Maximum. *Quat. Sci. Rev.* **21**, 331–342.

Seki, O., Foster, G.L., Schmidt, D.N., Mackensen, A., Kawamura, K., Pancost, R.D., 2010. Alkenone and boron-based Pliocene pCO_2 records. *Earth Planet. Sci. Lett.* **292**, 201–211.

Sessions, A.L., Burgoyne, T.W., Schimmelmann, A., Hayes, J.M., 1999. Fractionation of hydrogen isotopes in lipid biosynthesis. *Org. Geochem.* **30**, 1193−1200.

Sessions. A.L., Sylva, S.P., Summons, R.E., Hayes, J.M., 2004. Isotopic exchange of carbon-bound hydrogen over geological timescales. *Geochim. Cosmochim. Acta* **68**(7), 1545−1559.

Shackleton, N.J., 2000. The 100,000-year ice-age cycle identified and found to lag temperature, carbon dioxide, and orbital eccentricity. *Science* **289**, 1897–1902.

Shackleton, N.J., Berger, A., Peltier, W.R., 1990. An alternative astronomical calibration of the lower Pleistocene timescale based on ODP site 677. *Trans. R. Soc. Edinburgh Earth Sci.* **81**, 251–261.

Shanahan, T.M., Hughen, K.A., Ampel, L., Sauer, P.E., Fornace, K., 2013. Environmental control of the 2H/1H values of terrestrial leaf waxes in the Canadian Arctic. *Geochim. Cosmochim. Acta* **119**, 286-301.

Shepherd, T., Griffith, D. W., 2006. The effects of stress on plant cuticular waxes. *New Phytologist* **171**, 469−499.

Sigman, D.M., Boyle, E.A., 2000. Glacial/interglacial variations in atmospheric carbon dioxide. *Nature* **407**, 859−869.

Simoneit, B.R.T., 1984. Organic matter of the troposphere – III. Characterization and sources of petroleum and pyrogenic residues in aerosols over the western United States. *Atmos. Environ.* **18**, 51–67.

Simoneit, B.R.T., 1997. Compound-specific carbon isotope analyses of individual long-chain alkanes and alkanoic acids in Harmattan aerosols. *Atmos. Environ.* **31**, 2225–2233.

Simoneit, B.R.T., Chester, R., Eglinton, G., 1977. Biogenic lipids in particulates from the lower atmosphere over the eastern Atlantic. *Nature* **267**, 682–685.

Simoneit, B.R.T., Cox, R.E., Standley, L.J., 1988. Organic matter of the troposphere - IV. Lipids in Harmattan aerosols of Nigeria. *Atmos. Environ.* **22**, 983–1004.

Skinner, L.C., Shackleton, N.J., 2005. An Atlantic lead over Pacific deep-water change across Termination I: Implications for the application of the marine isotope stage stratigraphy, *Quat. Sci. Rev.* **24**, 571–580.

Skinner, L.C., Shackleton, N.J., 2006. Deconstructing Terminations I and II: Revisiting the glacioeustatic paradigm based on deep-water temperature estimates, *Quat. Sci. Rev.* **25**, 3312–3321.

Skonieczny, C., Bory, A., Bout-Roumazeilles, V., Abouchami, W., Galer, S.J.G., Crosta, X., Stuut, J.-B., Meyer, I., Chiapello, I., Podvin, T., Chatenet, B., Diallo, A., Ndiaye, T., 2011. The 7-13 March 2006 major Saharan outbreak: Multiproxy characterization of mineral dust deposited on the West African margin. *J. Geophys. Res.* **116**, D18210.

Smith, F.A., Freeman, K.H., 2006. Influence of physiology and climate on δD of leaf wax *n*-alkanes from C_3 and C_4 grasses. *Geochim. Cosmochim. Acta* **70**, 1172–1187.

Soon, W., Legates, D.R., 2013. Solar irradiance modulation of Equator-to-Pole (Arctic) temperature gradients: Empirical evidence for climate variation on multi-decadal timescales. *J. Atmos. Sol.-Terr. Phys.* **93**, 45–56.

Stager, J.C., Ryves, D.B., Chase, B.M., Pausata, F.S.R., 2011. Catastrophic drought in the Afro-Asian monsoon region during Heinrich Event 1. *Science* **331**, 1299–1302.

Standley, L.J., Simoneit, B.R.T., 1987. Composition of extractable organic matter in smoke particles from prescribed burns. *Environ. Sci. Technol.* **21**, 163–169.

Steinberger, B., Spakman, W., Japsen, P., Torsvik, T.H., 2015. The key role of solid-Earth processes in preconditioning Greenland‘s glaciation since the Pliocene. *Terra Nova* **0(0)**, 1–8.

Steph, S., Tiedemann, R., Prange, M., Groeneveld, J., Schulz, M., Timmermann, A., Nürnberg, D., Rühlemann, C., Saukel, C., Haug, G.H., 2010. Early Pliocene increase in thermohaline overturning: A precondition for the development of the modern equatorial Pacific cold tongue: *Paleoceanography* **25**, PA2202.

Sternberg, L.D.L., 1988. D/H ratios of environmental water recorded by D/H ratios of plant lipids from submerged plants. *Nature* **333**, 59−61.

Street-Perrott, F.A., Perrott, R.A., 1990. Abrupt climate fluctuations in the tropics: the influence of Atlantic Ocean circulation. *Nature* **343**, 607–612.

Stringer, C., 2000. Coasting out of Africa. *Nature* **405**, 24–27.

Strömberg, C.A.E., 2011. Evolution of Grasses and Grassland Ecosystems. *Annu. Rev. Earth Planet. Sci.* **39**, 517–544.

Stuiver, M., Reimer, P., Reimer, R.W., 2005. CALIB 5.0.

Stuut, J.-B., Zabel, M., Ratmeyer, V., Helmke, P., Schefuß, E., Lavik, G., Schneider, R., 2005. Provenance of present-day eolian dust collected off NW Africa. *J. Geophys. Res.* **110**, D04202.

Sun, Y., Ramstein, G., Contoux, C., Zhou, T., 2013. A comparative study of large-scale atmospheric circulation in the context of a future scenario (RCP4.5) and past warmth (mid-Pliocene). *Clim. Past* **9**, 1613–1627.

T

Taylor, C.M., Gounou, A., Guichard, F., Harris, P.P., Ellis, R.J., Couvreux, F., De Kauwe, M., 2011. Frequency of Sahelian storm initiation enhanced over mesoscale soil-moisture patterns. *Nat. Geosci.* **4**, 430–433.

ten Haven, H.L., Rullkötter, J., Stein, R., 1989. 20. Preliminary analysis of extractable lipids in sediments from the eastern North Atlantic (Leg 108): Comparison of a coastal upwelling area (Site 658) with a nonupwelling area (Site 659). In *Proc. Ocean Drill. Program Sci. Results* **108** (eds. Ruddiman, W.F., Sarnthein, M., et al.), Ocean Drilling Program, College Station, TX, 351–360.

Thiede, J., Winkler, A., Wolf-Welling, T., Eldholm, O., Myhre, A.M., Baumann, K.-H., Henrich, R., Stein, R., 1998. Late Cenozoic history of the Polar North Atlantic: results from ocean drilling. *Quat. Sci. Rev.* **17**(1–3), 185–208.

Tiedemann, R., Sarnthein, M., Stein, R., 1989. 15. Climatic changes in the western Sahara: aeolo-marine sediment record of the last 8 million years (Sites 657-661). In: *Proc. Ocean Drill. Program Sci. Results* **108** (eds. Ruddiman, W.F., Sarnthein, M., et al.), Ocean Drilling Program, College Station, TX, 241–278.

Tiedemann, R., Sarnthein, M., Shackleton, N.J., 1994. Astronomic timescale for the Pliocene Atlantic $\delta^{18}O$ and dust flux records of Ocean Drilling Program site 659. *Paleoceanography* **9**(4), 619–638.

Tierney, J.E., deMenocal, P.B., 2013. Abrupt shifts in Horn of Africa hydroclimate since the Last Glacial Maximum. *Science* **342**, 843–846.

Tierney, J.E., Russell, J.M., Huang, Y., Sinnighe Damsté, J.S., Hopmans, E.C., Cohen, A.S., 2008. Northern hemisphere controls on tropical Southeast African climate during the past 60,000 years. *Science* **322**, 252–255.

Tierney, J.E., Oppo, D.W., Rosenthal, Y., Russell, J.M., Linsley, B.K., 2010. Coordinated hydrological regimes in the Indo-Pacific region during the past two millennia. *Paleoceanography* **25**, PA1102.

Tierney, J.E., Russell, J.M., Sinnighe Damsté, J.S., Huang, Y., Verschuren, D., 2011. Late Quaternary behavior of the East African monsoon and the importance of the Congo Air Boundary. *Quat. Sci. Rev.* **30**, 798−807.

Tipple, B.J., Pagani, M., 2007. The Early Origins of Terrestrial C_4 Photosynthesis. *Annu. Rev. Earth Planet. Sci.*, **35**, 435–461.

Tipple, B.J., Pagani, M., 2010. A 35 Myr North American leaf-wax compound-specific carbon and hydrogen isotope record: Implications for C_4 grassland expansion and hydrologic cycle dynamics. *Earth Planet. Sci. Lett.* **299**, 250−262.

Tipple, B.J., Berke, M.A., Doman, C.E., Khachaturyan, S., Ehleringer, J.R., 2013. Leaf-wax *n*-alkanes record the plant-water environment at leaf flush. *Proc. Natl. Acad. Sci. USA* **110** (7), 2659–2664.

Tjallingii, R., Claussen, M., Stuut, J.-B.W., Fohlmeister, J., Jahn, A., Bickert, T., Lamy, F., Röhl, U., 2008. Coherent high- and low-latitude control of the northwest African hydrological balance. *Nat. Geosci.* **1**(10), 670–675.

Torrence, C., Compo, G.P., 1998. A practical guide to wavelet analysis: *Bull. Am. Meteorol. Soc.* **79**, 61–78.

Trauth, M.H., Maslin, M.A., Deino, A.L., Strecker, M.R., Bergner, A.G.N., Dühnforth, M., 2007. High- and low-latitude forcing of Plio-Pleistocene East African climate and human evolution. *J. Hum. Evol.* **53**, 475–486.

Trauth, M.H., Larrasoaña, J.C., Mudelsee, M., 2009. Trends, rhythms and events in Plio-Pleistocene African climate. *Quat. Sci. Rev.* **28**(5-6), 399–411.

Tuenter, E., Weber, S.L., Hilgen, F.J., Lourens, L., 2003. The response of the African summer monsoon to remote and local forcing due to precession and obliquity. *Global and Planetary Change* **36**, 219–235.

Tzedakis, P.C., Wolff, E.W., Skinner, L.C., Brovkin, V., Hodell, D.A., McManus, J.F., and Raynaud, D., 2012. Can we predict the duration of an interglacial?. *Clim. Past* **8**, 1473–1485.

V

Vallé, F., Dupont, L.M., Leroy, S.A.G., Schefuß, E., and Wefer, G., 2014. Pliocene environmental change in West Africa and the onset of strong NE trade winds (ODP Sites 659 and 658): *Palaeogeogr. Paleoclimatol. Palaeoecol.* **414**, 403–414.

Vidal, L., Labeyrie, L., Cortijo, E., Arnold, M., Duplessy, J.C., Michel, E., Becqué, S., van Weering, T.C.E., 1997. Evidence for changes in the North Atlantic Deep Water linked to meltwater surges during the Heinrich events. *Earth Planet. Sci. Lett.* **146**, 13–27.

Vimeux, F., Masson, V., Jouzel, J., Stievenard, M., Petit, J.R., 1999. Glacial-interglacial changes in ocean surface conditions in the Southern Hemisphere. *Nature* **398**, 410–413.

Vogts, A., Moossen, H., Rommerskirchen, F., Rullkötter, J., 2009. Distribution patterns and stable carbon isotopic composition of alkanes and alkan-1-ols from plant waxes of African rain forest and savanna C_3 species. *Org. Geochem.* **40**, 1037–1054.

Vogts, A., Schefuß, E., Badewien, T., Rullkötter, J., 2012. *n*-Alkane parameters from a deep sea sediment transect off southwest Africa reflect continental vegetation and climate conditions. *Org. Geochem.* **47**, 109–119.

Volkman, J.K., Eglinton, G., Corner, E.D.S., Sargent, J.R., 1980. Novel unsaturated straight-chain C_{37}–C_{39} methyl and ethyl alkenones in marine sediments and a coccolithophore *Emiliania huxleyi*. In: *Advances in Organic Geochemistry* (eds. Douglas, A.G., Maxwell, J.R.), Elsevier, New York, pp. 219–227.

W

Waelbroeck, C., Labeyrie, L., Michel, E., Duplessy, J.C., McManus, J.F., Lambeck, K., Balbon, E., Labracherie, M., 2002. Sea-level and deep water temperature changes derived from benthic foraminifera isotopic records. *Quat. Sci. Rev.* **21**, 295–305.

Wang, Y.V., Larsen, T., Leduc, G., Andersen, N., Blanz, T., Schneider, R.R., 2013. What does leaf wax δD from a mixed C3/C4 vegetation tell us? *Geochim. Cosmochim. Acta* **111**, 128−139.

Watrin, J., Lézine, A.-M., Hély, C., and Contributors, 2009, Plant migration and plant communities at the time of the “green Sahara”. *Comptes Redus Geoscience* **341**, 656–670.

Weber, S.L., Tuenter, E., 2011. The impact of varying ice sheets and greenhouse gases on the intensity and timing of boreal summer monsoons. *Quat. Sci. Rev.* **30**, 469–479.

Weijers, J.W.H., Schefuß, E., Schouten, S., Sinninghe Damsté, J.S., 2007. Coupled Thermal and Hydrological Evolution of Tropical Africa over the Last Deglaciation. *Science* **315**, 1701–1704.

Weldeab, S., Lea, D.W., Schneider, R.R., Andersen, N., 2007. 155,000 years of West African monsoon and ocean thermal evolution. *Science* **316**, 1303–1307.

White, F., 1983. The Vegetation of Africa. *Natural Resources Research* **20**, UNESCO, Paris.

White, T.D., Asfaw, B., Beyene, Y., Haile-Selassie, Y., Lovejoy, C.O., Suwa, G., WoldeGabriel, G., 2009. Aridipithecus ramidus and the paleobiology of early hominids. *Science* **326**, 75–86.

Willeit, M., Ganopolski, A., Feulner, G,. 2013. On the effect of orbital forcing on mid-Pliocene climate, vegetation and ice sheets. *Clim. Past* **9**, 1749–1759.

Worden, J., Noone, D., Bowman, K., the Tropospheric Emission Spectrometer science team and data contributors, 2007. Importance of rain evaporation and continental convection in the tropical water cycle. *Nature* **445**, 528–532.

Z

Zachos, J., Pagani, M., Sloan, L., Thomas, E., Billups, K., 2001. Trends, rhythms, and aberrations in global climate 65 Ma to present. *Science* **292**, 686–693.

Zhang, K.-S., Nisancioglu, K.H., Chandler, M.A., Haywood, A.M., Otto-Bliesner, B.L., Ramstein, G., Stepanek, C., Abe-Ouchi, A., Chan, W.-L., Bragg, F., Contoux, C., Dolan, A.M., Hill, D.J., Jost, A., Kamae, Y., Lohmann, G., Lunt, D.J., Rosenbloom, N.A., Sohl, L., Ueda, H., 2013a. Mid-Pliocene Atlantic meridional overturning circulation not unlike modern?. *Clim. Past* **9**, 1495–1504.

Zhang, Z.-S., Nisancioglu, K.H., Ninnemann, U.S., 2013b. Increased ventilation of Antarctic deep water during the warm mid-Pliocene. *Nature Communications* **4**, 1499.

Zhao, M., Dupont, L., Eglinton, G., Teece, M., 2003. *n*-Alkane and pollen reconstruction of terrestrial climate and vegetation for N.W. Africa over the last 160 kyr. *Org. Geochem.* **34**, 131–143.

Zhou, Y., Grice, K., Chikaraishi, Y., Stuart-Williams, H., Farquar, G.D., Ohkouchi, N., 2011. Temperature effect on leaf water deuterium enrichment and isotopic fractionation during leaf lipid biosynthesis: Results from controlled growth of C_3 and C_4 land plants. *Phytochemistry* **72**, 207−213.